

UNCLASSIFIED

Defense Technical Information Center
Compilation Part Notice

ADP010739

TITLE: Diagnostic Tools for Plasma Wind Tunnels
and Reentry Vehicles at the IRS

DISTRIBUTION: Approved for public release, distribution unlimited

This paper is part of the following report:

TITLE: Measurement Techniques for High Enthalpy
and Plasma Flows [Techniques de mesure pour les
écoulements de plasma et les écoulements a haute
enthalpie]

To order the complete compilation report, use: ADA390586

The component part is provided here to allow users access to individually authored sections of proceedings, annals, symposia, ect. However, the component should be considered within the context of the overall compilation report and not as a stand-alone technical report.

The following component part numbers comprise the compilation report:

ADP010736 thru ADP010751

UNCLASSIFIED

Diagnostic Tools for Plasma Wind Tunnels and Reentry Vehicles at the IRS

Monika Auweter-Kurtz, Markus Feigl, Michael Winter
Universität Stuttgart
Institut für Raumfahrtsysteme
Pfaffenwaldring 31
70550 Stuttgart
Germany

Introduction

Various plasma wind tunnels have been built for developing reusable space transportation systems and space probes entering the atmospheres of celestial bodies. All together they cover almost the whole reentry trajectory of a space craft [I.1]. They generate continuous plasma flows of high specific enthalpy and velocity with thermal or magnetoplasmadynamic generators. Plasma wind tunnels are used for:

- development and qualification of radiation and ablative cooling materials and thermal protection systems,
- validation of numerical codes for reentry prediction and
- development and qualification of reentry measurement devices.

The accuracy of the simulation of reentry conditions strongly depends on the ability to determine the flow conditions. These three lectures give an overview of the diagnostic methods which are qualified and in use at the IRS. Both intrusive probe measurement techniques (part A) including mass spectrometry and non-intrusive, optical techniques (part B) such as emission spectroscopy and laser induced fluorescence (LIF) are used to investigate high enthalpy plasma flows. Several measurement techniques are being developed for flight application (see part C).

The minimum set of parameters which have to be duplicated during the tests for material qualification (see Fig. I.1) are the specific enthalpy of the gas, the stagnation pressure and the surface temperature in the case of a radiation cooling material, or the heat flux for an ablative material. This is a minimum set of parameters which has to be adjusted during the test. A whole series of probes and non-intrusive techniques were developed to determine these parameters.

The average specific enthalpy of the flow in the exit plane of the plasma generator nozzle can be derived for all kinds of plasma wind tunnels by an energy balance. Therefore, the electric power consumed by the plasma source, the mass flow rate and the heat losses within the plasma generator are measured. The average specific enthalpy at the end of the plasma generator is then derived as the difference of the electrical power and the total heat loss related to the

mass flow rate. This result is very important for an initial estimation of the flow situation and even more so for the assessment of the plasma source condition and reproducibility of a test series. But without knowing the enthalpy distribution in the nozzle exit and due to the interaction between the free jet and the ambient gas in the wind tunnel, specific enthalpy near the material sample position can not be derived exclusively from this result. Direct enthalpy measurements with probes are necessary here or a calculation of the local enthalpy from the local pressure and heat flux profiles.

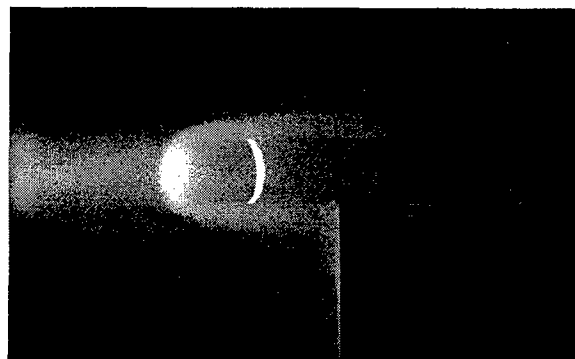


Fig. I.1: TPS material sample in the beam

However, the catalycity of the TPS materials strongly effects the surface temperature and the development of materials with the lowest possible catalycity is of great importance for future space vehicles. Plasma wind tunnels can be used to investigate the energy accommodation due to catalytic recombination near the surfaces of TPS materials. However, this requires detailed knowledge of the flow conditions within the shock layer. The measurement of the quantities of interest (temperatures, densities and velocities) is very difficult. The most significant problems are the high enthalpy and the chemically aggressive plasma, which limits probe measurements, and the fact that the flow is not in chemical and, in many instances, not in thermal equilibrium, which complicates the interpretation of measurement results. The non-equilibrium effects are more significant with lower pressure. With special probes, equipped with materials of various catalycities, the energy accommodation due to catalytic recombinations on the surface of the materials is being investigated [A2, A3, A4, A5]. LIF and emission spectroscopy are used

to determine atomic and molecular density and velocity distribution in the boundary layer [I.6]. Very important information was obtained from boundary layer investigations by emission spectroscopy in front of water-cooled copper and hot, radiating material probes [I.7, I.8, I.9].

Important information about the erosive behavior, catalycity and the failure of surface protection layers has been obtained using a mass spectrometer positioned directly behind the material sample within the plasma wind tunnel [I.10, I.8]. The transition from active to passive oxidation of materials containing Si has been investigated by LIF [I.6]. Surface temperature measurement is of great importance for material qualification, therefore, several pyrometers, including LCD systems, are available at the IRS.

For code validation the high enthalpy plasma jet has to be completely characterized at no less than two cross sections (see Fig. I.2). For this purpose a lot of measurement techniques are in use and being developed at the IRS. These are, for example, miniaturized mechanical probes for pressure and heat flux measurements [I.4]. Cylindrical electrostatic probes working in the collisionless regime are used for the detailed investigation of the electron temperatures, electron densities, plasma potentials, electron energy functions and velocities of the plasma flows [I.11, I.12]. At very high enthalpies where electrostatic probes can no longer be used due to the very high thermal and chemical load, the electron densities are high enough so that they can be determined using Thomson scattering [I.13]. Emission spectroscopic investigations are performed for the spectrally resolved analysis of the plasma radiation. The spectroscopic measurements also allow for the identification of various plasma parameters (temperatures and densities) in regions where intrusive probe measurements are impossible [I.14]. A Fabry-Perot Interferometer is used as a high resolution spectrometer to determine the plasma velocity from Doppler measurements. From the broadening of specific emission lines the translational and kinetic temperatures of the heavy particles in the plasma flow can be determined [I.12, I.15]. LIF will be used as for the boundary layer to determine the atomic densities of oxygen and nitrogen, NO-density distribution and velocity distribution [I.6]. For very low densities a mass spectrometer as a probe positioned in the plasma flow allows the plasma composition and the distribution of ions, molecules and neutral components to be determined [I.16]. The comparison of the experimental results with numerical calculations and flow simulations, which are also conducted at the IRS, are very important for both the diagnostic and code development of high enthalpy flows [I.17].

For planetary entry missions the radiative heat flux plays a major role due to very high entry velocities or

carbonaceous atmospheres. Therefore, a probe was developed at the IRS for overall radiation measurements [I.18, I.19].

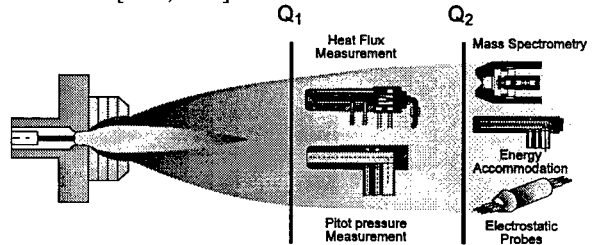


Fig. I.2: Experimental set-up for numerical code validation

Some diagnostic techniques which are in use in the PWKs can be further developed and qualified for flight applications on ballistic or winged reentry vehicles. A miniaturized pyrometric sensor system called PYREX [I.20, I.21] was developed and flight qualified for TPS temperature measurements. Furthermore, a catalytic sensor experiment is being developed [I.22]. An emission spectroscopic experiment is currently being prepared in conjunction with DASA [I.9]. Based on our experience with electrostatic probes in the wind tunnel environment, an electrostatic probe for space applications is being developed.

References

- [I.1] Auweter-Kurtz, M., Frühauf, H., Messer-schmid, E., Schöttle, U., Sleziona, C., "Wieder-eintrittsprobleme von Raumflugsystemen", IRS-95-M-1, Institut für Raumfahrtssysteme der Universität Stuttgart, 1995.
- [I.2] Stöckle, T., Winter, M., Auweter-Kurtz, M., "Simultaneous Spectroscopic and Mass Spectroscopic Investigation of Surface Catalytic Effects in High Enthalpy Gas Flows", AIAA-98-2845, 7th AIAA/ASME Joint Thermophysics and Heat Transfer Conference, Albuquerque, NM, 1998.
- [I.3] Stöckle, T., Auweter-Kurtz, M., Laure, S., "Material Catalysis in High Enthalpy Air Flows", AIAA-96-1904, 31st AIAA Thermophysics Conference, New Orleans, LA, 1996.
- [I.4] Laure, S., "Aufbau und Qualifikation von Versuchseinrichtungen zur Erzeugung von Hochenthalpie-Luftströmungen und deren Charakterisierung mittels mechanischer Sonden", Dissertation, Universität Stuttgart, 1998.
- [I.5] Fasoulas, S., Stöckle, T., Auweter-Kurtz, M., "Measurement of Specific Enthalpy in Plasma Wind Tunnels Using a Mass Injection Probe", AIAA-97-2496, 32nd Thermophysics Conference, Atlanta, GA, June 1997.
- [I.6] Auweter-Kurtz, M., Dabalà, P., Feigl, M., Habiger, H., Kurtz, H., Stöckle, T., Wegmann, T., Winter, M., "Diagnostik mit Sonden und optischen Verfahren", Teilprojekt A3, Sonderforschungsbereich 259 Arbeits- und Ergebnisbericht 1998, pp. 65-90.
- [I.7] Winter, M., Auweter-Kurtz, M., Kurtz, H., Park, C., "Investigation of an Equilibrium Condition Boundary Layer in Front of a Material Probe in a Subsonic Plasma Flow", AIAA-96-1853, 31st Thermophysics Conference, New Orleans, LA, 1996.

- [I.8] Dabalà, P., "Untersuchung des Erosionsverhaltens von Hitzeschutzmaterialien für Wiedereintrittsflugkörper unter Einsatz eines Massenspektrometers", Dissertation, Universität Stuttgart, 1998.
- [I.9] Winter, M., Auweter-Kurtz, M., "Emission Spectroscopic Investigation of the Boundary Layer in Front of a Blunt Body in a Subsonic Air Plasma Flow", Proceedings of the 3rd European Symposium on Aerothermodynamics for Space Vehicles, ESTEC, Noordwijk, The Netherlands, 1998.
- [I.10] Dabalà, P., Auweter-Kurtz, M., "Mass Spectrometric Erosion Measurements of Ceramic Thermal Protection Materials in High Enthalpy Plasma", AIAA-97-2590, 32nd Thermophysics Conference, Atlanta, GA, 1997.
- [I.11] Habiger, H., Auweter-Kurtz, M., "Investigation of High-Enthalpy Air Plasma Flow with Electrostatic Probes", Journal of Thermophysics and Heat Transfer, Vol. 12, No. 2, April-June 1998, S. 198-205; also AIAA-96-1864, 31st AIAA Thermophysics Conference, New Orleans, LA, June 1996.
- [I.12] Habiger, H., "Elektrostatische Sonden und Fabry-Perot Interferometrie zur Untersuchung von lichtbogenbeheizten Plasmen für Triebwerksanwendungen und Wiedereintritts-simulation", Dissertation, Universität Stuttgart, 1994.
- [I.13] Schumacher, U., Hirsch, K., "Spektroskopie und Laserdiagnostik", Teilprojekt A2, Sonderforschungsbereich 259 Arbeits- und Ergebnisbericht 1998, pp. 39-63.
- [I.14] Röck, W., Auweter-Kurtz, M., "Spectral Measurements in the Boundary Layer of Probes in Nitrogen/Methane Plasma Flows", AIAA-97-2525, 32nd Thermophysics Conference, Atlanta, GA, 1997.
- [I.15] Habiger, H., Auweter-Kurtz, M., "Fabry-Perot Interferometry for the Investigation of a High Enthalpy Plasma Flow", AIAA-95-2040, 30th Thermophysics Conference, San Diego, CA, 1995.
- [I.16] Schönemann, A., Auweter-Kurtz, M., "Mass Spectrometric Investigation of High Enthalpy Plasma Flows", Journal of Thermophysics and Heat Transfer, Vol. 9, No. 4, Oct.-Dec. 1995, pp. 620-628.
- [I.17] Fay, J.A., Riddell, F.R., "Theory of Stagnation Point Heat Transfer in Dissociated Air", Journal of Aeronautical Sciences, Vol. 25, No. 2, February 1958.
- [I.18] Röck, W., Auweter-Kurtz, M., "Experimental Investigation of the Huygens Entry into the Titan Atmosphere within a Plasma Wind Tunnel", AIAA-95-2112, 30th Thermophysics Conference, San Diego, CA, 1995.
- [I.19] Röck, W., "Simulation des Eintritts einer Sonde in die Atmosphäre des Saturnmondes Titan in einem Plasma-windkanal", Dissertation, Universität Stuttgart, 1998.
- [I.20] Auweter-Kurtz, M., Hald, H., Koppenwallner, G., Speckmann, H.-D., "German Experiments Developed for Reentry Missions", Acta Astronautica, Vol. 38, No. 1, 1996, pp. 47-61.
- [I.21] Habiger, H., Auweter-Kurtz, M., Frühlitz, H., Herdrich, G., "PYREX - Pyrometric Measurement on the Ceramic TPS of the Reentry Capsule MIRKA", Proceedings of the 3rd European Workshop on Thermal Protection Systems, ESTEC, Noordwijk, The Netherlands, March 1998, pp. 353-362.
- [I.22] Stewart, D.A., Rakich, J.V., Lanfranco, M.J., "Catalytic Surface Effects Experiment on the Space Shuttle", AIAA-81-1143, AIAA 16th Thermophysics Conference; also Progress in Aeronautics and Astronautics, Vol. 82: Thermophysics of Atmospheric Entry, pp. 249-272.

A Intrusive Measurement Techniques

Besides the so-called mechanical probes, the mass spectrometry, electrostatic and radiation probes also belong to the group of intrusive measurement techniques. As the name already suggests, this diagnostic method is based on a suitably constructed probe being mounted in the plasma stream which is to be investigated. This differs from the optical measurement techniques which will be described in the second part of this lecture. The mechanical probes are among the most important instruments for plasma-diagnostic measurements and are therefore also often used. They can essentially be divided into five groups according to the parameters to be investigated. We differentiate between:

- material sample support,
- Pitot pressure probes,
- aerodynamic wedge probes,
- heat flux probes,
- enthalpy probes and
- solid-state electrolyte probes.

All of these probes can be installed at the IRS on four-axis platforms inside the plasma wind tunnels. Three of the axes are linearly oriented, notated as x, y and z; the fourth axis provides the possibility to rotate the probes around the z-axis.

The wedge probe is used to ascertain the static pressure and the Mach number of the supersonic flow. A solid-state electrolyte probe can determine the oxygen particle pressure in a stream. With a mass spectrometer probe, particle densities and the energy distribution of the particles can be investigated. In the case of the other four probes, they each measure what their name implies.

With the exception of the Mach number and the oxygen partial pressure measurements, all of the measuring techniques with mechanical probes are ultimately based on the measurements of pressure, flux and/or temperature, whereby the attempt must be made to ascertain these parameters with the highest possible exactness. In practice, these supposedly simple measurements are very difficult [A.1]. A more or less complex theory is hidden between determining the basic parameters and ascertaining the parameters which are actually of interest, especially in the case of enthalpy and heat flux.

Besides the enthalpy probes, all mechanical probes have one common denominator - they do not actively influence the plasma, but rather quasi passively register the effects of the plasma flow in an appropriate way. This information is then used to determine the important parameters.

Electrostatic probes are used to ascertain the plasma potential, electron density and temperature, energy distribution of the electrons, ion temperature, flow

velocity and direction. The measurement principle is based on an active influence on the plasma boundary layer which forms on the probe.

A mass spectrometer probe can be used with low pressure plasmas to investigate the composition of the plasma [A.2, A.3]. Due to catalytic effects and the large pressure reduction which is necessary, the possibility of this at pressures above 1 hPa is limited and it is only possible with a two-step system. However, a mass spectrometer probe can be used advantageously for on-line investigations of erosion behavior [A.4, A.5] and the catalytic behavior [A.6, A.7] of thermal protection materials.

The use of radiometric probes is unavoidable when the radiation heat flux can not be neglected compared to the convective part. This is the case when during sample return missions the entry speed into the Earth's atmosphere is especially high or when the atmosphere of another celestial body (which is to be entered) contains strong radiating species, as for example the atmosphere of Titan [A.8, A.9].

The outward appearance of a probe not only depends on the parameter to be measured, but rather also on whether for example the free jet conditions should be measured or whether the plasma composition on the surface of the material sample being investigated is important. In the last case, the outward appearance of all the probes is adapted to the form of the material probe.

References

- [A.1] Auweter-Kurtz, M., "Meßverfahren für strömende Plasmen", IRS-94-M1, Institut für Raumfahrtssysteme der Universität Stuttgart, 1994.
- [A.2] Schönemann, A., Auweter-Kurtz, M., "Mass Spectrometric Investigation of High Enthalpy Plasma Flows", *Journal of Thermophysics and Heat Transfer*, Vol. 9, No. 4, Oct.-Dec. 1995, pp. 620-628.
- [A.3] Schönemann, A., "Massenspektrometrie zur Untersuchung lichtbogenbeheizter Plasmen in Niederdruck-Plasmawindkanal", Dissertation, Universität Stuttgart, 1994.
- [A.4] Dabalà, P., "Untersuchung des Erosionsverhaltens von Hitzeschutzmaterialien für Wiedereintrittsflugkörper unter Einsatz eines Massenspektrometers", Dissertation, Universität Stuttgart, 1998.
- [A.5] Dabalà P., Auweter-Kurtz, M., "Mass Spectrometric Investigations of Erosion Behavior of Thermal Protection Materials", ESA 2nd European Workshop on Thermal Protection Systems, Stuttgart, Germany, October 1995.
- [A.6] Stöckle, T., Winter, M., Auweter-Kurtz, M., "Simultaneous Spectroscopic and Mass Spectroscopic Investigation of Surface Catalytic Effects in High Enthalpy Gas Flows", AIAA-98-2845, 7th AIAA/ASME Joint Thermophysics and Heat Transfer Conference, Albuquerque, NM, 1998.
- [A.7] Stöckle, T., Auweter-Kurtz, M., Laure, S., "Material Catalysis in High Enthalpy Air Flows", AIAA-96-1904, 31st AIAA Thermophysics Conference, New Orleans, LA, 1996.
- [A.8] Röck, W., "Simulation des Eintritts einer Sonde in die Atmosphäre des Saturnmondes Titan in einem Plasmawindkanal", Dissertation, Universität Stuttgart, 1998.
- [A.9] Auweter-Kurtz, M., Laure, S., Röck, W., "Experimental Planetary Entry Simulation within a Plasma Wind Tunnel", *Proceedings of the 2nd European Symposium on Aerothermodynamics for Space Vehicle*, ESTEC, Noordwijk, The Netherlands, November 1994, pp. 429-436.

A1 Material Sample Support

Ablative materials are supported by water-cooled support systems of different sizes. An example is shown in Fig. A1.1.

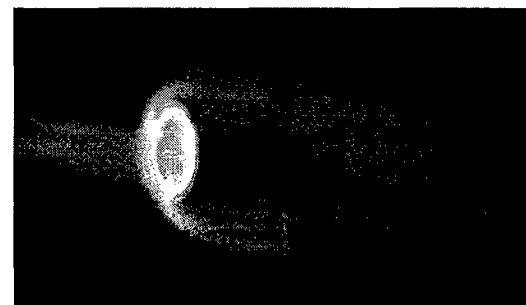
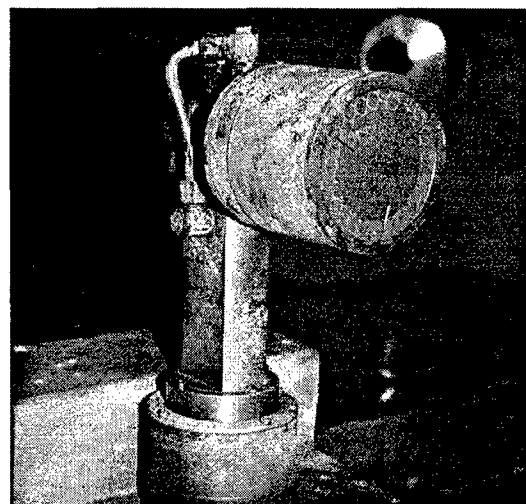
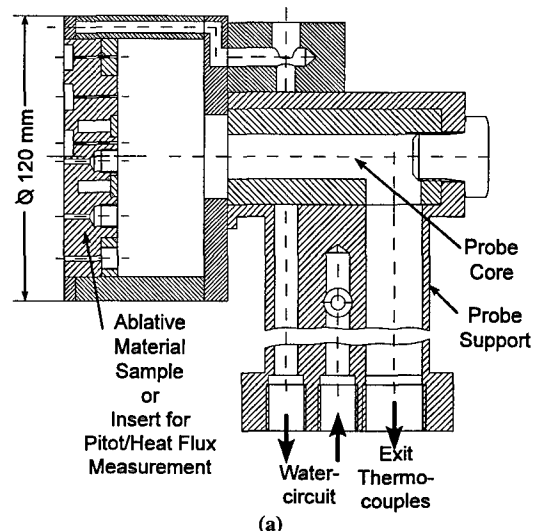


Fig. A1.1: Sample support for ablative material

The temperature distribution within the ablator is usually measured by thermocouples located at different distances from the front surface of the ablator.

A material sample support system which minimizes the heat exchange with the sample perpendicular to the flow is required for material qualification. In Fig. A1.2 the sample support for ceramic material in a stagnation point configuration is shown. The rear side temperature of the sample can be determined with a linear pyrometer (see also part B) via a fiber optic connection.

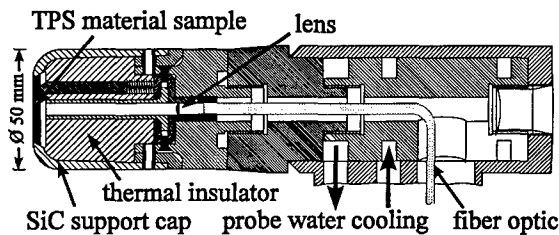


Fig. A1.2: Scheme of a TPS material probe with integrated pyrometer fiber optics

A2 Pitot Pressure Probes

With Pitot probes it is possible to measure the dynamic or total stagnation pressure of the plasma flow by connecting them either to a differential pressure gauge inside or to a total pressure gauge outside of the vacuum tank.

Figure A2.1 shows the scheme of the 'spherical head' Pitot probe which has an identical geometry to the material support system shown in Fig. A1.2.

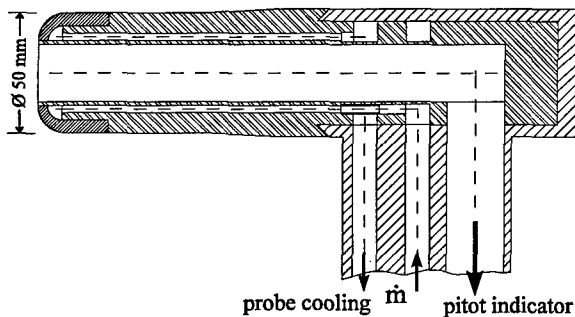


Fig. A2.1: 'Spherical head' Pitot probe

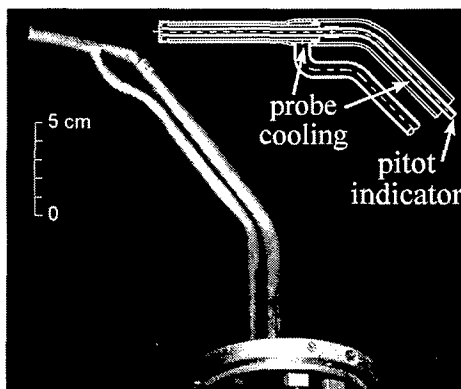


Fig. A2.2: Miniaturized Pitot probe

In Fig. A2.2 a miniaturized Pitot probe which is used for local measurements in the plasma flow can be seen. This probe is designed to determine very high heat fluxes of more than 10 MW/m^2 [A2.1].

When using Pitot probes, one must generally differentiate between two cases: pressure measurement in a subsonic flow and pressure measurement in a supersonic flow. In the first case, the conditions are relatively simple. The Bernoulli equation is valid whereby the simple equation

$$p_0 = p_\infty + \frac{\rho_\infty}{2} v_\infty^2 \quad (\text{A2.1})$$

at Mach numbers of $\text{Ma} > 0.3$ must be replaced by the Bernoulli equation for compressible flows. If friction effects are neglected and assuming that the changes in the condition run lengthwise isentropically along the lines, the following connection exists between the flow parameters:

$$p_0 = p_\infty \left(1 + \frac{\kappa - 1}{\kappa} \frac{\rho_\infty}{p_\infty} \frac{v_\infty^2}{2} \right)^{\frac{\kappa}{\kappa - 1}}, \quad (\text{A2.2})$$

whereby κ means the averaged adiabatic exponent, p_0 represents the pressure in the stagnation point and $p_\infty, \rho_\infty, v_\infty$ the quantities of the undisturbed flow. With that one can, for example, deduce the density from the pressure measurement when the speed and κ are known.

In supersonic flows a compression shock forms in front of the probe which results in a loss of total pressure. The probe measures the total pressure p_0 after the shock. Assuming that the compression shock runs perpendicular to the initial direction of flow and the changes in the condition run isentropically in front of and behind the shock, then the following is valid for p_0 :

$$p_0 = \frac{\kappa - 1}{2} \text{Ma}^2 \left[\frac{(\kappa + 1)^2 \text{Ma}^2}{4\kappa \text{Ma}^2 - 2(\kappa - 1)} \right]^{\frac{1}{\kappa - 1}} p_\infty \quad (\text{A2.3})$$

Here Ma is the Mach number in front of the shock and κ , on the other hand, is the averaged adiabatic exponent. If the Mach number is additionally determined with a wedge probe (see section A3) then the average adiabatic exponent can be calculated from this last equation.

However, one must be very careful when interpreting the measurement results from a Pitot probe. The viscosity effects of a flow affected by friction have to be considered. Two additional aspects must also be taken into account. These are the effect of the shape of the bore hole and the error which results when the longitudinal axis of the probe and the plasma stream axis are not aligned [see A2.2]. The size of the bore hole has to be large compared to the mean free path.

References

- [A2.1] Laure, S., "Aufbau und Qualifikation von Versuchseinrichtungen zur Erzeugung von Hochenthalpie-Luftströmungen und deren Charakterisierung mittels mechanischer Sonden", Dissertation, Universität Stuttgart, 1998.
- [A2.2] Habiger, H., "Elektrostatische Sonden und Fabry-Perot Interferometrie zur Untersuchung von lichtbogenbeheizten Plasmen für Triebwerksanwendungen und Wiedereintrittssimulation", Dissertation, Universität Stuttgart, 1994.

A 3 Aerodynamic Wedge Probe

Aerodynamic wedge probes can be used to ascertain the static pressure and Mach number of a supersonic flow. Their main component is a water-cooled copper wedge (see Fig. A3.1) which is placed in a supersonic flow, whereby attention must be paid to the parallel alignment of the probe surface to \bar{v}_∞ . With the help of a pressure measurement bore hole on the top side of the probe the static pressure can also be determined.

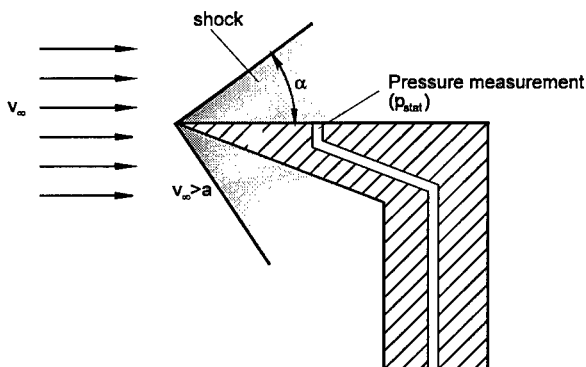


Fig. A3.1: Wedge probe in a supersonic stream

The tip of the wedge probe causes a disturbance in the flow which spreads analogously to the sound wave in the supersonic flow shown in Fig. A3.2. The effects of the disturbances are limited to the inside of a cone whose half open angle α , recognizable in Fig. A3.2, can be calculated as follows:

$$\sin \alpha = \frac{at}{vt} = \frac{a}{v} = \frac{1}{Ma} \quad (A3.1)$$

This cone is called a Mach cone.

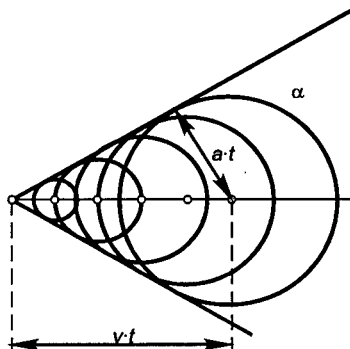


Fig. A3.2: Spreading of supersonic sound waves

From the measurement of the angle between the Mach line and the plasma stream axis the Mach number at this point can be determined.

When used in a high enthalpy flow (see Fig. A3.3), especially the cooling of the wedge tip causes problems. If the tip of the wedge is not sharp enough, the contour can not be discerned.

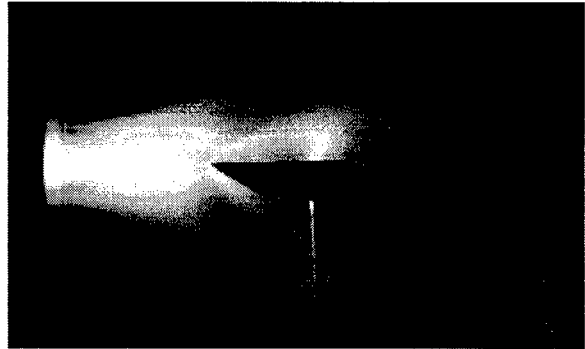


Fig. A3.3: Wedge probe in a plasma stream

A4 Heat Flux Measurements

Heat transfer to a body exposed to the plasma flow is of great interest for reentry simulation in a high enthalpy flow. With the heat flux probes described in this section, the total heat flux is measured. A radiometer probe which can be used for measuring the radiative part exclusively is described in section A9.

However, for the total heat flux measurement the material of the probe itself is of great importance because the heat transfer may vary depending on the catalyticity of the material of the body. In addition, the surface temperature of the probe may change the measurement result since it affects the recombination rate and its emission coefficient. As a standard reference material for heat flux probes copper is mostly used as it has a relatively high catalytic efficiency. However, it is not an ideal material as a standard because in an oxidizing atmosphere it forms two different oxides which change the catalyticity.

At the IRS both stationary and non-stationary heat flux measurement devices are used. The actual probes are inserted into the front plate of a water-cooled support system, having the identical geometry of the material probe, and consisting of either a water-cooled tube or a Gardon Gage for stationary measurements or a heat sink slug for non-stationary measurements. The probes can be coated and the slug can be made of copper or other materials such as tungsten or SiC to investigate the influence of the surface catalyticity [A4.1, A4.2].

The inserts, which can be seen in Figs. A4.1, A4.2, and A1.1a are thermally insulated from the surrounding support. Therefore, the heat flux onto the defined front area of the insert facing the plasma flow is measured.

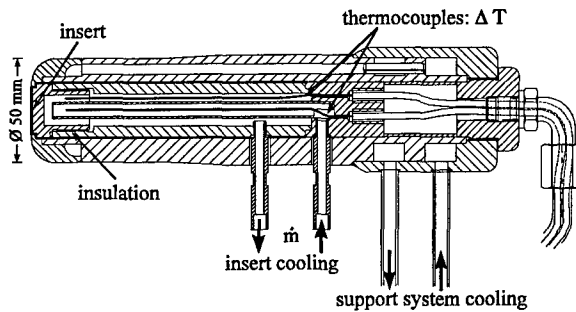


Fig. A4.1: Stationary heat flux probe

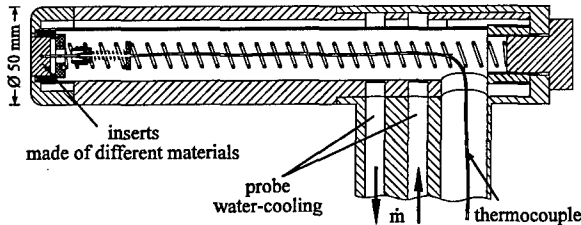


Fig. A4.2: Non-stationary heat flux probe

A4.1 Stationary Heat Flux Measurement

Two different principles are in use for stationary heat flux measurement.

A4.1.1 Calorimetric Probe

With this method the heat flux to a relatively cold surface is measured. Normally water is used for cooling the body of this type of probe (Fig. A4.1). From the heat which is carried off by the cooling water, one obtains the heat flux \dot{q} onto the front surface A_s by measuring the temperature difference between the cooling inflow and the outlet and its mass flow \dot{m}_c according to the equation:

$$\dot{q} = \frac{\dot{m}_c}{A_s} c_c \Delta T. \quad (\text{A4.1})$$

Here c_c represents the specific heat capacity of the coolant.

While operating the probe, one must keep in mind that the flow rate of the coolant is large enough to guarantee sufficient cooling on the one hand, and on the other hand small enough to keep the temperature difference between the inflow and outlet at a reasonable level so that it can still be measured.

A4.1.2 Gardon Gage

With this method the heat flux is determined from the temperature gradient which forms between the center and the edge of a circular foil. A heat flux probe of this principle called the Gardon Gage, named after its inventor Robert Gardon, consists of a heat sink in the form of a hollow cylinder usually made of copper and

a foil attached to the front side of the cylinder and typically made of constantan. The constantan foil is in turn connected with a copper wire in the center (Fig. A4.3). If the heat sink is kept at a constant temperature, for example by embedding it in a water-cooled sample, a radial temperature drop forms on the foil.

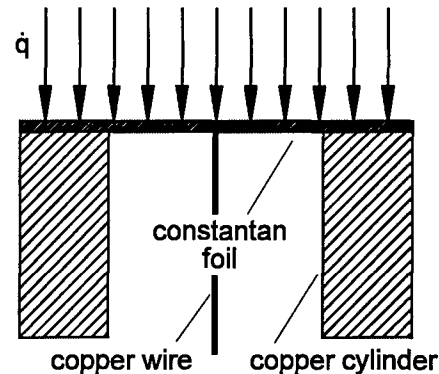


Fig. A4.3: Construction of a Gardon Gage

Assuming that the front and back of the foil do not give off any heat and that no temperature gradients are present across the thickness s of the foil, the following equation for stationary temperature distribution results from the parameters in Fig. A4.4:

$$\frac{\dot{q}}{s\lambda} + \frac{1}{r} \frac{dT_{\text{stat}}}{dr} + \frac{d^2 T_{\text{stat}}}{dr^2} = 0. \quad (\text{A4.2})$$

Here T_{stat} is the stationary temperature of the foil at the radius r and λ is the heat conductivity of the foil.

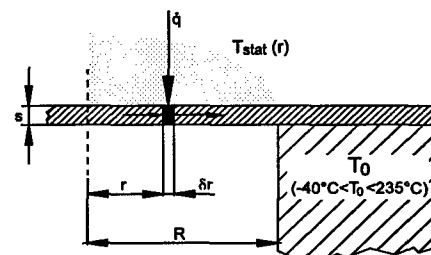


Fig. A4.4: Geometric relations

Considering the fact that the heat conductivity increases linearly when the temperature increases according to $\lambda = \lambda_0 (1 + \alpha(T - T_0))$, the solution to the above differential equation results in the following equation:

$$\Delta T \left(1 + \frac{\alpha}{2} \Delta T \right) = \dot{q} \frac{R^2}{4\lambda_0 s}, \quad (\text{A4.3})$$

where ΔT represents the temperature difference between the center point and the edge of the foil. With the values for λ_0 and α one obtains for constantan:

$$\dot{q} = \frac{1}{2026.25} \frac{s}{R^2} \Delta T (1 + 0.00115 \Delta T) \left[\frac{\text{W}}{\text{m}^2} \right]. \quad (\text{A4.4})$$

It is evident that the dependence of the temperature difference on the heat flux to be measured is still not linear.

This disadvantage can, however, be compensated for. Figure A4.3 shows how two thermal element transitions form in the center and at the edge of the foil where the copper cylinder or rather the wire and the constantan foil are connected. The fact that the temperature difference calculated above exists between the two contact points leads to a resulting thermal voltage which can be expressed for a copper-constantan combination in the following equation:

$$U = 0.0381 \Delta T (1 + 0.00117 \Delta T) \quad [\text{mV}]. \quad (\text{A4.5})$$

The figures in brackets of the last two equations are practically identical so that the measured thermal voltage becomes directly proportional to \dot{q} :

$$U \approx 77.2 \frac{R^2}{s} \dot{q} \quad [\text{mV}]. \quad (\text{A4.6})$$

Another advantage of the Gardon Gage is the compact design. The dimensions are usually only a few mm in diameter so that several sensors can easily be integrated into a probe body. As a result of their small size and low heat capacity the response times are also very short so that fast heat flux fluctuations, for example due to fluctuations of the plasma, can also be detected. The time constant τ , that is the time that passes until the sensor's output signal reaches 63% of the total with a jump in the heat flux, can be approximated by:

$$\tau \approx 3.76 \cdot 10^{-6} R^2 \quad [\text{s}]. \quad (\text{A4.7})$$

At the IRS these heat flux sensors are equipped with surface layers of different materials to study catalytic effects. But the reduction of the heat flux from measured data is no longer as easy as for the copper-constantan case.

A4.2 Non-Stationary Heat Flux Measurement

If one avoids a radial heat transport as in the stationary case, the axial heat flux can be calculated from the one-dimensional Fourier equation:

$$\frac{\partial T}{\partial t} = a \left(\frac{\partial^2 T}{\partial x^2} \right). \quad (\text{A4.8})$$

For the boundary conditions the labels from Fig. A4.5 apply:

$$t < 0: \quad \text{temperature of the probe} = T_{w0} = \text{const.}, \\ \text{heat flux } \dot{q} = 0$$

and

$$t > 0: \quad T = T(x, t), \quad (\text{A4.9}) \\ T(x=0, t) = T_w(t).$$

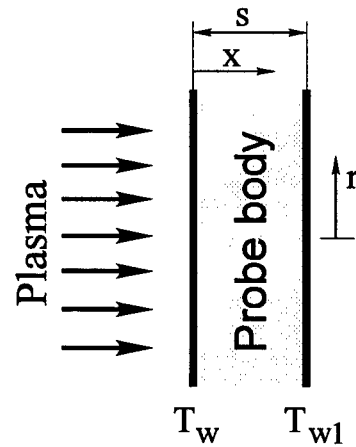


Fig. A4.5: Explanation of the parameters

One differentiates between two different methods - the thin wall and the thick wall method. These methods differ from each other in the realization of the last necessary boundary conditions.

A4.2.1 Non-Stationary Thin Wall Method

With this method the heat flux is assumed to be constant throughout the entire thickness of the probe:

$$\dot{q}_{x=0} = \dot{q}_{x=s}. \quad (\text{A4.10})$$

The solution to the Fourier equation can be greatly simplified for Fourier numbers

$$F_0 = \frac{at}{s^2} > 0.3. \quad (\text{A4.11})$$

The temperature rise is measured and the heat flux can be directly determined from this:

$$\dot{q} = \rho c_p s \frac{dT}{dt}. \quad (\text{A4.12})$$

The ρ and c_p represent the density and specific heat capacity of the material, respectively. With a probe body made of copper with a thickness of 10 mm, the condition $F_0 > 0.3$ is for example fulfilled after a measurement time of $t_{\min} > 0.27$ s.

Although the theory of the non-stationary thin wall method neglects heat fluxes in a radial direction (that is $d\dot{q}/dr \neq 0$), in practice this condition can not be completely fulfilled. A simple estimate shows, however, that these heat fluxes do not interfere with the measurement as long as the heating of the body does not last longer than a certain maximum time t_{\max} . The following is valid for the maximum measurement time:

$$t_{\max} \ll \left| \frac{\dot{q}}{\frac{d\dot{q}}{dy} s} \right| \frac{s^2}{a}. \quad (\text{A4.13})$$

A typical heat flux probe using the thin wall method is shown in Fig. A4.2.

A4.2.2 Non-Stationary Thick Wall Method

With the non-stationary thick wall method one assumes that the temperature on the back of the sample body does not rise during the measurement. The solution to the Fourier equation while keeping this boundary condition in mind is:

$$\dot{q}(t) = \sqrt{\frac{\rho c_p \lambda}{\pi}} \left[\frac{T(t)}{\sqrt{t}} + \frac{1}{2} \int_0^t \frac{T(t) - T(\tau)}{(t - \tau)^{3/2}} d\tau \right] \quad (\text{A4.14})$$

If one can assume that the heat flux is constant over time, the solution to the Fourier equation for this case can be written as follows:

$$T(x = 0, t) - T_{w0} = \frac{2}{\sqrt{\pi}} \dot{q} \sqrt{\frac{t}{\rho c_p \lambda}} \quad (\text{A4.15})$$

Contrary to the thin wall method, in using this equation there is no demand for a minimum test time t_{\min} . On the other hand, it is only valid as long as the increase in temperature has not spread over the entire measurement element. That is $T(\infty, t)$ is no longer equal to T_{w0} .

In the thin wall method only the material constants ρ and c_p have to be known, while in the thick wall method the heat conductivity λ of the sample body must also be known. Because this parameter is very difficult to determine in experiments, it can be viewed as a disadvantage. In contrast to this, the thick wall method used for heat flux measurements in a plasma wind tunnel offers the possibility while passing through the plasma stream of determining the entire profile at one time because it is possible to calculate back from the temperature-time course via Eq. (A4.14) to $q(t)$ or when the speed of the probe is known to $q(y)$. This is not possible with the thin wall method. Here the jet beam profile must be interpolated from individual measurements at various radial positions.

But the length of the thick wall sensor must be sufficient so that within the measurement time needed a rise in temperature does not occur at the back of the sensor. With metallic samples the minimum length can be approximately calculated according to the equation:

$$l_{\min} [\text{cm}] = 4 \sqrt{t_{\text{meß}} [\text{s}]} \quad (\text{A4.16})$$

This means that with a typical measurement time in a plasma wind tunnel of approximately 8 s for a radial scan, the sensor length must be around 10 cm. This is one of several reasons that these kinds of sensors have mostly been used in shock tubes and shock tube wind tunnels up to now.

With this method the temperature of the front surface has to be observed. A simple measurement of the front surface temperature is possible when the sensor is designed as a thermocouple. Here the sensor is made of a round material which is inside a hollow cylinder. The material and the cylinder are separated

from each other by a layer of insulation which runs along the sides. The front surface is, for example, dampened with a conductive layer (see Fig. A4.6). In this way, catalycity tests with different layers can also be carried out.

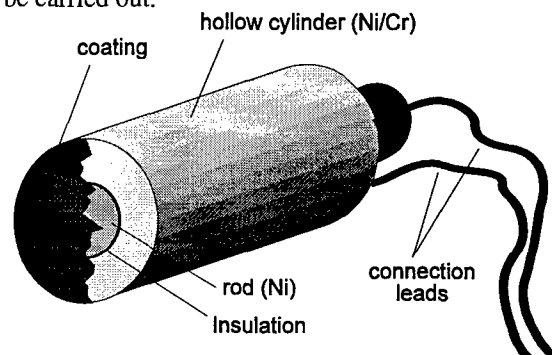


Fig. A4.6: Non-stationary heat flux probe according to the thick wall method, Shock Wave Lab, RWTH Aachen

A4.3 Influence of Surface Catalycity on Heat Flux Measurements

Apart from the uncontrolled heat losses which have already been mentioned there is a far more important factor which can considerably influence the measurement results: the surface catalycity of the sample.

The heat flux on a sample in a dissociated gas (while neglecting the radiation portion) which is not chemically balanced consists of two parts joined together. The first part is supplied by the normal, molecular heat conductivity of the plasma. The second forms when atom pairs recombine on the surface. Here they transfer some of their recombination energy to the sample. The quantitative relationship between the two parts, heat conductivity and recombination, depends greatly on the length of time that the recombination partners are in the boundary layer. If the time necessary for the potential reaction partners to make their way to the sample surface by means of diffusion is much longer than the time needed by the partners for the recombination reaction, then one speaks of a *balanced boundary layer*. In this case the surface catalycity of the sample does not play a role because the particles already recombine beforehand and transfer their energy to the gas mixture. Contrary to this, the surface catalycity becomes important when a so-called *frozen boundary layer* prevails. In this case, the recombination time is much longer than the diffusion time through the boundary layer so that all potential reaction partners that enter the boundary layer also reach the front surface of the sample. If the nature of the surface encourages recombination, then the reaction energy will be set free on the surface and the heat flux onto the wall will increase. However, if

the surface is not conducive to recombination, then the particles leave the boundary layer again without having released their energy. This characteristic is quantitatively expressed by the so-called recombination coefficient of a material γ . Here $\gamma = 1$ means that all of the atoms that make it to the surface recombine (fully catalytic behavior), and $\gamma = 0$ that no catalytic recombination reactions take place (non-catalytic behavior).

As an example Fig. A4.7 shows the results of heat flux measurements that were performed with probes made of different materials. The 'n' or 's' in the key explains what kind of measurement it was (n: non-stationary, s: stationary, thin wall method). One assumes with the stationary measurement that the surface temperature remains constant and is only slightly higher than the temperature of the coolant (300 K). The temperature for the stationary measurements applies to the sample's average surface temperature when measuring in the middle of the beam ($y = 0$). One recognizes that the surface catalyticity can increase the heat flux by more than a factor of 2 and that a material's catalyticity increases as the temperature rises.

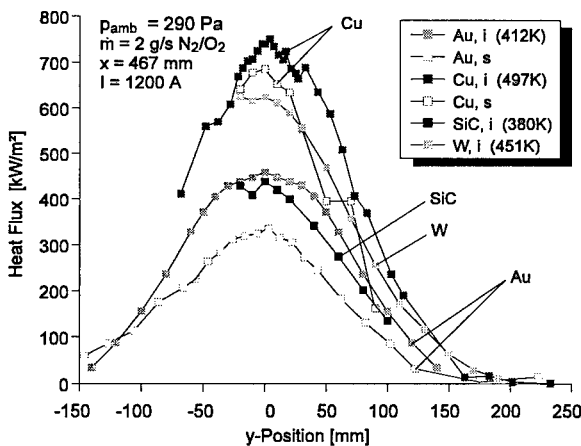


Fig. A4.7: Results of heat flux measurements with various samples

Copper has the highest catalyticity of all the normal metals used. Its recombination coefficient is 0.2 - 0.5 and for gold between 0.04 and 0.09.

References

- [A4.1] Stöckle, T., Auweter-Kurtz, M., Laure, S., "Material Catalysis in High Enthalpy Air Flows", AIAA-96-1904, 31st AIAA Thermophysics Conference, New Orleans, LA, 1996.
- [A4.2] Stöckle, T., Fasoulas, S., Auweter-Kurtz, M., "Heterogeneous Catalytic Recombination Reactions Including Energy Accommodation Considerations in High Enthalpy Gas Flows", AIAA-97-2591, 32nd Thermophysics Conference, Atlanta, GA, 1997.

A5 Enthalpy Measurements

Due to the very high velocity of the plasma jet, the total specific enthalpy of the gas consists of two parts according to:

$$h_t = \frac{1}{2} v^2 + c_p T \quad (\text{A5.1})$$

As discussed in the introduction, due to the unknown enthalpy distribution in the nozzle end section and due to interaction of the jet with the ambient gas, the local enthalpy can not be derived from the averaged value in the nozzle exit plane. Therefore, at the IRS two different enthalpy probes are used depending on the pressure level. The main differences are that in one case the plasma is suctioned out and in the other case gas is injected. In addition to this, the specific enthalpy is calculated from the heat flux measurements.

A5.1 Mass Suction Enthalpy Probe

If the total pressure is high enough, then the local specific enthalpy and the local mass flow rate of a supersonic flow can be determined by suctioning out mass using the probe pictured in Fig. A5.1.

The mass flow which corresponds to the probe opening is suctioned out with a pump and here \dot{m}_g and the gas temperature $T_{g,2}$ at the end of the probe and consequently the enthalpy of the gas at this point can be determined. The suction power has to be adjusted so that the compression shock which forms in front of the probe is perpendicular to the inlet opening so that mass escaping or in-flow is avoided.

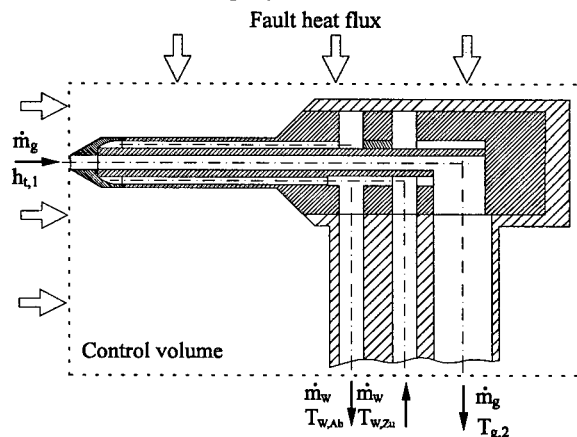


Fig. A5.1: Set-up of a mass suction enthalpy probe

The amount of heat which is carried off with the cooling water is measured with (V. open) as well as without (V. closed) suction and so the amount of heat extracted from the gas flow is determined by means of the difference. The energy balance reads as follows:

$$\dot{m}_g h_{t,1} = \dot{m}_W c_W (T_{W,\text{outflow}} - T_{W,\text{inflow}})_{V,\text{open}} - \dot{m}_W c_W (T_{W,\text{outflow}} - T_{W,\text{inflow}})_{V,\text{closed}} + \dot{m}_g c_p T_{g,2} \quad (\text{A5.2})$$

From here the unknown total enthalpy $h_{t,1}$ can be obtained.

Another error appears when the specific enthalpy and thereby the suction speed are very high. It is possible that as a result the heat transfer to the wall and herewith to the water circulation will be greatly reduced which makes itself noticeable in that the gas temperature $T_{g,2}$ rises quickly. Based on the high gas temperature and the slight temperature increase of the cooling water connected with it, determining the enthalpy under these conditions can result in a large error. Furthermore, with low pressure plasmas the problem arises that the very low mass flow rate \dot{m}_g can only be measured correctly with great difficulty.

A5.2 Mass Injection Enthalpy Probe

This diagnostic method, which was developed at the IRS [A5.1], can be used for plasma flows at low pressures. The measurement principle is based on the reduction of the heat flux to the wall due to mass injection through the surface of the probe (see Fig. A5.2).

The surface heat transfer in a viscous non-equilibrium high enthalpy flow is for this case obtained by:

$$\dot{q}_w = \underbrace{\left(\lambda \frac{\partial T}{\partial y} \right)_w}_{\text{conduction}} + \underbrace{\left(\rho D_{12} \sum_i h_i \frac{\partial c_i}{\partial y} \right)_w}_{\text{diffusion}} + \underbrace{\dot{q}_R}_{\text{radiation}} \quad (\text{A5.3})$$

where the radiation is often negligible (also within this investigation).

A mass injection through the wall into the boundary layer now influences the layer and the transferred heat flux. It leads to a decrease of the temperature gradient on the surface and therefore to a decrease of heat flux due to conduction. Indeed, when the injection rate is high enough, the viscous layer is blown completely off the surface and the aerodynamic convective heat transfer becomes zero. Theoretical investigations by solving the transformed Navier-Stokes equations in the boundary layer show that the heat flux \dot{q} in the stagnation point of the body being investigated is clearly dependent on the mass flow of the cooling gas which is emitted and can be expressed over a wide range of operations by

$$\frac{\dot{q}}{\dot{q}_0} = 1 - 0.72 B + 0.13 B^2 \quad (\text{A5.4})$$

with the so-called mass addition factor B

$$B = \frac{\rho_w v_w}{\rho_\infty v_\infty St_0} = \frac{\rho_w v_w}{\dot{q}_0} (h_\infty - h_w) \quad (\text{A5.5})$$

Here \dot{q}_0 is the heat flux and St_0 is the Stanton number without the cooling gas mass flow. The Stanton number is defined as the relation between the heat flux which appeared and the maximum possible heat flux:

$$St_0 = \frac{\dot{q}_0}{\rho_\infty v_\infty (h_\infty - h_w)} \quad (\text{A5.6})$$

Another investigation leads to nearly identical results by solving the viscous shock layer equations [A5.2]. By varying the specific mass flow rate $\rho_w v_w$ and measuring the heat flux ratio \dot{q}/\dot{q}_0 the enthalpy can be determined from the equation system above as follows:

The heat flux to the probe is measured by varying the mass flow rate of the injection within a wide range. Then the heat flux ratio \dot{q}/\dot{q}_0 is plotted against the mass addition factor as shown in Fig. A5.4. For this B has to be calculated.

In order to calculate the mass addition factor B, the effective area specific mass flow rate of the cooling gas $\rho_w v_w$ must be known. The mass flow rate $\dot{m} = \rho_w v_w A$ can easily be measured but determining the corresponding area A is difficult. This area can not simply be stated without further ado. (In no case is it identical to the sum of the profiles of the cooling gas bore holes.) In Fig. A5.2 one can recognize (although only weakly) that the cold boundary layer arches over the entire area of the cooling gas bore holes and beyond. Measurements in plasmas with a known enthalpy that consequently allow an inference of the effective discharge area show that in a first approximation the base of the cold boundary layer can be perceived as an effective injection area.

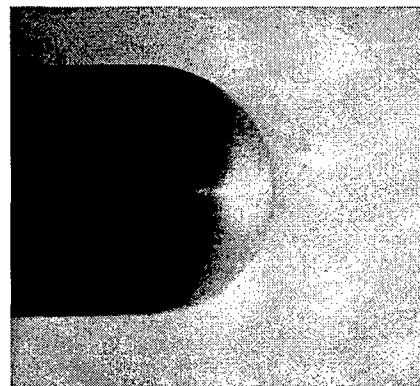


Fig. A5.2: Cold boundary layer

The second value needed to calculate B is the unknown enthalpy difference to begin with, and the enthalpy difference is arbitrarily chosen. The uncertainty in determining B results in a curve which will more or less deviate from the theoretical function. By varying a factor X the curve will approach the

theoretical curve when, for example, the least squares method is used. Figure A5.4 shows the result of such a regression calculation for various positions in the plasma stream. It is noticeable that from a mass addition factor of $B \approx 1.2$ onward a sudden deviation of the measurements from the course of the theory appears. Numerical simulations have shown that at this point the emission speed of the cooling gas reaches sonic speed. Here effects obviously appear that can no longer be explained by the theory applied. However, this is unimportant in determining the enthalpy because the upper portion of the curve is sufficient for the regression analysis.

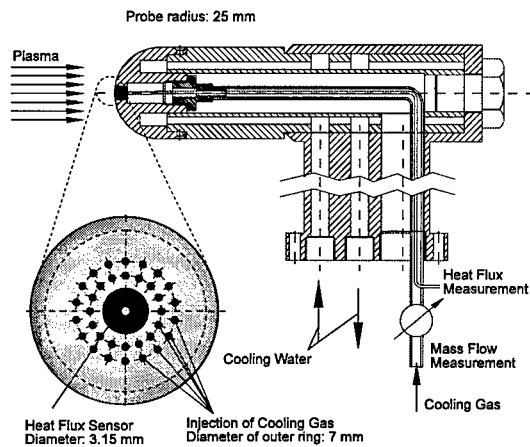


Fig. A5.3: Experimental set-up of the mass injection probe

The experimental set-up is shown in Fig. A5.3. In the hemispherical front part there are small bore holes through which the cooling gas flows and in the middle there is a Gardon Gage heat flux sensor. The front of the probe differs from the otherwise flat contour of the mechanical probes usually used in wind tunnels. The reason is that in a flat stagnation point the boundary layer's similarity to itself no longer exists. With that the decrease in the heat flow would no longer obey the form given in Eq. (A5.4).

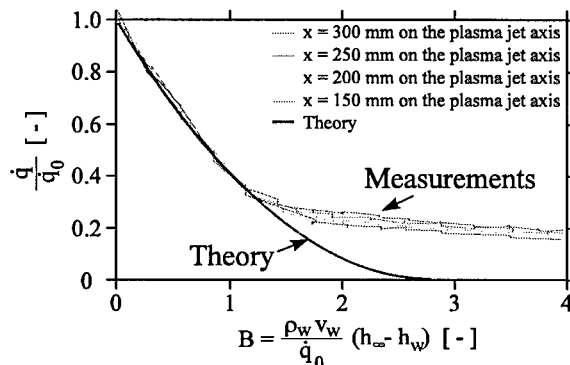


Fig. A5.4: Determining the enthalpy by adjusting the measurement curve to the theoretical course

A5.3 Determining the Specific Enthalpy from Heat Flux Measurements

The local distribution of the specific enthalpy can be determined from measurements of the local heat flux distribution and the total pressure distribution. For this purpose, Fay and Riddell [A5.3] reformed the laminar boundary layer equations for chemically reactive flows. By comparing them with experimental results, semi-empirical equations could be formed for the following three cases:

- boundary layer in chemical equilibrium (independent of the surface catalycity),
- frozen boundary layer with a fully catalytic surface,
- frozen boundary layer with a non-catalytic surface.

As an example of this only the equation for the heat flux on a fully catalytic surface is given:

$$\dot{q}_{fc} = 0.763 \text{Pr}^{-0.6} \left(\frac{\rho_w \mu_w}{\rho_\infty \mu_\infty} \right)^{0.1} \sqrt{\rho_\infty \mu_\infty \beta} (h_\infty - h_w) \left[1 + (\text{Le}^{0.63} - 1) \left(\frac{h_D}{h_\infty} \right) \right] \quad (\text{A5.7})$$

With the help of Eq. (A5.7), the local enthalpy in the flow h_∞ can in principle be determined by measuring the local heat flux. However, the density ρ_∞ , viscosity μ_∞ , dissociation energy h_D , Prandtl number Pr , Lewis number Le and velocity gradient β at the stagnation point have to be known.

In the case of a chemically frozen flow, an approximate solution was given by Pope [A5.4] which only requires that the Pitot pressure and the heat flux be known in order to calculate the enthalpy:

$$h_\infty = \frac{\dot{q}_{fc}}{K \sqrt{\frac{P_{\text{tot}}}{R_{\text{eff}}}}} \quad (\text{A5.8})$$

Here K is a constant which has the value $K = 108 \text{ W}/(\text{MJ}/\text{kg bar}^{0.5} \text{ m}^{1.5})$ for nitrogen, R_{eff} is the effective leading edge radius of the probe which can be given by $R_{\text{eff}} = 2.9 r_N$ (r_N : real leading edge radius) for the relatively low Mach numbers in the plasma wind tunnels.

Here \dot{q}_{fc} represents the fully catalytic heat flux. For copper up to a specific enthalpy of approximately $50 \text{ MJ}/\text{kg}$ it can be calculated from the actual heat fluxes \dot{q}_{fc} with the help of measurements from Pope [A5.5] and Goulard [A5.6].

References

- [A5.1] Fasoulas, S., Stöckle, T., Auweter-Kurtz, M., "Measurement of Specific Enthalpy in Plasma Wind Tunnels Using a Mass Injection Probe", AIAA-97-2496, 32nd Thermophysics Conference, Atlanta, GA, June 1997.

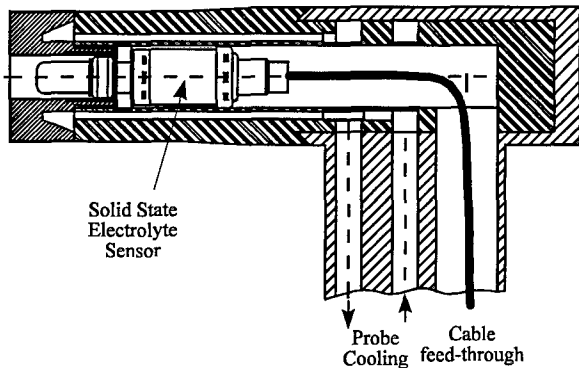


Fig. A6.3: Solid state electrolyte probe for use in a PWK

Due to the high catalyticity of the surface, these solid state electrolyte probes can not differentiate between atomic and molecular oxygen. The oxygen distribution measured with solid state electrolyte sensors corresponds to the sum from the molecule portions of O and O₂. Moreover, additional electrochemical reactions on the catalytic probe electrodes are brought about by oxidizable gases such as NO and CO which are often present in combustion gases and thereby influence the sensor voltage and may therefore falsify the measurement.

References

- [A6.1] Fasoulas, S., "Measurement of Oxygen Partial Pressure in Low Pressure and High Enthalpy Flows", AIAA-96-2213, 19th AIAA Advanced Measurement and Ground Testing Technology Conference, New Orleans, LA, 1996.

A7 Electrostatic Probes

Electrostatic probes normally used in plasma wind tunnels consist of up to three electrodes which are electrically insulated from each other and from mass and are exposed to the plasma. By recording current-voltage characteristics or current-time developments, the various parameters of the plasma such as plasma potential, electron temperature and density, flow direction, electron energy function, plasma velocity or ion temperature can be determined at the position of the probe electrodes [A7.1, A7.2].

If one moves an electrostatic probe into a plasma beam, a plasma boundary layer forms around the probe. This layer can be altered by varying the bias voltage across the probe. Important plasma parameters can be deduced from the probe signal. For this purpose, the boundary layer must be described theoretically.

When moving a probe into a plasma assumed to be quasi-neutral, a negative charge of the probe takes place across from the surrounding plasma. This is because the higher thermal mobility of the electrons causes more electrons than ions to reach the probe electrode surface. The negative charge causes a

repulsion of further electrons in the area around the probe. Therefore, a positive space charge layer forms which disturbs the ionization recombination equilibrium.

The higher ion density in the space charge layer around the probe, compared to the electron density, causes the formation of an electric field which decreases as the distance to the probe surface increases. As a result of the recombinations on the probe surface, charge carriers from the quasi-neutral, undisturbed plasma have to subsequently be delivered to the space charge layer. This charge carrier drift requires the existence of a weak remaining field which must also be present outside of the space charge layer in the so-called transition region. Figure A7.1 shows the development of the potential in the entire plasma surface layer.

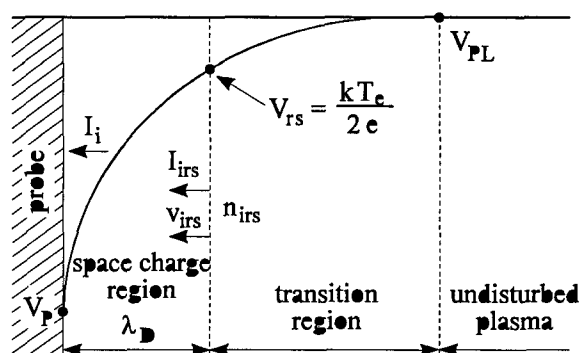


Fig. A7.1: Potential development in the plasma surface layer

The thickness of the space charge layer is given by the Debye length λ_D which is dependent on the electron temperature and density by means of the equation

$$\lambda_D = \sqrt{\frac{\epsilon_0 k T_e}{e^2 n_e}} \quad (\text{A7.1})$$

Figure A7.2 shows that, for example, in MPD tunnels the Debye length is several mm. In the adjacent transition region, a slight charge carrier concentration decline still exists which affects the drift. Despite the small, remaining electric field in the transition region, the plasma can be considered quasi-neutral for the theoretical treatment. For additional increasing distances from the probe surface, the undisturbed, quasi-neutral plasma with the potential V_{PL} is finally reached. The border of the space charge layer is determined by the so-called Bohm criteria according to which the charge carriers entering the space charge layer have to apply the energy of

$$e V_{rs} = \frac{k T_e}{2} \quad (\text{A7.2})$$

Moreover, for the theoretical description of the boundary layer, the smallest mean free path is of great importance. It is the mean free path due to electron and ion collisions:

$$\lambda_{ei} = \frac{16\pi (\epsilon_0 k T_e)^2}{e^4 n_e \ln \Lambda}$$

with

$$\Lambda = 12\pi \frac{(\epsilon_0 k T_e)^{3/2}}{n_e^{1/2} e^3} \quad (A7.3)$$

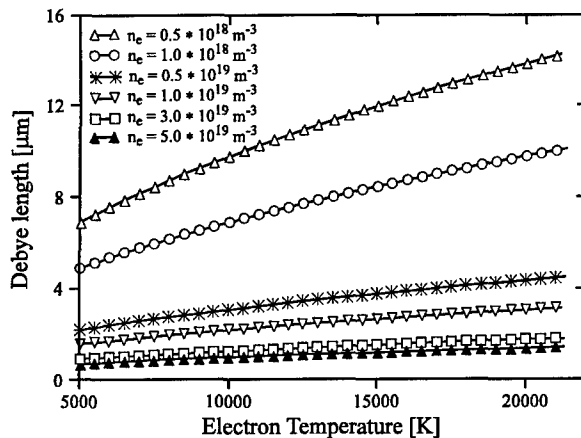


Fig. A7.2: Debye length as a function of n_e and T_e

As can be seen in Fig. A7.3, in the MPD tunnels it is expressed in mm.

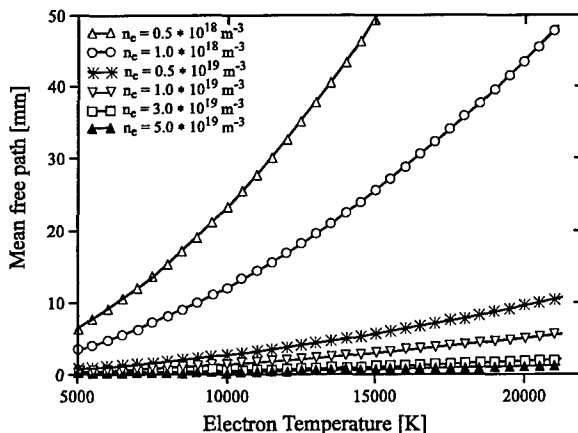


Fig. A7.3: Mean free path as a function of n_e and T_e

The current that flows to a probe's surface depends on the mean free path λ_{ei} of the charge carrier and the Debye length λ_D in the space charge layer and on the probe radius r . The relationships between these parameters determine whether the movement of the charge carriers in the space charge layer is influenced by a shock.

If the probe radius can be chosen so that

$$\lambda_{ei} \gg r \gg \lambda_D \quad (A7.4)$$

is fulfilled, then a so-called conventional shockless thin space charge layer can be assumed.

In an MPD tunnel partial densities of the charged particles in the investigated regions of the air plasma flow, ranging from $x = 50$ mm to 500 mm axial distance to the MPG, are in the range of $n_e = 10^{17}$ to 10^{21} m^{-3} . With electron temperatures T_e of 5000 to 30000 K, this results in Debye lengths of $\lambda_D < 40$ μm .

The Coulomb mean free paths are in the range of $\lambda_{ei} \geq 1$ mm.

The shockless theories developed for stationary plasmas and cylindrical probes can also be applied to flowing, shockless plasmas when the cylindrical probes with a length l are aligned with the plasma flow and $l/\lambda_D \gg 1$ is fulfilled. In the case of larger Debye lengths the plasma layer is enlarged at the front surface of the probe and the ion current to this surface compared with the ion current to the cylindrical surface of the length l can no longer be neglected. The ratio l/λ_D is proportional to the so-called end effect parameter τ_1 which is a criterion for the portion of current to the front surface of a cylindrical probe aligned with the plasma flow. For $\tau_1 > 50$ this amount of current is negligible.

Table 7.1 gives an overview of the probes typically used for plasma diagnostics and the plasma parameters which can be determined with each one.

Probe	Parameters
Single probe	Electron temperature T_e , electron density n_e , plasma potential, electron energy distribution
Double probe	Electron temperature T_e , electron density n_e
Triple probe	Electron temperature T_e , electron density n_e
Time of flight probe	Plasma velocity
Electrostatic angle probe	Plasma flow line
Rotation electrostatic probe	Plasma flow line
Electrostatic crossed probe	Plasma velocity at known ion temperature ion temperature at known plasma velocity

Tab. 7.1 Various probes and their determinable plasma parameters

A7.1 Electrostatic Single Probe

The measurement diagnostic while operating electrostatic single probes consists of determining the current-voltage characteristic. By applying external voltage between the single probe electrode and a reference electrode in contact with the plasma, the probe potential V is varied with respect to the surrounding plasma and therefore the thickness of the space charge layer is changed. Figure A7.4 depicts a typical current-voltage characteristic.

Here the entire current to the probe consists of the ion current I_i and the electron current I_e components. The single probe characteristic curve can be divided into three areas: ion saturation A, transition region B and electron saturation C.

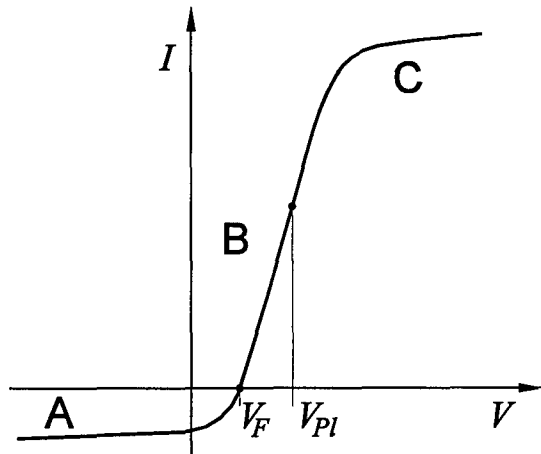


Fig. A7.4: Typical single probe current-voltage characteristic

For large negative probe voltages all electrons are rejected by the probe; only ions are drawn by the probe resulting in an ion saturation current. For lower negative probe voltages in the electron retarding region of the probe characteristics, an increasing amount of electrons contributes to the net current drawn by the probe while the ion current portion decreases. At the floating potential V_F no net current is drawn since the ion current I_i equals the electron current I_e . If the probe voltage reaches the point V_{Pl} , the space charge zone disappears because there is no longer a potential difference between the probe and the plasma. Therefore, V_{Pl} is referred to as *plasma potential*. At probe voltages positive with respect to the plasma potential V_{Pl} , the ions are rejected and only electrons contribute to the probe current. Saturation is reached when due to the electron mobility more electrons can no longer be supplied from the plasma.

The electron saturation current is substantially higher than the ion saturation current due to the higher mobility of the electrons. The ratio of the two currents is given by:

$$\frac{I_e}{I_i} \approx \sqrt{\frac{m_i T_e}{m_e T_i}} \quad (\text{A7.5})$$

Electron Temperature

The shape of the probe characteristic especially in the electron retarding region, where the transition from ion to electron current occurs, is governed by the electron energy distribution function. If the electron current to the probe is calculated assuming Maxwell distribution, the result is a simple equation for determining the electron temperature:

$$\frac{d \ln(I_e)}{dV} = \frac{e}{k T_e} \quad (\text{A7.6})$$

For a Maxwellian electron energy distribution function, the electron temperature T_e can therefore be obtained by plotting the slope of the logarithmic electron current in the retarding region versus the probe potential.

The electron current plotted logarithmically against the probe potential in the transition area B has to result in an even integer (see Fig. A7.5). The value of the increase of these even integers is required to determine the electron temperature. In practice, however, an evaluation in the region of the floating potential V_F has been proven to be most reliable.

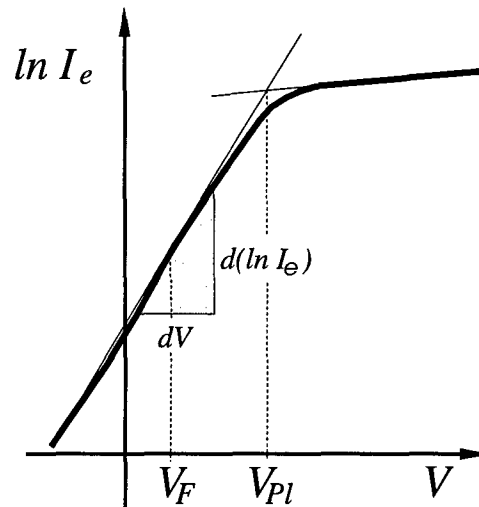


Fig. A7.5: Determining the electron temperature

The electron current in region B is determined from the current-voltage characteristic (Fig. A7.4) in that one first of all determines the ion current by means of a linear extrapolation from the ion saturation current. This is then subtracted from the measured total current.

Plasma Potential

The plasma potential can also be determined from Fig. A7.5. The plasma potential V_{Pl} is given by the crossing point of the extrapolated linear electron retarding region and the saturation region of the logarithmic electron current.

Electron Density

The ion current is calculated to determine the electron density. Assuming quasi-neutrality Laframboise did this for a probe in a parallel flow taking the thermal non-equilibrium into account.

According to Laframboise's theory [A7.3], the ion current I_i to a single probe aligned with the plasma is given by

$$I_i = A e n_e \sqrt{\frac{k T_e}{2 \pi m_i}} i_i \left(\chi_p, \frac{T_i}{T_e}, \frac{r}{\lambda_D} \right) \quad (\text{A7.7})$$

The correction factor i_i depends on the normalized plasma potential $\chi_p = e(V_{Pl} - V_p) / k T_e$, the Debye ratio r / λ_D and the temperature ratio T_e / T_i . The correction factor can be set to 1 in good approximation if the Debye ratio is greater than 50, which can be achieved by choosing the corresponding probe radius r in accordance with this requirement and if the

ion current is obtained by the extrapolation of the saturation current region to values of small normalized probe potentials χ_p .

Electron Energy Distribution

An essential requirement of the single probe theory introduced here is the assumption of a Maxwell distribution of the electron energies. The validity of this assumption in the plasma which has been examined can be proven rather easily based on the linearity of the logarithmized electron current in the transition region of the probe characteristic curve as shown in Fig. A7.5. Due to high local heat input, deviations from this energy distribution may occur so that it is no longer possible to exactly determine the electron temperature based on the electron current increase of a single probe measurement.

According to Fig. A7.6, the electrons on the center line at a distance of $x = 117$ mm to the exit of the MPG are non-Maxwellian. It can be clearly seen from Fig. A7.6 that for the other positions the electrons do have a Maxwellian energy distribution.

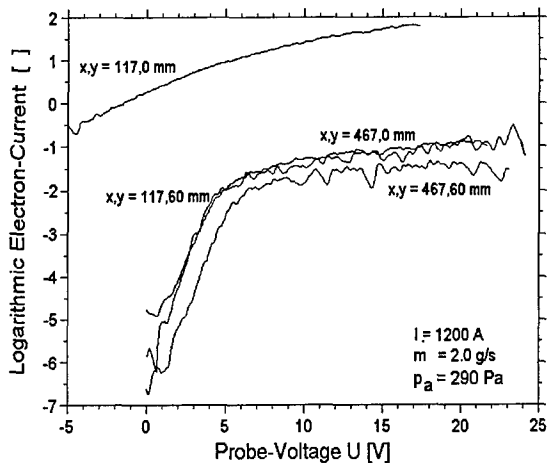


Fig. A7.6: Semi-logarithmic plots of the electron currents to a single probe at different x, y positions to the MPG exit

In the case of deviations from the Maxwellian electron velocity or distribution, i.e. one has a different isotropic distribution function, this distribution function can be obtained from the probe characteristic in the retarding region at $V_S < V_{PL}$. The shape of the second derivative of the electron current I_e to a single probe with respect to the probe voltage U is proportional to the shape of the distribution function of the electrons which can be numerically fitted. To do this, the plasma potential V_{PI} must be known since the probe potential must be measured with respect to the plasma potential. In the electron retarding region of the probe characteristic, the change of probe current is mainly driven by the change in the electron current part which is much greater than the change in the ion current. Thus it can be assumed that the second derivative of the total probe current is

essentially the same as the second derivative of the electron current.

If the electron current I_e is differentiated twice with respect to U , one yields

$$[f(E)]_{E=-eU} = \frac{-1}{A 2e\pi} \left(\frac{m_e}{e}\right)^2 \frac{d^2 I_e}{dU^2}; \quad U < 0 \quad (A7.8)$$

for the velocity distribution function $f(E)$ and

$$F(E) \Big|_{E=eU} = -\frac{4}{A e^2} \sqrt{\frac{-m_e U}{2e}} \frac{d^2 I_e}{dU^2} \quad (A7.9)$$

for the energy distribution function of the electrons.

In Figs. A7.7 and A7.8 the experimentally obtained electron energy distribution functions at two different positions in the air plasma are shown. For reasons of comparison, Fig. A7.7 also shows a theoretical Maxwell distribution function at an appropriate electron temperature T_e .

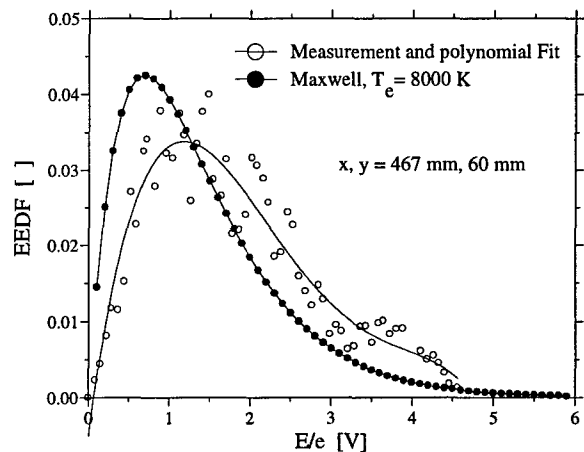


Fig. A7.7: Experimental and theoretical (Maxwell) electron energy distribution function at $x, y = 467$ mm, 60 mm

Figure A7.8 shows the experimentally obtained electron energy distribution function on the plasma flow center line at $x = 117$ mm. High energy electrons are dominant.

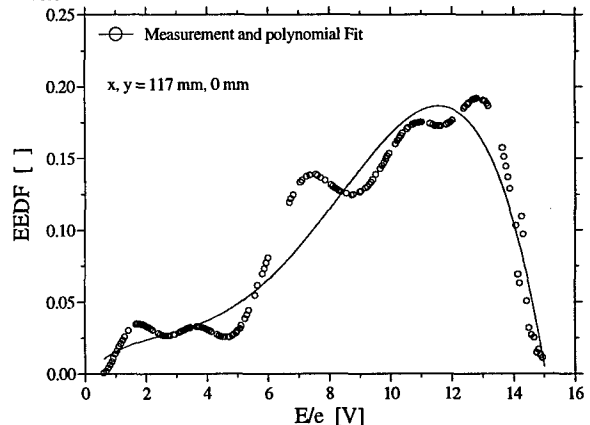


Fig. A7.8: Experimental electron energy distribution function at $x, y = 117$ mm, 0 mm

Experimental Set-up

Figure A7.9 shows the design of a typical single probe. For use in MPD tunnels the probe itself consists of a tungsten wire with a diameter of 0.1 to 1 mm and an effective length of 5 to 20 mm. The rest of the wire is insulated from the probe clamp by means of a small aluminum tube.

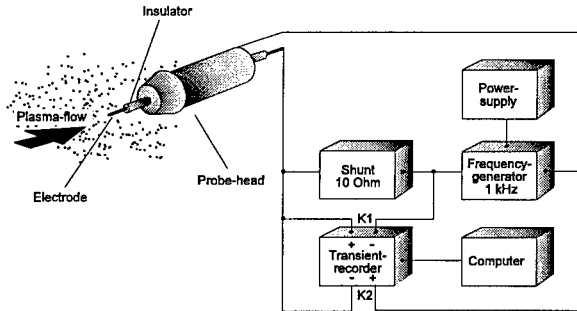


Fig. A7.9: Experimental design for single and double probe measurements

A power pack supplies voltage of ± 30 V which is modulated in the form of a sine or saw tooth signal from a portable generator. This voltage variation is established as probe potential. The modulation across the entire voltage region is done with a frequency of up to 10 kHz. The probe potential is measured directly and the probe current is measured at a precision resistance. The measurements are recorded with a oscilloscope or transient recorder.

A7.2 Electrostatic Double Probe

A double probe consists of two cylindrical probe electrodes whose distance to each other has to be more than several Debye lengths so that any kinds of disturbances can be ruled out. Normally the surfaces of both electrodes are the same size. This condition should be assumed for the following.

Voltage is created between the two electrodes and the flowing current is measured. Each electrode can be considered to be a single probe with the other electrode acting as the reference. The theory of the double probe characteristic can, therefore, principally be derived from the theory for single probes.

If the potential of a probe electrode (electrode 1) is negative compared to the plasma after applying external voltage V , then there is a continuous decrease of the electron current portion until ion saturation is reached. If the external voltage is 0, both probe electrodes float and the resulting total current disappears. In the case of polarity reversal of the double probe, electrode 2 becomes more and more negative compared to the plasma potential and finally reaches ion current saturation. Electrode 1 compensates for this ion current with an appropriately large electron current. In this way, contrary to the single probe, the double probe with equal surface areas

never reaches the point of electron saturation. Figure A7.10 shows a typical double probe characteristic curve.

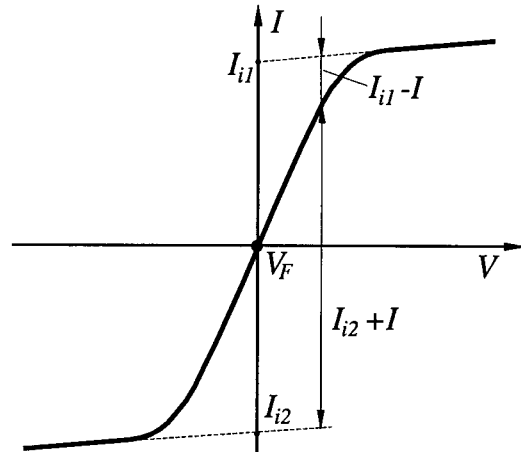


Fig. A7.10: Double probe characteristic curve for electrodes with equal surface area

Only high energy electrons penetrate the plasma sheath near the floating potential V_F and contribute to the net current. This means that the double probe is less sensitive to low energy deviations from the assumption of Maxwell electron energy distribution (see Fig. A7.7).

Electron Temperature

The electron temperature T_e is obtained by the equation (A7.10):

$$\left. \frac{dI}{dV} \right|_{V=0} = \frac{I_{i1} I_{i2}}{I_{i1} + I_{i2}} \frac{e}{k T_e} \quad (\text{A7.10})$$

The ion currents I_{i1} and I_{i2} are extrapolated from the saturation regions of the characteristic to the floating potential V_{PL} where no current is drawn (see Fig. A7.10).

Electron Density

The electron density can be determined from a double probe measurement with the same equation as with a single probe measurement Eq. (A7.7). However, a mean ion current has to be determined. With a double probe with equal surface areas this is obtained from

$$\bar{I}_i = \frac{|I_{i1}| + |I_{i2}|}{2} \quad (\text{A7.11})$$

The decision whether one uses a single or a double probe is based on the advantages and disadvantages of each method. Single probe measurements and the evaluation can be performed quickly due to the low Debye lengths and the resulting negligible ion current correction factor. These probes are smaller and allow for a better local resolution of the plasma parameters. However, single probes used to determine the electron temperature and density reach their limits as soon as significant deviations of the electron energies

from the Maxwell distribution appear. An additional disadvantage is that the distance between the reference electrode and the single probe is usually quite large and therefore the probe characteristic can be influenced by changes in the plasma potential between the two electrodes. Moreover, a thermal overload and destruction can be easily caused by the high electron current load of a single probe which results in an increased burning off of the probe electrodes with erosive plasmas. With a double probe, the load from the current is lower due to the essentially smaller ion current saturation, which in this case is the maximum current load. The number of electrons in a double probe current is limited to the high energy electrons, i.e. a double probe measurement is less susceptible to deviations of the electron energy distribution. The disadvantages of the double probe, the larger size and lower local resolution of the measurement, can usually be compensated for with the smaller changes of the plasma potential between the electrodes. The technical performance and the construction of a double probe only differs from a single probe in that the voltage is established between the two probes.

A7.3 Electrostatic Triple Probe

A major disadvantage of single and double probes for plasma wind tunnel applications is that the heat load during the measurement of the probes in the plasma jet is very high due to the time needed to obtain the full probe characteristics at any measurement point. In addition, the current to the probe often results in high thermal loads, leading to extensive erosion in the chemically reacting air plasma. With an electrostatic triple probe, for example, the whole radial distribution of the electron temperature and the electron density can be measured by a fast radial motion of the probe through the investigated plasma jet. No further evaluation of characteristics taken at specific radial test positions is necessary.

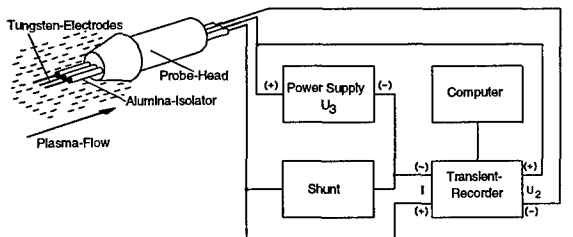


Fig. A7.11: Triple probe measurement set-up

As shown in Fig. A7.11, the electrostatic triple probe consists of three electrodes identical in surface area A , two of them (1, 3) connected to a double probe and a third (2) floating with respect to the plasma.

Electron Temperature

In a collisionless thin sheath of plasma at the probe surface, the current to each electrode at a potential V can be expressed by:

$$-I_1 = A j_i (V_1) - A j_e \exp(-eV_1/kT_e), \quad (\text{A7.12})$$

$$I_2 = A j_i (V_2) - A j_e \exp(-eV_2/kT_e), \quad (\text{A7.13})$$

$$I_3 = A j_i (V_3) - A j_e \exp(-eV_3/kT_e). \quad (\text{A7.14})$$

Without an externally applied potential difference between the double probe circuit and the floating electrode, the current I_2 to the floating electrode will be zero. By assuming no variation in ion current density j_i in the probe region, one obtains from the current ratio:

$$U_2 = \frac{kT_e}{e} \left[\ln 2 - \ln(1 + \exp(-eU_3/kT_e)) \right], \quad (\text{A7.15})$$

with $U_2 = V_2 - V_1$ and $U_3 = V_3 - V_1$. For an externally applied fixed potential difference U_3 in the double probe circuit, an electron temperature dependent potential voltage difference U_2 can be measured between the double probe and the floating electrode. By moving the probe through the plasma, direct radial or axial distribution of T_e can be measured.

Electron Density

Since the ion current density j_i depends on the electrode potentials, the assumption of equal ion current densities is not quite correct even for the thin sheath case. Therefore, Chen and Sekiguchi derived an approximate expression for the ion current density which includes a correction factor β [A7.4]. This correction factor scales the potential difference with respect to the floating potential V_F . The correction factor β can be calculated from the equation

$$\exp\left(-\frac{eV_F}{kT_e}\right) = 0.6577 \sqrt{\frac{m_i}{m_e} \left(1 - \beta \left(V_F - \frac{e}{2kT_e}\right)\right)} \quad (\text{A7.16})$$

by using one of the triple electrodes as a single probe in order to determine the floating potential V_F and the electron temperature as described in Eq. (A7.1). Using this correction, one obtains:

$$\frac{1}{2} \frac{1 - \left(\sqrt{1 - \beta U_2} + \sqrt{1 + \beta(U_3 - U_2)}\right)}{1 - \exp\left(-\frac{eU_3}{kT_e}\right)} * 0.5 \exp\left(-\frac{eU_2}{kT_e}\right) \quad (\text{A7.17})$$

to determine the electron temperature.

In Fig. A7.12 the correction factor β is plotted as function of electron temperature for different gases. Without this correction the electron temperatures are overestimated by 20% at the most.

From the collisionless probe theory and the measured current I in the double probe circuit under the assumption of constant current density j , the electron number density is determined by:

$$n_e = \frac{\sqrt{m_i I}}{A} \frac{\sqrt{e}}{e \sqrt{kT_e} \left[\exp(-eU_2/kT_e) - 1 \right]}. \quad (\text{A7.18})$$

Without this correction factor the electron density is overestimated by a maximum of 40% according to the theory of Chen and Sekiguchi with respect to Eq. (A7.15). The equation for the electron density changes to:

$$n_e = \frac{\sqrt{m_i I}}{A} \frac{1.05 \cdot 10^9 (1 - \beta (V_F - e / 2kT_e))^{1/2}}{\sqrt{T_e} (\exp(eU_2 / kT_e) - (1 - \beta U_2)^{1/2})} \quad (A7.19)$$

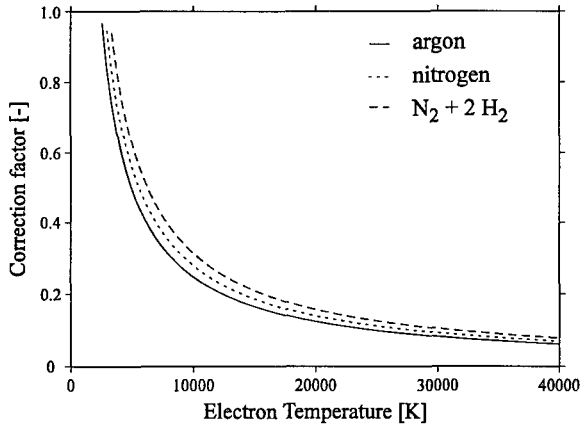


Fig. A7.12: Correction factor β for various plasmas as function of the electron temperature T_e

For the use of the formula given in section A7.3 the electron energy distribution has to be Maxwellian. A correction in the case of a non-Maxwellian energy distribution is impossible without losing the advantage of rapid mobility of this type of probe. In this case a single probe measurement is preferable because of its much higher local resolution.

The wiring of the probe can be seen in Fig. A7.11. Contrary to single and double probe measurements, a saw tooth generator is not necessary. This makes it possible to achieve a substantially higher transport speed of the probe in the plasma beam and therefore a lower thermal load.

Figures A7.13 and A7.14 show cross sections of the electron temperature and density, determined by a double and triple probe respectively, through the plasma beam at a distance of 467 mm from the nozzle end of the plasma generator in an MPD tunnel.

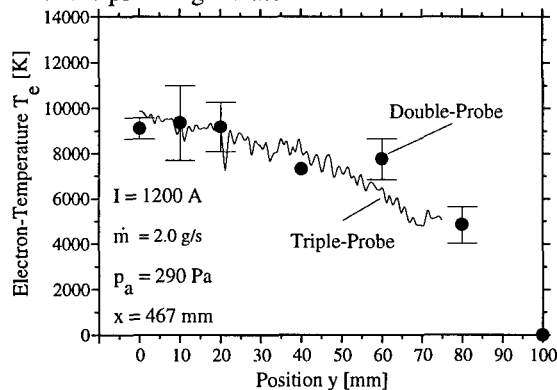


Fig. A7.13: Electron temperature distribution

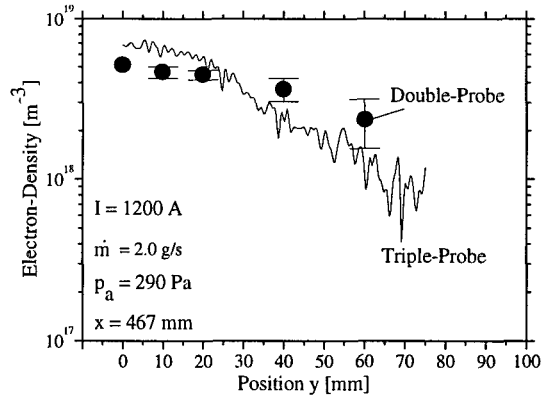


Fig. A7.14: Radial electron density distribution

A7.4 Time of Flight Probe

Time of flight probes are in use for plasma flow measurements. They are electrostatic double probes separated at a known distance and aligned with the flow of the plasma particles as shown in Fig. A7.15.

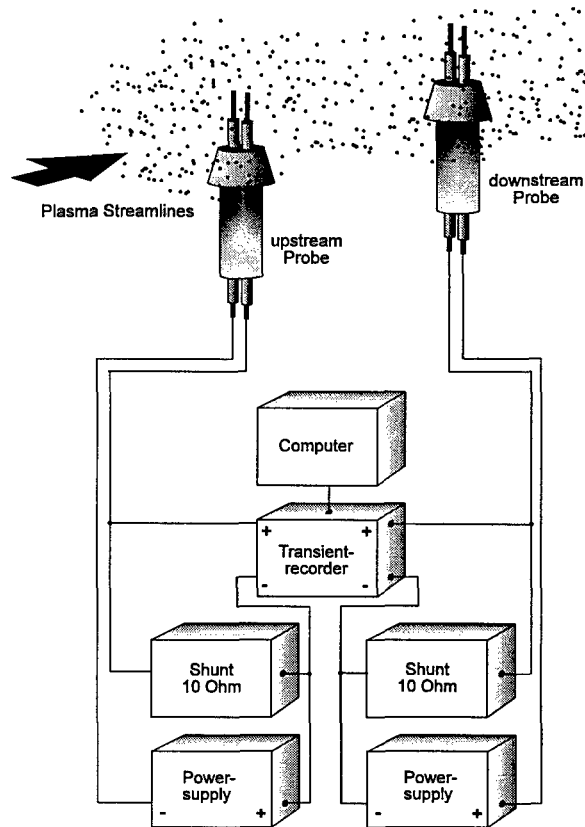


Fig. A7.15: Design of a time of flight probe

Upstream and downstream probes are both biased to draw ion-saturation current. Fluctuations in the local ion number density around a probe result in fluctuations in the detected ion current. By moving with the flow velocity v, those fluctuations are first detected at the upstream probe and then time-delayed at the downstream probe. The method of time of flight probes as described is only applicable within regions with moderate velocity gradients because a relatively large probe separation of about 25-50 mm is needed

to resolve the time delays in high speed plasmas. By performing an FFT-cross-correlation with the two signals, the value of the time shift in respect to the time of flight can easily be determined. With the known separation of the two probes, the velocity of the plasma particles can be calculated.

Within the air plasma of an MPD wind tunnel the natural plasma fluctuation is high enough to use this method. Figure A7.16 shows the axial velocity distribution at the center line of the plasma jet. The velocity measurements, especially those close to the plasma source, were compared to optical velocity measurements using the Doppler shift effect of a nitrogen NI emission line at 746.83 nm, detected with a Fabry-Perot interferometer described in section B4. In Fig. A7.17 the plasma velocity measurements were taken as input values for calculation of the stagnation pressures by the Bernoulli equation. The calculated results already agreed quite well with measurements of the pressure.

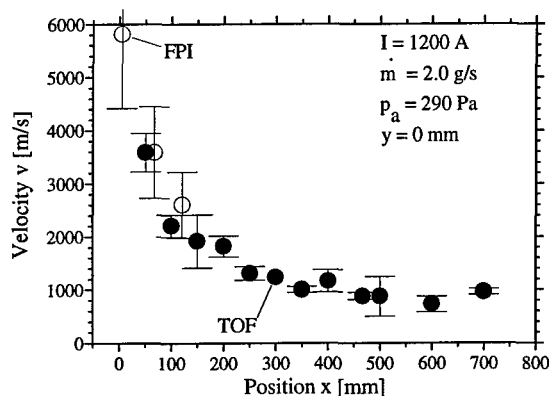


Fig. A7.16: Axial velocity distribution measured with time of flight probes and Fabry-Perot interferometry

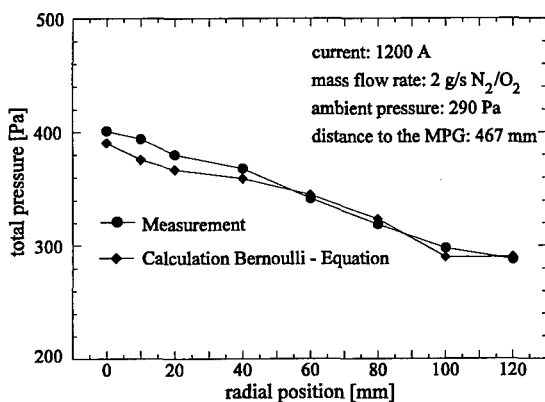


Fig. A7.17: Total pressure distribution

A7.5 Electrostatic Angle Probe

Theoretically formulated and experimentally verified, the ion current to a cylindrical probe in a plasma flow depends strongly on the angle θ between the probe axis and the plasma flow vector [A7.5]. For a probe electrode not aligned with the plasma flow, the kinetic energy of charged particles moving towards

the electrode results in a deformation of the potential sheath around the electrode, in which the charged particles are sampled and contribute significantly to the probe current. For electrodes aligned with the plasma flow vector, only those charged particles which enter the potential sheath by random thermal motion like in stationary plasma contribute to the probe current. In general the ion current to a probe at an angle θ with respect to the velocity vector can be described by the following equation:

$$I_i = \sqrt{\frac{kT_e}{2\pi m_i}} n_e e A \frac{2}{\sqrt{\pi}} \exp\left(-\left(\frac{v_i}{v_{th}}\right)^2 \sin^2 \theta\right) \sum_{n=0}^{\infty} \left(\frac{\left(\frac{v_i}{v_{th}}\right)^n \sin^n \theta}{n!}\right) 2\Gamma\left(n + \frac{3}{2}\right) \quad (\text{A7.20})$$

Here v_i is the directed ion flow velocity, A the probe surface area and v_{th} the thermal velocity given by:

$$v_{th} = \sqrt{\frac{2kT_i}{m_i}} \quad (\text{A7.21})$$

With two different probes this current dependence of the angle is made use of at the IRS: in the case of the rotating electrostatic probe for determining the flow direction and in the case of the so-called electrostatic crossed probe for velocity or ion current measurement.

A7.5.1 Rotating Electrostatic Probe

The flow direction in a diverging plasma flow can be determined based on Eq. (A7.20) using a cylindrical single probe which is rotated as shown in Fig. A7.18.

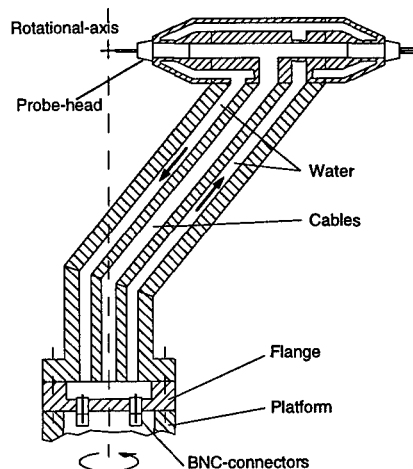


Fig. A7.18: Rotating probe

The variation of the probe angle θ with respect to the flow direction causes a change in the current to the probe which has a minimum in the case of a parallel alignment. In Fig. A7.19 the theoretical course of the probe current for constant values of the flow velocity

v_i while varying the probe angle is shown. Likewise the constant values of the electron temperature T_e , the mass m_i as well as the charge carrier density n_e and the probe surface A influence the shape of the curve but do not change the location of its minimum. While the probe is being turned, a constant negative probe voltage to the ground is applied so that the probe draws ion saturation current.

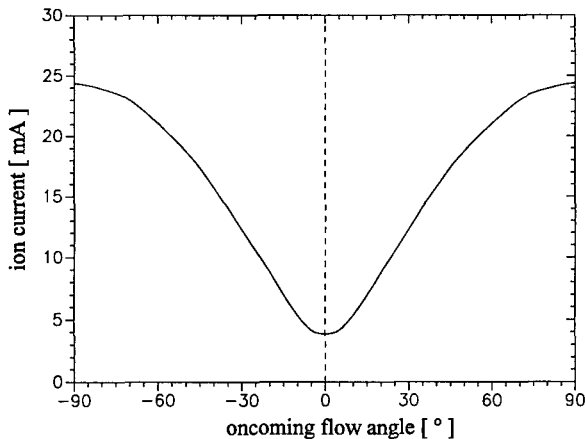


Fig. A7.19: Calculated ion current to a cylindrical probe depending on the oncoming flow angle θ

The current as function of the angle θ can be calculated from the constant rotation velocity of the probe. The angle θ which corresponds to the current minimum then gives the flow direction at the measurement position.

A7.5.2 Electrostatic Crossed Probes

For two single probes with one oriented perpendicular to ($\sin \theta = 1$) and one aligned with the flow vector (see Fig. A7.20) the reaction of the two currents becomes:

$$\frac{I_{iL}}{I_{iF}} = \frac{2}{\sqrt{\pi}} \exp\left(-\left(\frac{v_i}{v_{th}}\right)^2\right) \sum_{n=0}^{\infty} \left(\frac{(v_i/v_{th})^n}{n!}\right) 2\Gamma\left(n + \frac{3}{2}\right). \quad (\text{A7.22})$$

If the ion temperature and therefore with Eq. (A7.21) the thermal velocity is known, the directed ion velocity v_i can be derived from the current ratio [A7.6]. By knowing the directed velocity of the plasma from time of flight measurements, for example, the ion temperature T_i can be calculated using Eq. (A7.22).

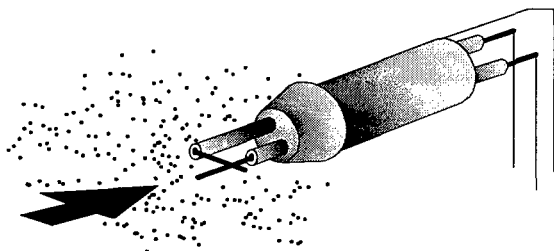


Fig. A7.20: Measurement head with crossed single probes

There are some crucial assumptions underlying the crossed probe method. To obtain the correct current ratio, the surface area of both probes must be known or assumed to be equal as in the case of Eq. (A7.22). Especially in chemically reacting air plasmas, a high erosion rate of the perpendicular electrode is observed, which has to be taken into account. Within supersonic flows like in MPG plasmas, the effective area of the perpendicular probe is reduced due to a shock effect. The errors are therefore quite large with this method. They are at about $\pm 50\%$ of the absolute value for the ion temperature T_i and at about 20% for the ion velocity v_i based on experience at the IRS.

References

- [A7.1] Habiger, H., Auweter-Kurtz, M., "Investigation of High-Enthalpy Air Plasma Flow with Electrostatic Probes", *Journal of Thermophysics and Heat Transfer*, Vol. 12, No. 2, April-June 1998, S. 198-205; also AIAA-96-1864, 31st AIAA Thermophysics Conference, New Orleans, LA, June 1996.
- [A7.2] Habiger, H., "Elektrostatische Sonden und Fabry-Perot Interferometrie zur Untersuchung von lichtbogenbeheizten Plasmen für Triebwerksanwendungen und Wiedereintrittssimulation", Dissertation, Universität Stuttgart, 1994.
- [A7.3] Langmuir, I., "The Collected Works of Irving Langmuir", ed. by C. Suits, Pergamon Press Inc., New York 1961.
- [A7.4] Chen, S.L., Sekiguchi, T., "Instantaneous Direct-Display System of Plasma Parameters by Means of Triple-Probe", *Journal of Applied Physics*, Vol. 36/8, 2363, August 1965.
- [A7.5] Kanal, M., "Theory of Current Collection of Moving Cylindrical Probes", *Journal of Applied Physics*, Vol. 35, No. 6, June 1964, p. 1967.
- [A7.6] Poissant, G., Dudeck, M., "Velocity Profiles in a Rarefied Argon Plasma Stream by Crossed Electrostatic Probes", *Journal of Applied Physics*, Vol. 58, No. 6, Sept. 1985.

A8 Mass Spectrometer Probes

Mass spectrometry allows the particle densities and the energy distributions of the neutrons and ions in a free stream plasma to be determined and is used to determine the plasma flow composition [A8.1, A8.2] as well as to investigate the erosion behavior [A8.3, A8.4] and catalytic effects [A8.5, A8.6] of heat shield materials in the PWK plasma flows.

The mass spectrometer used at the IRS is based on a VG Quadrupole [A8.7] SXP300/CMA500 and consists of an open electron impact ion source, a cylindrical mirror energy analyzer (CMA, 0 - 50 eV), a triple filter quadrupole (0 - 300 amu) and a channeltron (see Fig. A8.1). In front of the ion source an ion transfer optic (ITO) is installed, a small aperture lens, with which external ions can be focused into the CMA while the ion source is switched off. In the case where neutrals are detected, a reflecting potential for

positive ions is applied to the ITO and the ion source is switched on. Thus, mass scans at a constant energy level and energy scans at a constant mass can be carried out for neutral as well as ionized plasma particles [A8.8].

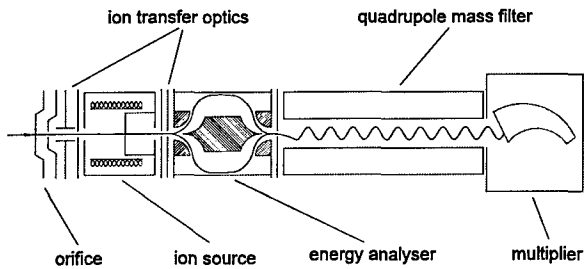


Fig. A8.1: Set-up of the mass spectrometer

The mass spectrometer is situated inside the vacuum chamber of the plasma wind tunnel (see Fig. A8.2). Therefore, the whole spectrometer is protected by a stainless steel housing and a water-cooled copper heat shield against the high heat loads and the erosive environment. All equipment is placed outside the vacuum chamber, i.e. the electrical support is made through a flexible tube under atmospheric pressure while the vacuum support is done with a CF100 bellow, which also serves the mobility of the spectrometer.

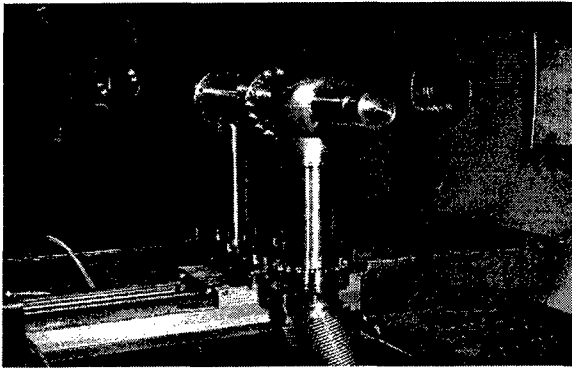


Fig. A8.2: Mass spectrometer probe in PWK 1

One-Stage System

The spectrometer head MS-1 is shown in Fig. A8.3. This one-stage configuration is used to determine the plasma composition at low pressures. The orifice opening (diameter 100 μm , length 100 μm) is drilled into a tungsten plate (diameter 39 mm, thickness 4 mm) with an excimer laser. This plate is cooled by a special cooling body. The spectrometer head is electrically insulated from the rest of the housing, thus the orifice is floatable. In case of high pressures (> 100 Pa) a tungsten foil instead of the tungsten plate is used yielding again a length to diameter ratio for the orifice of $L/d = 1$ for all measurements (opening diameter 40 μm). The orifice opening also serves as a one-staged differential pumping system.

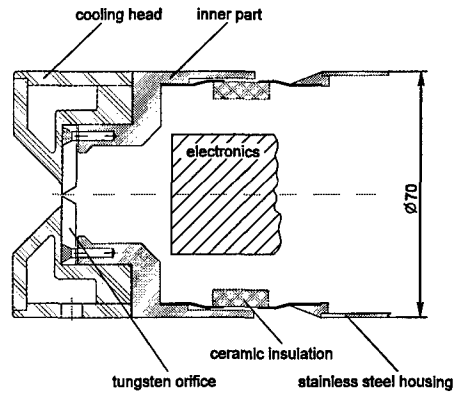


Fig. A8.3: Set-up of the spectrometer head with orifice opening

The ITO is placed 32 mm behind the orifice opening. Therefore, long paths inside the spectrometer leading to particle losses are avoided.

For calibration purposes a special test stand has been built at the IRS [A8.9]. The spectrometer was calibrated with neutrals, external atoms and external ions to show the function and accuracy of the CMA for energy analysis, the relative sensitivities of the spectrometer for different masses and to demonstrate the influence of the orifice opening on the sampling of atoms and ions as well as the influence of a space charge sheath in front of the orifice on the measured ion energies [A8.2].

The CMA was shown to measure with an error of ± 0.5 eV in the relevant energy region of 0 - 50 eV. The normal fluctuation of the signal within an energy scan of a neutral particle is around 10%. In contrast it was observed that for plasma ions, which have a very high intensity (e.g. N^+ with up to 10^6 counts/s), these fluctuations can increase to 20%. The mass resolution of the quadrupole is set to $\Delta m/m = 1$, i.e. neighbored masses like water ($m = 17, 18$) can be resolved, but not that of certain molecules like N_2 and CO ($m = 28$). To distinguish between molecules with the same mass number and between particles which were produced inside the plasma and enter the spectrometer and those which were produced inside the ion source, the particles' ionization potentials can be used [A8.10]. Therefore, the electron impact energy of the ion source was lowered from 70 eV to 17 eV. Here, dissociation of a molecule, e.g. O_2 , and subsequent ionization of the fragment, O, is not possible. Thus, O atoms detected inside the plasma jet at this electron energy can be attributed entirely to the plasma. Additionally, a reference spectrum of the residual gas inside the spectrometer can easily be subtracted from the data measured inside the plasma jet.

As a typical result, the composition of a nitrogen plasma at a stagnation pressure of 130 Pa is shown in Fig. A8.4.

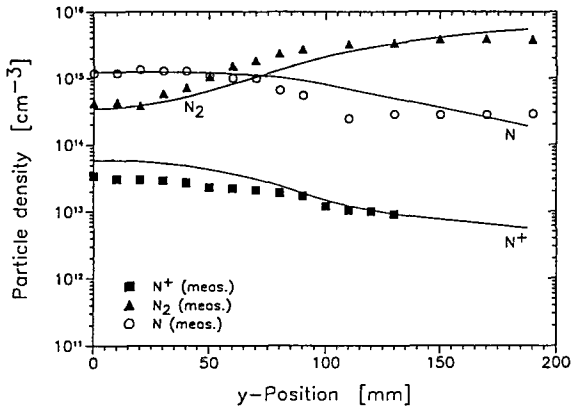


Fig. A8.4: Comparison of mass spectrometric data and results of the numerical simulation of the 130 Pa test case [A8.6]

One-stage configurations of different shapes were used for the investigation of catalytic effects [A8.6]. They allow operation at different surface temperatures and with different coatings of the orifice region. In Fig. A8.5 the distribution of nitric oxide with different coatings and configurations is shown as an example.

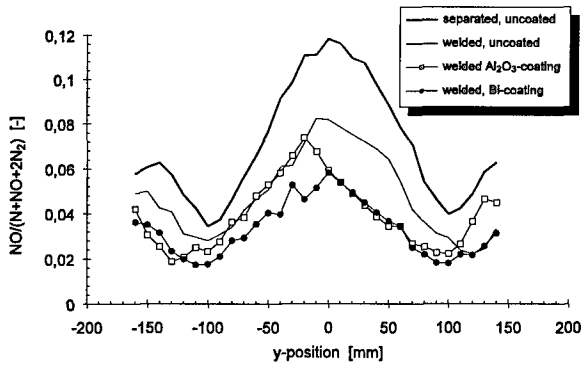


Fig. A8.5: Distribution of nitric oxide with different cooling heads and coatings in air plasma

Two-Stage System

For measurements at higher ambient pressures, a two-staged system MS-II was designed for pressures up to 1 kPa [A8.5] which is shown in Fig. A8.6.

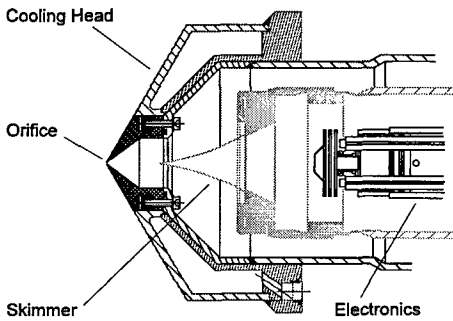


Fig. A8.6: Two-stage mass spectrometer inlet system

The inlet system was built with an additional pumping stage between the tungsten orifice and the spectrometer housing. With this two-stage design it

was possible to increase the orifice diameter to 400 μm. The second stage is equipped with a nickel skimmer of 100 μm orifice diameter and a total wedge angle of 35°. Between the orifice and the skimmer a pressure of 0.01 - 1 Pa is achieved. According to the investigation of Pertel [A8.11], due to interactions with the residual gas molecules, the supersonic free jet generated from the orifice is enclosed by a shock barrel at the side and by a normal shock (Mach disk) at the front of the jet. To avoid changes of the chemical composition of the extracted plasma jet, it is absolutely vital that the tip of the skimmer be placed at a distance from the orifice smaller than the distance of the Mach disk X_M . Ashkenas and Sherman [A8.12] showed that this axial distance is given by

$$x_M = 0.67 \sqrt{\frac{P_0}{P_1}} d \quad (A8.1)$$

For a chosen orifice diameter d and a total pressure of 290 Pa, for example, the equation above states that the orifice to skimmer distance must be less than 12 mm. The MS-II configuration was used for catalytic investigations with different orifice materials [A8.6]. In Fig. A8.7, the ratio of NO/N_2 is shown with a tungsten and an SiC orifice, respectively.

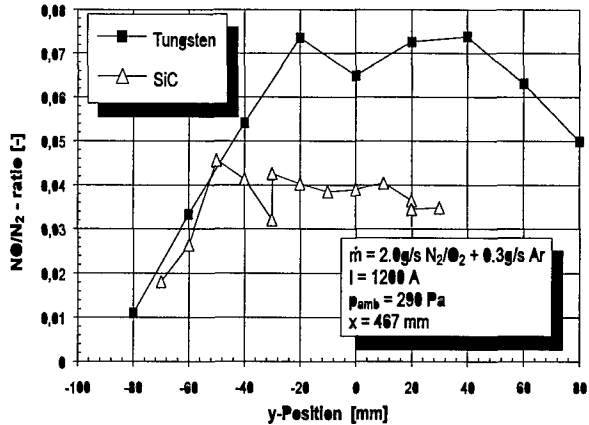


Fig. A8.7: NO/N_2 -ratio measured with a tungsten and a SiC-orifice, respectively

Configuration for Material Investigation

The third configuration of MS-III (Fig. A8.8) was built to examine the erosion behavior of ceramic heat shield materials. For this purpose, the material sample has to be arranged uncooled just in front of the spectrometer orifice [A8.13, A8.14]. The erosion products are extracted by the same pinhole diameters as in the MS-I configuration.

This configuration has been used for the on-line investigation of the erosion behavior of different coatings as well as for the investigation of the passive/active transition of the oxidation of SiC.

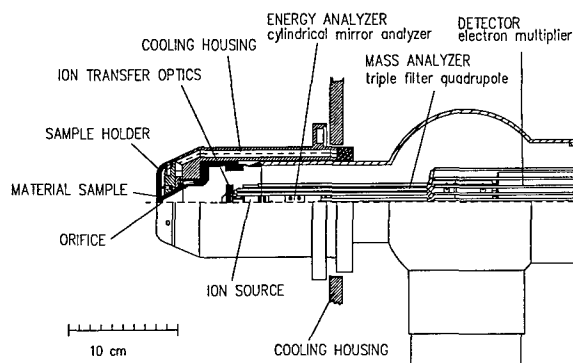


Fig. A8.8: MS-III configuration

As an example, Fig. A8.9a shows the time dependence of the ion percentage of mass 28 which represents Si and CO using a coated C/C-SiC sample. The corresponding temperature history of the sample is plotted in Fig. A8.9b. After 15s at a temperature of about 1400°C, a rapid increase of the signal can be seen. A surface temperature of 1670°C was reached after 30 seconds when the steep decrease of the signal occurs.

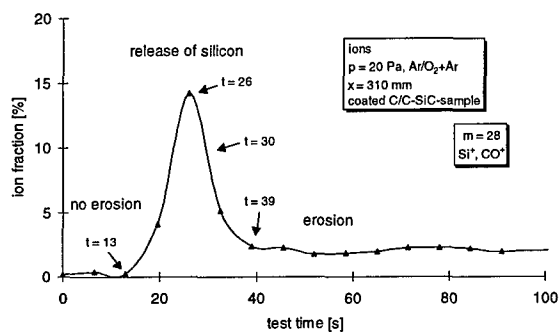


Fig. A8.9a: Erosion behavior

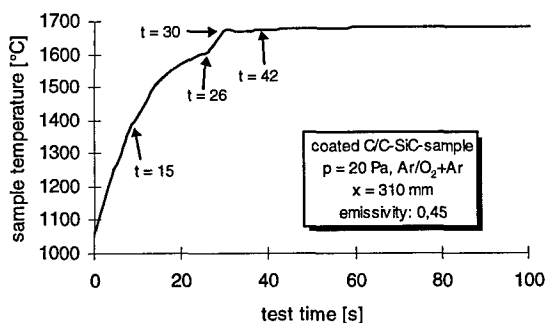


Fig. A8.9b: Temperature history of a coated C/C-SiC sample

References

- [A8.1] Schönemann, A., Auweter-Kurtz, M., "Mass Spectrometric Investigation of High Enthalpy Plasma Flows", *Journal of Thermophysics and Heat Transfer*, Vol. 9, No. 4, Oct.-Dec. 1995, pp. 620-628.
- [A8.2] Schönemann, A., "Massenspektrometrie zur Untersuchung lichtbogenbeheizter Plasmen in Niederdruck-Plasmawindkanal", Dissertation, Universität Stuttgart, 1994.
- [A8.3] Stöckle, T., Winter, M., Auweter-Kurtz, M., "Simultaneous Spectroscopic and Mass Spectroscopic

Investigation of Surface Catalytic Effects in High Enthalpy Gas Flows", AIAA-98-2845, 7th AIAA/ASME Joint Thermophysics and Heat Transfer Conference, Albuquerque, NM, 1998.

- [A8.4] Dabalà P., Auweter-Kurtz, M., "Mass Spectrometric Investigations of Erosion Behavior of Thermal Protection Materials", ESA 2nd European Workshop on Thermal Protection Systems, Stuttgart, Germany, October 1995.
- [A8.5] Stöckle, T., Auweter-Kurtz, M., Laure, S., "Material Catalysis in High Enthalpy Air Flows", AIAA-96-1904, 31st AIAA Thermophysics Conference, New Orleans, LA, 1996.
- [A8.6] Schönemann, A., Auweter-Kurtz, M., "Characterization of Nitrogen and Air Plasma Flows by Mass Spectrometry", ISPC 11, Proceedings of the 11th International Symposium on Plasma Chemistry, Loughborough, UK, 1993, pp. 458-463.
- [A8.7] Batey, J.H., "Quadrupole Gas Analyzers", *Vacuum* 37/8, 1987, pp. 659-668.
- [A8.8] Schönemann, A., Auweter-Kurtz, M., Habiger, H., Sleziona, C., Stöckle, T., "Experiment and Numerical Investigation of the Influence of Argon Used a Protection Gas in a Reentry Simulation Device", 28th Thermophysics Conference, AIAA-93-2829, Orlando, FL, 1993.
- [A8.9] Auweter-Kurtz, M., "Meßverfahren für strömende Plasmen", IRS-94-M1, Institut für Raumfahrtssysteme der Universität Stuttgart, 1994.
- [A8.10] Litzow, M.R., Spalding, T.R., "Mass Spectrometry of Inorganic and Organometallic Compounds", Elsevier Scientific Publishing Co., Amsterdam, 1973, chapter 3.
- [A8.11] Pertel, R., "Molecular Beam Sampling of Dynamic Systems", *Int. J. Mass Spectrom. Ion Phys.*, 16, (1975), 53.
- [A8.12] Ashkenas, A., Sherman, F.S., "The Structure and Utilization of Supersonic Free Jets in Low Density Wind Tunnels", 4 RGD 84, 1966.
- [A8.13] Dabalà, P., Auweter-Kurtz, M., "Mass Spectrometric Erosion Measurements of Ceramic Thermal Protection Materials in High Enthalpy Plasma", AIAA-97-2590, 32nd Thermophysics Conference, Atlanta, GA, 1997.
- [A8.14] Dabalà, P., Auweter-Kurtz, M., "Investigation of the Erosion Behavior of Graphite and Silicon Carbide by Mass Spectrometry", 12th International Symposium on Plasma Chemistry, Minneapolis, MN, 1995.

A9 Radiometer Probe

Radiometer probes are mainly used to determine the radiation heat flux. By using appropriate filters, however, conclusions about the gas composition can also be made. The radiation intensity of the plasma rises with the fourth power of the gas temperature when only the continuum part of the plasma radiation is taken into account. The following is approximately valid for the radiation heat flux. Whereby the degree of emission of the plasma can be smaller than that of the thermal protection material depending on the plasma condition:

$$\dot{q}_{\text{radiation}} \sim \epsilon_{\text{plasma}} T_{\text{plasma}}^4 - \epsilon_{\text{wall}} T_{\text{wall}}^4 \quad (\text{A9.1})$$

At plasma temperatures of 10000 K and higher and at pressures of up to 10 kPa, the radiation heat flux can generally no longer be neglected and reaches the same order of magnitude as the convective part. Figure A9.1 shows, for example, calculated heat fluxes for the entry of the Huygens probe into the atmosphere of the Saturn moon Titan.

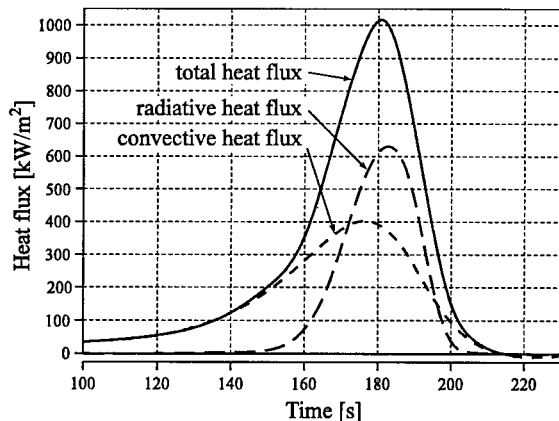


Fig. A9.1: Calculated heat fluxes for the entry of the Huygens probe into the $N_2/Ar/CH_4$ atmosphere of the Saturn moon Titan (without catalytic effects)

In ground test facilities a detector can be placed perpendicular to the plasma beam or to the shock front to measure the radiation heat fluxes. The measurement devices are then located outside of the evacuated test chamber and the optics are focused on the test point through windows or light wave conductors. This stipulates long distances to the measurement position along which radiation can be absorbed and the measurable wavelength region remains limited to the transmission area of the windows or the light wave conductors.

The more direct way is to place the radiometer in a probe which is directly exposed to the plasma. For this purpose a radiometer probe, shown in Fig. A9.2, was developed at the IRS. Various glass shields, filters and detectors can still be used as indicated in Fig. A9.2.

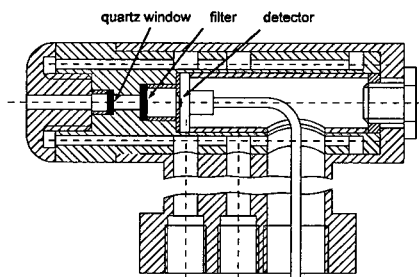


Fig. A9.2: Radiometer probe with dismantlable quartz window and filter

Adding filters and lenses to protect the detector is possible. However, they greatly limit the usable spectral region as seen in Fig. A9.3. The goal, however, of radiometric measurements is to cover the entire radiation which appears.

However, the detectors may not touch the plasma because they can be damaged by the heat. This can be avoided by mounting the detector deep inside the cooled probe body. The radiation reaches the detector through an optical tunnel. Here a cold, stationary gas column forms because the detector completely closes off the end of the tunnel.

However, this method clearly narrows the visible solid angle. In order to get the entire radiation on the front side of the sample, the probe has to be rotated in the beam while being measured so that the complete solid angle is covered. A hemispherical numerical integration results then in the demanded radiation heat flux at the front opening of the radiometer [A9.1].

The detector and where applicable the filters and lenses must be suited to the task. Special attention must be paid to the choice of the detector. After that the most important characteristics are compiled.

The signal-noise ratio and the noise equivalent power (NEP) are used to assess and compare detectors.

The signal-noise ratio is the ratio between the output signal of a detector and the superordinated noise. It describes the maximum possible exactness of a measurement. With a signal-noise ratio of 100:1, the exactness of the measurement can in no case be better than 1 %.

In a radiometric detector the NEP indicates the radiation power which has to reach the detector in order to create a signal-noise ratio of 1. NEP is also the smallest measurable power which reaches the detector. The following applies:

$$NEP = \frac{I_n}{S} \quad (A9.2)$$

Here I_n is the noise voltage or the noise current of the detector and S is the total sensitivity. Because S depends on the relative spectral intensity distribution of the radiation source, when comparing various NEP values it must be taken into account that they were recorded with the same radiation source under the same conditions. Usually a black radiator with a temperature of 500 K is used.

Additional important characteristics are:

Linearity

The linearity is one of the most important specifications of a detector for radiometric measurements. Linearity exists when in a certain range the output signal of a detector is exactly proportional to the incoming radiation or when the sensitivity of the detector does not depend on the incoming power.

Time constant

The time constant τ of a detector reports the time that the detector signal requires to reach 63% of the final value after constant radiated power suddenly appears on the detector.

Total sensitivity of a detector

The total sensitivity of a detector is the ratio between the detector output signal I and the total incoming radiated power Φ in a certain wavelength region. It is a function of the detector, the radiation source and the transmission from windows and filters on the optical axis of the measurement arrangement. A certain detector has a different total sensitivity for each radiation source:

$$S = \frac{I}{\Phi} = \frac{\int_{\lambda_1}^{\lambda_2} \Phi_{e/\lambda}(\lambda) S_{\lambda}(\lambda) \tau(\lambda) d\lambda}{\int_{\lambda_1}^{\lambda_2} \Phi_{e/\lambda}(\lambda) d\lambda} \quad (\text{A9.3})$$

with:

- λ_1, λ_2 = lower or upper boundary wavelength
- S = total sensitivity
- I = detector output signal
- Φ = total incoming radiation
- $\Phi_{e/\lambda}(\lambda)$ = absolute spectral intensity distribution of the radiation source
- $S_{\lambda}(\lambda)$ = spectral sensitivity, known from the calibration
- $\tau(\lambda)$ = transmission from windows and filters

Instead of the absolute spectral intensity distribution $\Phi_{e/\lambda}(\lambda)$ the relative or normalized spectral intensity distribution can be used:

$$\phi(\lambda) = \frac{\Phi_{e/\lambda}(\lambda)}{\Phi_{e/\lambda}(\lambda_0)} \quad (\text{A9.4})$$

λ_0 is here the normalized wavelength.

The radiation heat flux onto a detector surface A can be calculated as:

$$\dot{q}_{\text{Strahlung}} = \frac{I}{AS} \quad (\text{A9.5})$$

If in addition the measurement arrangement is divided by the visible solid angle, one obtains the radiation heat flux in $[\text{W}/(\text{m}^2 \text{sr})]$.

Figure A9.3 shows several profiles of the radiation heat flux perpendicular to the beam axis at various N_2/CH_4 plasma combinations used to simulate the entry of the Huygens probe into Titan's atmosphere.

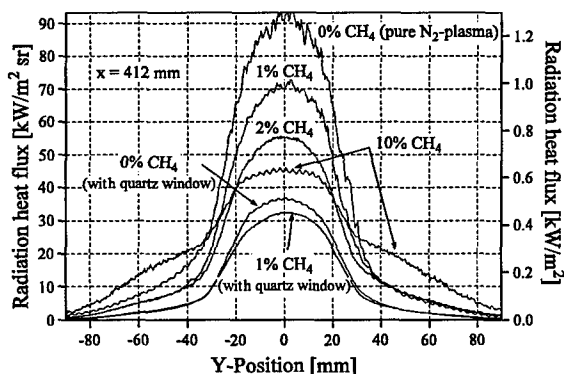


Fig. A9.3: Radial profiles of various N_2/CH_4 -plasmas with and without a protective window at a distance of 412 mm to the plasma generator

References

- [A9.1] Röck, W., "Simulation des Eintritts einer Sonde in die Atmosphäre des Saturnmondes Titan in einem Plasmawindkanal", Dissertation, Universität Stuttgart, 1998.

B Non-Intrusive Measurement Techniques

Most of the optical measurement techniques are non-intrusive techniques. The pyrometer commonly used for surface temperature measurements in plasma wind tunnels, the emission spectrometry and Fabry-Perot interferometry clearly meet this criterion. Emission spectroscopy enables identification of the heavy particles in the plasma and the determination of their temperatures. Furthermore, it has the potential to be used for density measurements. Fabry-Perot interferometry can be used to determine the plasma velocity and the kinetic temperature of the heavy particles.

All measurement techniques which are based on the investigation of the plasma reaction to light intensity radiated into the plasma technically do not belong to the non-intrusive techniques; they may locally change the plasma state and possibly its composition. However, they are generally included in this category. Absorption spectroscopy, laser induced fluorescence and Raman spectroscopy belong to this group. These methods can all be used to identify the particles as well as to determine particle densities and velocities. Another laser based technique is Thompson Scattering from which temperature and density of the free electrons can be derived.

B1 Pyrometry

Determining the surface temperature of heat shield materials is of particular interest for the development as well as for the qualification of these materials. The erosion and ablation behavior are very sensitive to the surface temperature within the regarded temperature range. Temperature measurements during the re-entry itself give information about the material characteristics and the re-entry conditions representing the test conditions which should be used in ground test facilities.

Due to the sufficient thickness of the ablation materials and their low heat conductivity, thermo couples can be mounted at different material depths. The surface temperature, the heat flux and the time-dependent erosion can be determined in this way [B1.1].

The situation is different if fiber ceramic materials are used. Due to the wall thinness (between 0.5 up to only a few millimeters) and the high temperatures (between 1000 and 3000 K) the thermo couples cannot be embedded correctly without a risk of damaging the material. Even during the material production, the temperature rises over the bearable temperature of the thermocouples. If the thermo-

couples are mounted on the back side of the heat shield material, the measurement is adulterated and the material can be damaged by carbonization caused by the thermo couples. Therefore for fiber ceramic materials, a non intrusive measurement technique using a pyrometer remains as single solution.

B1.1 Theoretical Basics

Each body with a surface temperature above absolute zero emits electro-magnetic radiation. Measurement instruments that determine the surface temperature from this thermal radiation are called radiation thermometers or pyrometers. The observed wavelength region reaches from 10^{-7} to 10^{-5} m, which also covers the narrow region of visible light.

The basic quantities are the *radiant energy flux* ϕ given by the emitted energy dW during the time dt

$$\phi = \frac{dW}{dt} \tag{B1.1}$$

and the *radiant exitance* M which describes the radiation that is emitted by the surface element dA into a solid angle of 2π :

$$M = \frac{d\phi}{dA} \tag{B1.2}$$

If the *radiant exitance* is observed at a single wavelength *spectral radiant exitance* M_λ is obtained which can be calculated using *Planck's law*:

$$M_{\lambda S} = \frac{2\pi c^2 h}{\lambda^5 \left(e^{\frac{hc}{\lambda T}} - 1 \right)} \tag{B1.3}$$

h : Planck's constant ($6.6256 \cdot 10^{-34}$ Js)
 c : Speed of light in vacuum ($2.9979 \cdot 10^8$ m/s)

The integration of $M_{\lambda S}$ of a black body over all wavelengths yields, according to the *Stefan Boltzmann law*, the *radiant exitance of a black body* M_S

$$M_S = \int_0^\infty M_{\lambda S} d\lambda = \sigma T^4 \tag{B1.4}$$

σ : Stefan Boltzmann constant ($5.669 \cdot 10^{-8}$ Wm⁻²K⁻⁴)
 The *emissivity* ϵ is the ratio of the *radiant exitance* M of any given radiator and the *radiant exitance of a black body*.

$$\epsilon = \frac{M}{M_S} \tag{B1.5}$$

which depends on the temperature, the material itself and the condition on the surface such as roughness. Accordingly, the *spectral emissivity* $\epsilon(\lambda, T)$ is defined:

$$\epsilon(\lambda, T) = \frac{M(\lambda, T)}{M_S(\lambda, T)} \tag{B1.6}$$

If the emissivity does not depend on T or λ , the emitting surface is called a *gray body*. Although gray bodies do not exist in reality, the assumption of a gray body gives a good approach for most real bodies.

While the integration of the spectral radiation over the total wavelength regime yields the *Stefan*

Boltzmann law the first derivation gives the wavelength λ_{max} , which defines the wavelength where the emitted spectral radiation at a given temperature T reaches its maximum value.

Wien's Law is obtained:

$$\lambda_{max} = \frac{2898}{T} \cdot 10^{-6} \text{ [m]} \tag{B1.7}$$

Figure B1.1 shows the spectral radiant exitance of a black body for different temperatures within the important wavelength region. If a non black body is observed, the spectral radiant exitance has to be reduced according to the spectral emissivity of the surface.

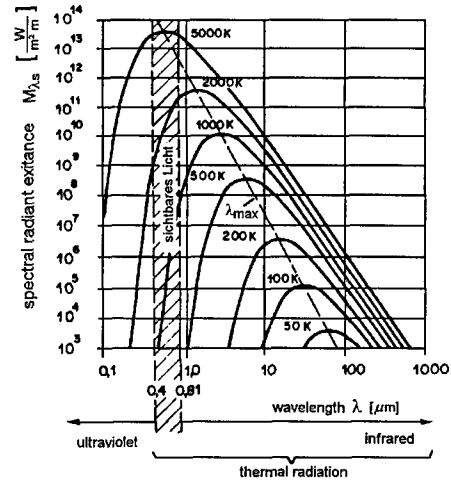


Fig. B1.1: Spectral radiant exitance of a black body

The above mentioned radiation laws already show the main problems of radiation thermometry:

- According to the *Stefan Boltzmann law*, the thermally emitted radiation remarkably decreases (proportional to T^4) with decreasing temperature.
- At low temperatures, the maximum of radiation is shifted to high wavelengths where disturbing influences on the measurement become high.
- The spectral emissivity of non black bodies depends not only on temperature and wavelength but also on the material itself and the surface structure (mainly the surface roughness) in an often not well-known matter.
- Besides the radiation emitted by the observed surface, disturbing radiation of reflected or transmitted radiation emitted by other radiators can influence the measurement.

If radiation interacts with a surface, reflection, absorption and emission occur. The ratios of absorbed, transmitted and reflected radiant energy fluxes to the incoming radiant energy flux are defined as:

absorptance transmittance reflectance

$$\alpha = \frac{\phi_a}{\phi}, \quad \tau = \frac{\phi_{tr}}{\phi}, \quad \rho = \frac{\phi_r}{\phi} \tag{B1.8}$$

According to the above-mentioned definitions, the word spectral is added if these quantities refer to monochromatic radiation.

$$\alpha_\lambda = \frac{\phi_{\lambda,e}}{\phi_\lambda}, \quad \tau_\lambda = \frac{\phi_{\lambda,tr}}{\phi_\lambda}, \quad \rho_\lambda = \frac{\phi_{\lambda,r}}{\phi_\lambda} \quad (\text{B1.9})$$

They are functions of the wavelength and depend on the material, its surface structure and the temperature. They are coupled by the relation

$$\alpha + \tau + \rho = 1 \quad \alpha(\lambda) + \tau(\lambda) + \rho(\lambda) = 1 \quad (\text{B1.10})$$

Additionally, according to *Kirchhoff* the emissivity is equal to the absorptance for all bodies:

$$\varepsilon(T, \lambda) = \alpha(T, \lambda) \quad (\text{B1.11})$$

A black body will absorb all incoming radiation and has therefore an absorptance and due to equation (B1.11) also an emissivity of 1.

B1.2 Measurement Principle

To determine the surface temperature the radiant energy flux emitted by the surface A_1 and received by A_2 has to be determined (see Fig. B1.2). The surface A_1 does not cover the solid angle of 2π , so only a part of the radiant exitance M (or M_λ , respectively) is received. This part is given by:

$$L = \frac{dM}{d\Omega \cos\vartheta} = \frac{d\left(\frac{d\phi}{dA_1}\right)}{d\Omega \cos\vartheta} = \frac{d^2\phi}{dA_1 d\Omega \cos\vartheta} \quad (\text{B1.12})$$

L is the radiance in the dimension $\text{Wm}^{-2}\text{sr}^{-1}$. In Fig. B1.3 A_1 is the radiating surface which emits a radiance of L_1 and A_2 the receiving area which is represented by the measurement array of the pyrometer, which transfers the measured radiance into an electrical signal. According to the radiation laws and due to the geometrical relations given by A_1 , A_2 , a and b , the radiant energy flux $\phi_{1,2}$ in the dimension of Wsr^{-1} is given by:

$$\phi_{1,2} = L_1 A_2 \frac{A_3}{a^2} \quad (\text{B1.13})$$

Normally, area A_3 is given by an iris which is part of the optical path inside the pyrometer. The values A_2 , A_3 and a are hardware parameters of the pyrometer and remain constant within the measurement. Therefore, the measured signal becomes independent of the distance to the measured surface b and is a function of constructive parameters of the pyrometer and of the radiance L_1 emitted by the measured surface. Often a lens system which also acts like an iris is added to the optical setup to measure small areas in large distances to the pyrometer. According to the optical laws, the independence of the measured signal from the distance to the measured object remains valid.

Usually imaging factors between 10 and 100 are used which means that the measured spot on a surface at a distance of 1 m has a diameter of 10 cm or 1 cm.

With *linear pyrometers*, the measured signal is proportional to the radiance seen by the pyrometer and therefore also to that emitted by the measured surface. There are several classes of pyrometers which differ mainly in the evaluation of the measured signals [B1.1].

A *monochromatic radiation thermometer* measures only radiation within a narrow wavelength region (in effect at one wavelength), a *spectral-band radiation thermometer* measures within a much broader wavelength region while a *wideband radiation thermometer* (sometimes also called *total radiation thermometer*) is able to detect more than 90 % of the emitted radiation by choosing suitable optics and detectors.

The *radiation ratio thermometer* compares the spectral distribution of the measured radiation with that of a black body. The best known type is the *two color pyrometer*, which uses the ratio of two spectral radiances measured at different wavelengths to determine the true temperature.

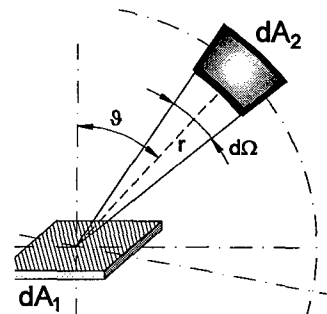


Fig. B1.2: Geometrical relations

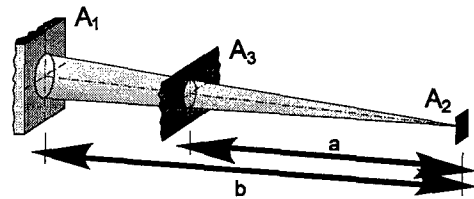


Fig. B1.3: Measurement principle of a pyrometer

To obtain temperature distributions on the surface of a sample, an image can be taken using a CID-camera. The same measurement method was used to determine the temperature distribution on the surface of the cathode of a MPD plasma generator [B1.2]. Similar to normal pyrometric measurements, the radiation emitted by a probe body is detected and evaluated. The main difference is the measurement of a whole array of detector elements which offers, in combination with different lens systems, a wide range of spatial variations.

With the camera, a kind of black and white image is obtained and read into a computer using a video adapter. The typical dynamic resolution of 8 bit offers different gray values from 0 (black) up to 255 (white). The spectral sensitivity of the detector elements limits the usable wavelength range from the visible up to the close infrared where it is possible to limit the radiation with suitable wavelength filters to enable a temperature determination. For this purpose, the camera has to be calibrated by a measurement of a black body radiator at different temperatures. So, different gray-levels can be transferred into temperature values.

B1.3 Determination of the True Temperature

The measured radiant energy flux ϕ_m is a combination of the desired radiation ϕ_e emitted by the surface of the object of interest, of radiation which originates from the surrounding walls ϕ_s and is partly reflected at the surface and partly transmitted by the body as shown in Fig. B1.4.

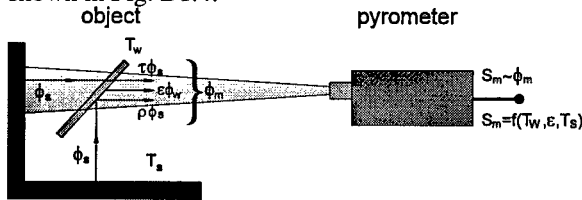


Fig. B1.4: Experimental setup

ϕ_e can be written as the radiation of a black body ϕ_w at the same temperature reduced by the emissivity ϵ of the measured surface. The disturbing radiation of the surroundings ϕ_s is to be multiplied with the factors ρ and τ to obtain the reflected and the transmitted radiation, respectively. For the measured radiant energy flux the equation

$$\phi_m = \epsilon\phi_w + \rho\phi_s + \tau\phi_s \quad (\text{B1.14})$$

is valid. According to equation (B1.10), the sum of emissivity, reflectivity and transmission has to be 1. Thus follows:

$$\phi_m = \epsilon\phi_w + (1-\epsilon)\phi_s \quad (\text{B1.15})$$

According to equations (B1.3), (B1.4) and (B1.12) radiances can be calculated from the radiant energy fluxes and so, between the radiance L_m and the temperature T_m the relation

$$L_m = \int_{\lambda_1}^{\lambda_2} \frac{2\pi c^2 h R(\lambda) d\lambda}{\lambda^5 \left[\exp\left(\frac{hc}{\lambda T_m}\right) - 1 \right]} \quad (\text{B1.16})$$

can be obtained. $R(\lambda)$ is the relative spectral sensitivity of all optical components of the setup and can be regarded as remaining constant between λ_1 and λ_2 .

Substituting the radiant energy fluxes with the radiation densities and assuming black body radiation for the wall emission to allow the usage of Planck's Law, one gets for a *monochromatic radiation thermometer* an equation to determine the true temperature T_w for a measured temperature T_m :

$$T_w = \frac{1}{-\frac{hc}{\lambda} \ln \left[\exp\left(-\frac{hc}{\lambda T_m}\right) - (1-\epsilon) \exp\left(-\frac{hc}{\lambda T_s}\right) \right] + \frac{hc}{\lambda} \ln \epsilon} \quad (\text{B1.17})$$

The same procedure for a called *total radiation thermometer* yields:

$$T_w = \frac{T_m}{\sqrt[4]{\epsilon}} \sqrt[4]{1 - (1-\epsilon) \left(\frac{T_s}{T_m}\right)^4} \quad (\text{B1.18})$$

In reality, the temperature of the surrounding T_s is often clearly below the temperature which should be measured.

In this case, the equations can be simplified to:

$$T_w = \frac{1}{\frac{1}{T_m} + \frac{hc}{\lambda} \ln \epsilon} \quad \text{and} \quad T_w = \frac{T_m}{\sqrt[4]{\epsilon}} \quad (\text{B1.19})$$

Obviously, the agreement between the displayed temperature T_m with the true temperature T_w is better the lower the wavelength used for the measurement and the closer the emissivity is to 1. Generally, the displayed temperature is lower than the true temperature. Furthermore, the influence of the emissivity becomes weaker with a decreasing difference between the temperatures of the measurement object itself and the surroundings.

With a *spectral-band pyrometer* the same equations as with a *monochromatic radiation thermometer* are valid if λ is replaced by a characteristic wavelength at which the main part of the radiation is measured.

One important uncertainty is a result of requiring the emissivity to determine the temperature (see Fig. B1.5). One certain exception is given by the *two color pyrometer*. With this instrument, the ratio of the spectral radiation densities at two different wavelengths λ_1 and λ_2 is determined. The measured signal can be written as:

$$S_m = \frac{L_{m1}}{L_{m2}} = \frac{\epsilon_1 L_{w1} + (1-\epsilon_1) L_{s1}}{\epsilon_2 L_{w2} + (1-\epsilon_2) L_{s2}} \quad (\text{B1.20})$$

Figure B1.5 shows the spectral radiation densities L_{m1} and L_{m2} at the wavelengths λ_1 and λ_2 . Similar to the *total radiation thermometer* T_m is determined from S_m . *two color pyrometers* are used when $T_m \gg T_s$.

Under this assumption, the true temperature can be calculated from:

$$T_w = \frac{1}{\frac{1}{T_m} - \frac{k}{hc} \frac{\lambda_1 - \lambda_2}{\lambda_1 \lambda_2} \ln \frac{\epsilon_1}{\epsilon_2}} \quad (\text{B1.21})$$

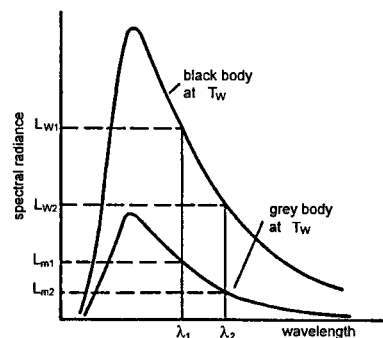


Fig. B1.5: Description of the ratio pyrometry

Under the assumption of a common emissivity at both wavelengths, the above equation can be reduced to $T_w = T_m$, which means that the measured temperature equals the true temperature with no need for any information about the quantitative value of the emissivity.

In reality, this assumption is rarely valid. Especially with metallic surfaces, ϵ decreases with a rising wavelength (see table B1.1). With ceramic materials, the situation is worse because often not even a steady function of the wavelength can be given. The measured temperature is too high and T_m has to be corrected according to equation (B1.22) to obtain T_w . Again, this requires the knowledge of at least the

qualitative course of the emissivity with a rising wavelength.

The possibility that the measured temperature can be higher than the true temperature is significant for *radiation ratio thermometer* because *linear pyrometers* typically show a temperature lower than the true temperature.

B1.4 Emissivity

As shown in the previous section, the temperature measurement with pyrometers can only be correct if the emissivity of the surface is known. ϵ depends on many different factors such as wavelength, temperature and surface structure and has to be determined experimentally. For this purpose, a hole is drilled into a probe body and the true temperature is determined using thermo couples. The emissivity can be determined by a comparison with for example a pyrometrically measured temperature. Table B1.1 shows the emissivity of different metals.

Ceramic materials also show a wavelength dependent emissivity. Exemplarily, the $\epsilon(\lambda)$ -distribution of silicon carbide (SiC) at different temperatures is shown in Fig. B1.6.

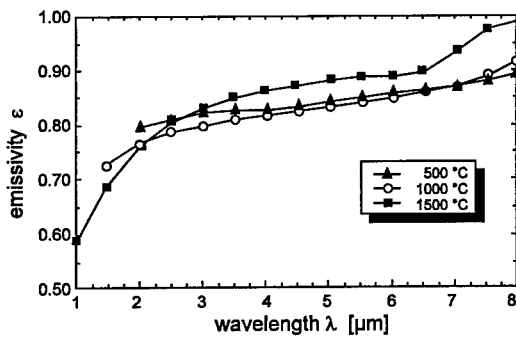


Fig. B1.6: Emissivity of SiC as a function of wavelength and temperature

Uncertainties in determining the emissivity cause errors in the transformation of the measured temperature into the true temperature which can rise up to some hundred K. Figure B1.7 shows the difference ΔT of a temperature T_m determined by a spectral pyrometer and the true temperature T_w for different emissivities at a wavelength of $\lambda = 0.65 \text{ nm}$.

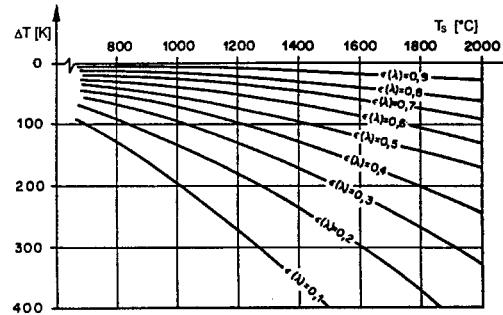


Fig. B1.7: Difference between measured and true temperature for various emissivities

B1.5 Calibration Procedure

For calibration purposes a black body source is available at the IRS. The source which is shown in Fig. B.1.8 consists of an electrically heated graphite radiator with a cylindrical cavity. To approximate the black body, the cavity has a large length-to-diameter ratio and the cavity walls are designed to maintain an isothermal profile. This temperature uniformity is achieved by a variable heat source distribution which is realized by varying the cavity wall thickness. The outline of the graphite rod was therefore calculated using a numerical procedure [B1.3].

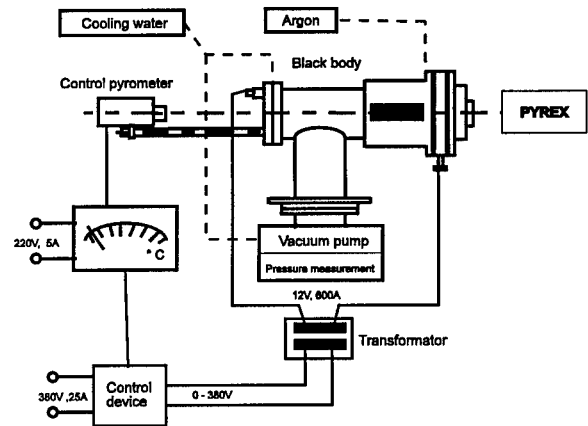


Fig. B1.8: Schematic view of the IRS black body

In order to provide high accuracy, three different geometries for three different temperature ranges are available. The black body's second radiation outlet is used for the calibration of pyrometers. The black body's temperature is varied using the control pyrometer; temperature and photo current are measured simultaneously. Figure B.1.9 shows a typical result of such a calibration measurement for the system (see part C).

metal	temperature [K]	ϵ at $\lambda = 540 \text{ nm}$	ϵ at $\lambda = 660 \text{ nm}$
iron	1300 / 1600 / 2000	-	0.39 / 0.37 / 0.35
gold	1000 / 1300 / 1600	0.41 / 0.44 / 0.40	0.11 / 0.16 / 0.21
copper	1000 / 1300 / 1600	0.40 / 0.40 / 0.38	0.11 / 0.11 / 0.15
molybdenum	1000 / 1500 / 2000	0.44 / 0.42 / 0.41	0.39 / 0.38 / 0.36
nickel	1000 / 1300 / 1600	0.42 / 0.42 / 0.42	0.38 / 0.38 / 0.38
platinum	1000 / 1300 / 1600	0.32 / 0.32 / 0.33	0.29 / 0.30 / 0.30

Table B1.1: Spectral emissivity of different metals

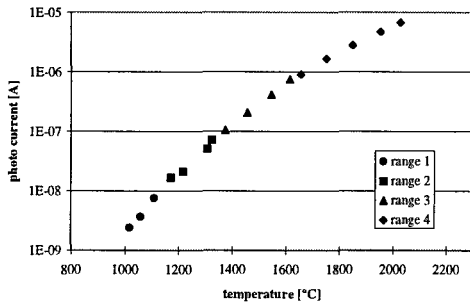


Fig. B1.9: PYREX-LD photo current vs. black body temperature

A photo current line versus the measured temperature is obtained. This photo current calibration curve is then used to calculate the temperature data. Within each of the four measuring ranges, the photo current signal is linear to the temperature with the measured radiance of the material as the only necessary input signal. The advantage of this linearity is that any disturbances as well as changes of the emission coefficient ϵ can be taken into account by reprocessing the temperature data.

B1.6 Pyrometers for Plasma Wind Tunnel Applications

The pyrometers in use at the IRS are listed in Table B1.2. The measurement head TMR85L is used for investigations of cathodes for the plasma devices. All other pyrometers are used in the plasma wind tunnels for material testing. Furthermore, the measurement head TMR95 is used for investigations at comparatively low temperatures between 150 °C and 650 °C. With the TMR105 the pyrometrical determination of surface temperatures of materials with high transmittance in the visible wavelength range such as SiO₂ is possible.

The first five instruments in Table B1.2 show a non-linear characteristic. The main disadvantage can be seen in the difficulty to extract influences of disturbing radiation such as reflected cathode radiation or plasma emission from the measured signal. Generally, it is almost impossible to perform such an extraction if some of the influences show up

after the measurement or if a quantization of these effects is only possible afterwards. Also a wrong emissivity or a change in emissivity during the test can hardly be covered by these instruments.

The results of linear pyrometers as the better choice in this case can also be corrected after the measurement due to the direct proportionality of the measured signal to the spectral radiance. Thus, the linear pyrometer LP2-80/20 [B1.4] as shown in Fig. B.1.10 was optimized for the application to problems within the plasma wind tunnel investigations [B1.5]. One feature is the possibility to use different filter combinations with respect to the plasma radiation.

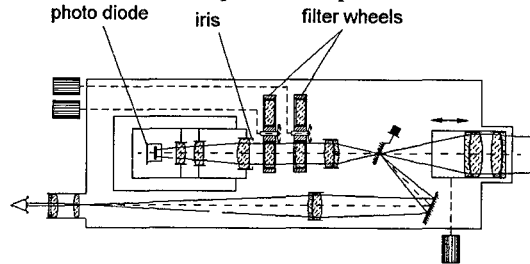


Fig. B1.10: The linear pyrometer LP2-80/20

Based on the good results obtained with the LP2-80/20, a miniaturized linear pyrometer called MP1 was designed and qualified at the IRS [B1.5]. This pyrometer is integrated into the sample support system as shown in Fig. B1.11. On the back of the sample, the temperature measurement is neither influenced by the plasma jet nor by possible changes in emissivity on the front during the test. The PYREX-pyrometer which is described in part C is a flight version of the MP1 [B1.6].

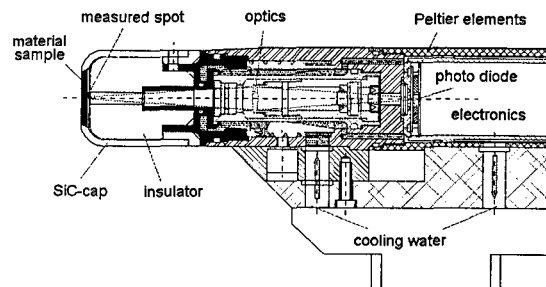


Fig. B1. 11: Miniaturized pyrometer MP1

type	wavelength	measurement range [°C]	purpose
1) spectral band pyrometers			
TMR85EA	900 nm	610 - 3050	cathodes of electrical thrusters
TMR95EA	1.5-2.6 μm	150 - 650	material tests in the PWK electrode investigation with electrical thrusters
TMR105	7 - 7.5 μm	800 - 2000	material tests in the PWK
TMR85H	900 nm	610 - 2420	material tests in the PWK control of black body temperature
2) linear pyrometers			
LP2-80/20	9 diff. wavelengths 560 - 960 nm	800 - 3000	precision measurements
MP1	630 nm	1000 - 1900	material tests in the PWK
PYREX	630 nm	1200 - 3000	material tests in the PWK / reentry experiments
3) CID camera			
CID		1000 - 3400	surface temperature distributions

Table B1.2: Various pyrometers at the IRS

References

- [B1.1] Auweter-Kurtz, M., Burkhardt, J., Fertig, M., Frühauf, H.-H., Habiger, H., Jahn, G., Messerschmid, E., Schöttle, U., "Flugdatenauswertung der MIRKA-Experimente HEATIN und PYREX", DGLR-JT98-203, Bremen, DGLR-Jahrestagung 1998.
- [B1.2] DeWitt, D. P. and Nutter, G. D., "Theory and Practice of Radiation Thermometry", J. Wiley, New York, 1988.
- [B1.3] Winter, M., Auweter-Kurtz, M., Kurtz, H.L. and Sleziona, P.C., "Evaluation of Cathode Temperature Distribution in a Cylindrical MPD Thruster", Proceedings of the 24th International Electric Propulsion Conference, Moscow, Russia, September 1995.
- [B1.4] Groll, M. and Neuer G., "A New Graphite Cavity Radiator as Blackbody for High Temperatures", in: Murray, H.P.(ed.): "Temperature, its Measurement and Control in Science and Industry - Part 1", Vol.4; Instrument Society of America, Pittsburgh, 1971.
- [B1.5] Schreiber, E., Neuer, G., Wörner, B., "Performance Tests with a Standardpyrometer", Proceedings of the Fourth Symposium on Temperature and Thermal Measurement in industry and Science, Helsinki, September 1990, pp. 292-305.
- [B1.6] Loesener, O. R., "Pyrometrische Temperaturmessungen an Oberflächen von Hitzeschutzkeramiken im Plasmawindkanal", Dissertation am Institut für Raumfahrtssysteme, 1993 in: Fortschrittsberichte VDI, Reihe 6: Energieerzeugung, Nr. 294, VDI Verlag, Düsseldorf, 1993.
- [B1.7] Habiger, H., Auweter-Kurtz, M., Früholz, H., Herdrich, G., "PYREX - Pyrometric Temperature Measurement on the Ceramic TPS of the Re-Entry Capsule MIRKA", 3rd European Workshop on Thermal Protection Systems, ESTEC, Noordwijk, The Netherlands, March 1998.

B2 Emission Spectroscopy

Emission spectroscopy is based on the analysis of the radiation which is emitted by the investigated medium and evaluates the spectral distribution of the obtained radiation. Thus, information about the qualitative and quantitative chemical composition and about different thermodynamic quantities can be acquired.

B2.1 Theoretical Basics

In gases and plasmas at low pressures which are excited to emit light, the emission is mainly caused by single atoms and molecules. Thus, the properties of the emitted radiation allow conclusions to be drawn about the emitting particles. In this case, radiation occurs mainly at single discrete wavelengths as so-called spectral lines. The number of lines for molecules of one species normally outnumbers the number of lines caused by a certain atom. The resulting intensity distribution as a function of the wavelength is called emission spectrum.

There are several possibilities to excite atoms and molecules to emit radiation:

- In flames, light arcs and sparks, the atoms are excited by collisions due to their high thermal energy.
- In discharges, the excitation is caused by collisions with electrons and ions which possess high kinetic energy due to acceleration processes within an electric field.
- Excitation induced by radiation at short wavelengths such as UV or Röntgen-radiation.

For the first two reasons, the plasma jet within a plasma wind tunnel is already excited which makes emission spectroscopic methods easily applicable.

B2.1.1 Discrete Energy Levels of Atoms

This section gives an overview of the basic processes for the excitation of atoms. More detailed information is given in [B2.1, B2.2]. The emission and absorption at single lines is explained by the model of *Bohr*, who found that atoms can only exist at discrete energy values which correspond to special orbits of the electrons around the positively charged nucleus (see Fig. B2.1a).

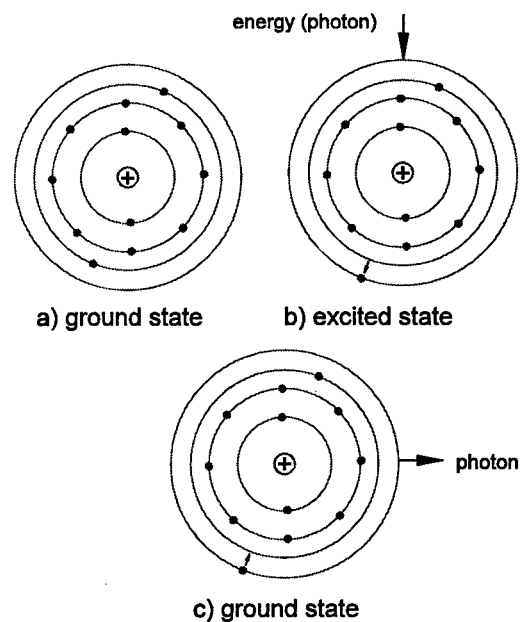


Fig. B2.1: Model of the magnesium atom

Energy can be absorbed or emitted if an electron changes its orbit from one energy level to another one. In this case the energy

$$E_{nm} = h\nu = \frac{hc}{\lambda} \quad (\text{B2.1})$$

is either absorbed or emitted in form of electromagnetic waves of the frequency ν which is equivalent to the wavelength λ . Here, h is *Planck's constant* and c the speed of light in the observed medium. Only transitions between allowed energy values are possible. The allowed energy values are called energy levels and are characterized by the indices n and m in the above equation. This means an atom can only absorb radiation if it passes the transition from the energy level E_m to the higher

energetic level E_n where its electron is at a higher energetic orbit (see Fig. B2.1b). On the other hand, an atom at the state E_n emits radiation if its electron falls down to a lower energetic orbit with the energy E_m (see Fig. B2.1c).

The time during which the electrons stay in the higher energetic state is limited to the life-time of the excited state which is characteristic for each excited state. This time, which is equivalent to the time between absorption and emission, is normally very short, in the range of nanoseconds or below.

An important quantity is the spectral emission coefficient ϵ_v which is defined as the energy of the radiation per time and solid angle emitted at the frequency ν by a unity volume. For a spontaneous transition of an excited electron at an energy level n to a lower level m , the emission coefficient ϵ_{nm} can be calculated as:

$$\epsilon_{nm} = \frac{I}{4\pi} h\nu_{nm} A_{nm} n_n \quad (B2.2)$$

Here, A_{nm} is the *Einstein transition probability* between the excited states m and n while n_n is the number density of the particles in the excited state n .

According to equation (B2.1), the transition from the energy level n to a lower level m produces emission of the frequency ν . In reality, the emission occurs within a frequency interval $\delta\nu$. This phenomenon is called line broadening. Therefore, the emission coefficient ϵ_{nm} of a spectral line with the linewidth $\delta\nu$ has to be written as:

$$\epsilon_{nm} = \int_{\nu}^{\nu+\delta\nu} \epsilon_{\nu} d\nu \quad (B2.3)$$

The different broadening mechanisms are described in section B2.1.2.

The basic mechanisms of atomic radiation can be seen most clearly in the most simple case of the hydrogen atom with only one electron.

B2.1.1.1 The Optical Spectrum of the Hydrogen Atom

Kirchhoff and *Bunsen*, who laid the foundation for spectral analysis, realized already in the middle of the last century that each element emits its own characteristic spectrum. The spectral lines of one species can be sorted into series and are described formally by a so-called series formula. In the most simple case of the hydrogen atom with only one electron, each spectral line fulfills the equation:

$$\frac{1}{\lambda} = R_H \left(\frac{1}{n_1^2} - \frac{1}{n_2^2} \right) \quad (B2.4)$$

Here, R_H is the so-called *Rydberg-constant* ($R_H = 2\pi^2 m_e e^4 / (h^3 c) = 109677,581 \text{ cm}^{-1}$), where the index H stands for hydrogen. n_1 and n_2 are natural numbers and represent the numbering of the energy levels where $n_1 < n_2$ and n_1 is constant within one series.

The emission spectrum of hydrogen consists of the following series:

- Lyman-Series (UV) $n_1 = 1 \quad n_2 \geq 2$
- Balmer-Series (visible if $n_2 < 8$) $n_1 = 2 \quad n_2 \geq 3$
- Paschen-Series (infrared) $n_1 = 3 \quad n_2 \geq 4$
- Brackett-Series $n_1 = 4 \quad n_2 \geq 5$
- Pfund-Series $n_1 = 5 \quad n_2 \geq 6$

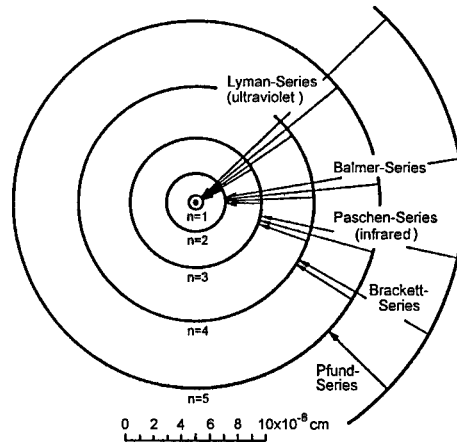


Fig. B2.2: Bohr model of the hydrogen atom with the first five spectral series

Figure B2.2 explains the origin of the different series. Normal hydrogen, where all atoms are at the ground level ($n=1$), can absorb radiation only in the Lyman-series. The absorption at other spectral lines requires the existence of excited states which means that atoms exist where the electron already stays in the levels $n_1 = 2$ or $n_1 = 3$ and so on.

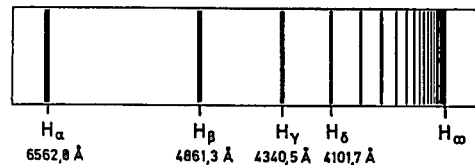


Fig. B2.3: Balmer-series of hydrogen

With rising n_2 the spectral distance between lines of one series decreases more and more. For $n_2 \rightarrow \infty$ the borders of the series are given by:

$$\lambda_{\infty} = \frac{n_1^2}{R_H} \quad (B2.5)$$

Beyond this border, the spectrum is no longer characterized by single emission lines but by continuous emission. The radiation is now no longer caused by transitions of excited atoms. It originates when free electrons are captured by ions (radiation by recombination) or when ions or electrons are accelerated or decelerated by electric fields. The line emission is also called bound-bound radiation while radiation by recombination is called free-bound. Radiation caused by acceleration and deceleration processes is termed free-free.

If the excited states are highly enough populated, the emission spectrum of hydrogen always contains three characteristic lines in the visible wavelength region at 6563, 4861 and 4340 Å ($1\text{Å} = 10^{-10}\text{m} = 0.1\text{nm}$) which

originate from the Balmer-series (compare Fig. B2.3). The strongest of these lines was already discovered by *Ångström* in 1853. Nowadays this line is called H_{α} -line (6563 Å), the others were called H_{β} , H_{γ} and so on corresponding to their rising frequency. For atoms other than hydrogen the formulation of analytic series formulas that cover all possible spectral lines becomes rather complicated due to the fact that more than one electron exists.

B2.1.1.2 The Optical Spectra of Nitrogen and Oxygen

In the case of re-entry investigations, the emissions of nitrogen and oxygen as main components of an air plasma are of particular interest. As mentioned above, the definition of simple analytic series formulas like those for hydrogen is no longer possible. Although a more complicated analytic calculation of single emission lines is still possible, in most cases using values that are tabulated in literature like [B2.3, B2.4] is the better solution. Different numerical codes like NEQAIR [B2.5] or PARADE [B2.6] offer the possibility of computing a complete spectrum. Normally, the number densities of the desired species as well as different temperatures have to be added into the code. The working principle of the code will not be discussed in more detail but Figs. B2.4 and B2.5 show the emission of atomic nitrogen and oxygen and their ions computed with PARADE.

species	number density [m ⁻³]
N	6,4 10 ²⁰
O	2,02 10 ²⁰
N ⁺	1,72 10 ²¹
O ⁺	3,16 10 ²⁰

Table B2.1: Number densities used for PARADE computation

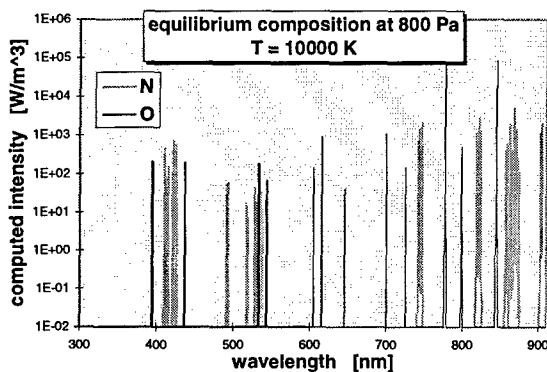


Fig. B2.4: Emission of neutral atomic nitrogen and oxygen computed by PARADE

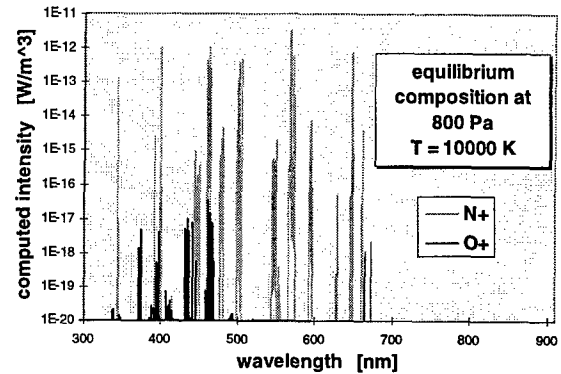


Fig. B2.5: Emission of ionized atomic nitrogen and oxygen computed by PARADE

Table B2.1 gives the number densities used for the computation. Although the number densities of the ions are even higher than those of the neutral particles, the computed intensities within the same wavelength region are weaker by factors of about 10^{20} and 10^{15} . This factor shows the influence of the Einstein transition probability.

B2.1.2 Line Broadening

The *natural line-width* in an almost motionless plasma at a low pressure (which means that collisions between particles are rare) is determined by *Heisenberg's law of uncertainty* and is in the dimension of 10^{-5} nm which normally can be neglected in comparison to the other broadening mechanisms.

The most important processes for line-broadening are:

- Doppler effect
- Interaction with other particles (pressure broadening such as resonance, Stark and Van der Waals broadening)
- Zeemann effect caused by disturbing magnetic fields
- Absorption within the plasma
- Contributions of the optical elements

The Zeemann effect gains importance if strong magnetic fields are used e.g. to control the plasma as in fusion reactors. The influence of absorption can be seen if the intensity profile has a local minimum value at the center of the line where the emission is re-absorbed. This effect gains importance at high pressures and at optically thick plasma states. The contributions of the optical elements are mainly caused by chromatic and spherical aberrations of lenses and mirrors. This effect has to be taken into account in the calibration procedure.

The first two effects can be used for diagnostics to determine thermodynamic quantities. Therefore, the Doppler broadening and the pressure broadening (here Stark broadening is the most important process) are discussed in more detail in this section.

B2.1.2.1 Doppler Broadening

The motion of radiating particles causes a wavelength shifting of the emitted spectral line (Doppler shift). Within a non-flowing plasma, the velocity values and directions of the single particles are statistically distributed. A superposition of the different Doppler shiftings yields a broadened intensity profile. If the Doppler displacement is strong in comparison to the other broadening mechanisms, the translatory temperature of the emitting particles can be determined from the Doppler half width of the emission lines. For this purpose, a high resolution spectrometer is needed. A Fabry Perot interferometer fulfills this requirement (see section B4).

B2.1.2.2 Broadening by Interaction with Other Particles

Neutral particles, electrons and ions in the plasma surrounding the emitting particles can cause disturbances of the emission which is proportional to the partial pressures of the emitting and disturbing particles. This pressure broadening can be divided into resonance, Stark and Van der Waals broadening. To describe this procedure, the disturbing particles are mostly regarded as classical particles which move in the most simple case on straight lines with the velocity v . From a distance ρ to the emitting particle the effect of the disturbing particle can be noticed as illustrated in Fig. B2.6. Therefore, the time during which the disturbance occurs is in the magnitude of

$$\Delta t \approx \frac{\rho}{v} \tag{B2.6}$$

If Δt is short in comparison to the time between two disturbances (which is normally valid for fast particles such as electrons) the disturbances can be regarded as collisions and interpreted by collision theories. In this case, the emitting particle is regarded as a harmonic oscillator.

If a disturbing particle passes the emitting particle, the phase of the above-mentioned oscillation is changed. A Fourier analysis of the phase-disturbed oscillation gives a dispersion profile with the half width Δv_H (see Fig. B2.7). The maximum value of this line profile is shifted by Δv compared with the profile of the undisturbed line with the frequency ν_0 . At the regarded plasma states, the half-width is mainly determined by the Stark effect which covers the interaction of charged particles caused by the forces due to their electric field.

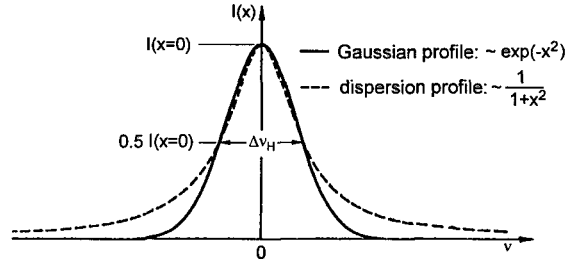
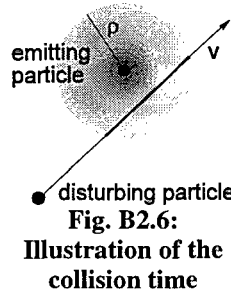


Fig. B2.7: Gaussian and dispersion profile with the same half width

In comparison to the emission without disturbing effects caused by an electric field, the emission of atoms in an electric field of the strength E is shifted by the frequency Δv :

$$\Delta v(E) = \frac{1}{2\pi} C^* E^2 \tag{B2.7}$$

Here, C^* is the so-called Stark effect constant. A disturbing electron in the distance r to the emitting particle produces an electric field at the location of the particle with the strength

$$E = \frac{1}{4\pi\epsilon_0} \frac{e}{r^2} \tag{B2.8}$$

and therefore causes a frequency displacement of the above described oscillator of:

$$\Delta v(r) = \frac{1}{2\pi} \left(\frac{e}{4\pi\epsilon_0} \right)^2 C^* \frac{1}{r^4} = \frac{C_w}{r^4} \tag{B2.9}$$

Therefore, the line broadening due to the Stark effect is proportional to $-r^{-4}$ with the constant C_w . So, the equations for the line displacement Δv_v^{ST} and the half width Δv_H^{ST} in a plasma with the electron density n_e and the average thermal velocity \bar{v} can be written as:

$$\begin{aligned} \Delta v_v^{St} &= \frac{1}{2\pi} 9.85 C_w^{2/3} \bar{v}^{1/3} n_e \\ \Delta v_H^{St} &= \frac{1}{2\pi} 11.37 C_w^{2/3} \bar{v}^{1/3} n_e \end{aligned} \tag{B2.10}$$

$$\text{with } v = \sqrt{\frac{8}{\pi} kT \left(\frac{1}{m_e} + \frac{1}{M} \right)}$$

Here, M is the molecular mass of the corresponding ion. In the above equations, only the influence of the electrons on the emitting particles is taken into account. Due to their higher mass and their therefore lower velocity, the influence of the heavy particles can often be neglected. Meanwhile, the simple model as described above has been refined by quantum mechanical considerations of the collision processes but the principal results remain valid.

Due to their large line width, especially the Balmer lines of the hydrogen atom are well-suited to determine the electron density from the line broadening due to the Stark effect. Figure B2.8 shows the H_α -line at two different plasma states.

The line width of the Balmer line H_β is even stronger than that of the H_β -line. At an electron density of

$n_e = 10^{23} \text{ m}^{-3}$ and a temperature of $T = 10000 \text{ K}$ the half width of the H_β -line is 45 \AA .

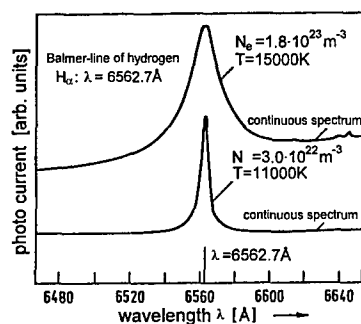


Fig. B2.8: Line broadening due to the Stark-effect

For plasmas without hydrogen, determining the electron density from the Stark broadening is often difficult or even impossible because the effects of other broadening mechanisms (especially the effect of Doppler broadening) are stronger than the Stark effect. Sometimes, small amounts of hydrogen can be added to the plasma to enable the determination of the electron density as described above.

B2.1.3 Energy Levels of the Molecules

In this section, an overview of the basic principles will be given. For more detailed information the corresponding literature such as [B2.7, B2.8] is recommended. As seen above, the energy levels of atoms are defined by the electron orbits around the nucleus. In the case of molecules, there are additional energy levels caused by the degrees of freedom of rotation and vibration. Still, the emission occurs at discrete energies which results in an emission spectrum consisting of single emission lines. But in comparison to the atoms, the number of transitions allowed is much higher and the spectral distance between the single lines is much smaller. A measurement of single lines is only possible with extremely high resolution spectrometers. The wavelength of each emission line is not only a function of the upper and lower electronic states of the transition but also of the upper and lower rotational and vibrational energy levels. In molecular spectroscopy usually the wave number $\tilde{\nu}$ which is the inverse wavelength is used to characterize the single emission lines. The corresponding wave number for a molecular transition is proportional to the total change in energy:

$$\tilde{\nu} = \frac{1}{hc} (\Delta E_{el} + \Delta E_{vib} + \Delta E_{rot}) \quad (\text{B2.11})$$

Here, ΔE_{el} , ΔE_{rot} and ΔE_{vib} , are the changes in electronic, rotational and vibrational energy, respectively.

The effect of the electronic transition can be reduced to the corresponding energy difference of the upper and lower electronic state and is usually taken from literature such as [B2.8, B2.9]. The degrees of freedom for rotation and vibration can be described

by analytical models which allow the calculation of the possible energy levels and the quantum physical interpretation of the obtained spectra.

B2.1.3.1 Rotational Energy Levels

Figure B2.9 shows a simple model for a two-atomic molecule which is simulated as a dumb-bell. Here, the atoms are regarded as point masses m_1 and m_2 , the connection with the length r_0 is regarded as boundless and rigid in a first approach. The molecule rotates around the center of mass S . In this system, the rotational energy can be calculated using the equations of classical mechanics:

$$E_{rot} = \frac{1}{2} j \omega^2 \quad (\text{B2.12})$$

Here, j is the moment of inertia and ω the angular velocity of the rotation. For the simple model of the rigid rotation, j becomes:

$$j = m_1 r_1^2 + m_2 r_2^2 \quad (\text{B2.13})$$

The assumption that $m_1 = m_2 = m$ and therefore $r_1 = r_2$ which is actually valid for homonuclear molecules results in:

$$j = \frac{m}{2} r_0^2 \quad (\text{B2.14})$$

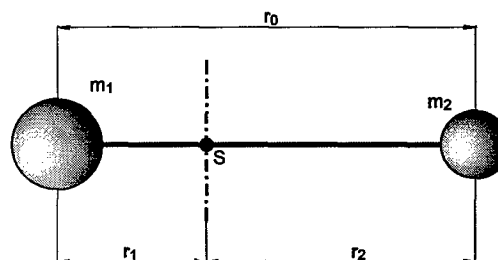


Fig. B2.9: Molecule as rotating dumb-bell

Equations of classical mechanics would say that the rotational energy can have any value. But again, in quantum mechanics only discrete energy levels exist. As not explicitly shown here, the solution to the so-called *Schrödinger equation* yields the relation:

$$E_{rot} = \frac{h^2}{8\pi^2 j} J(J+1) \quad (\text{B2.15})$$

with $J = 0, 1, 2, \dots$

As already mentioned, h is *Planck's constant* while J is the *rotational quantum number*.

In molecular spectroscopy, the energy terms are usually given in terms of wave numbers which is done by a normalization by hc . Therefore, equation (B2.15) is equivalent to:

$$F(J) = \frac{E_{rot}}{hc} = B_e J(J+1) \quad (\text{B2.16})$$

The rotational constant B_e is one of the most important constants in molecular spectroscopy. It is inversely proportional to the moment of inertia j and gives for a known atomic mass the bonding length of the molecule which is a very basic piece of

information about the inner construction of the investigated molecule. The normalized rotational energy $F(J)$ is used within the temperature determination procedure of molecular temperatures (compare section B2.2.4).

The selection rules of quantum mechanics only allow transitions with neighboring rotational quantum numbers which means the maximum change in J can be 1 or -1. The resulting series of emission lines are called branches and are named P-, Q- and R-branch. The possible changes in rotational energy become:

$$\text{P-branch } (\Delta J=1) \quad \Delta E_{rot} = \frac{h^2}{8\pi^2 J} 2(J+1) \quad (\text{B2.17a})$$

$$\text{Q-branch } (\Delta J=0) \quad \Delta E_{rot} = 0 \quad (\text{B2.17b})$$

$$\text{R-branch } (\Delta J=-1) \quad \Delta E_{rot} = -\frac{h^2}{8\pi^2 J} 2J \quad (\text{B2.17c})$$

If the change in the total angle remains constant within the transition, the Q-branch is not allowed. The contribution of the rotational transition to the wave number of the emission line is given by:

$$\tilde{\nu}_{rot} = \Delta F(J) = \frac{\Delta E_{rot}}{hc} \quad J = 0, 1, 2, \dots \quad (\text{B2.18})$$

In the model of the rigid rotating dumb-bell, the wave numbers within one branch increase linearly with a rising quantum number. This results in constant spectral differences between the single rotational lines in terms of wave numbers. In reality, the connection between the two nuclei is not rigid as assumed within the above equations. This yields a deformation of the molecule with rising centrifugal force which can be taken into consideration by implementing a second order correction term yielding the model of a non-rigid rotating dumb-bell. Here, the constant D_e is implemented which considers the extension of the distance between the nuclei with increasing rotational energy. D_e is an experimentally determined constant which varies for different species and for different electronic states. Equation (B2.16) transforms into:

$$F(J) = B_e J(J+1) - D_e [J(J+1)]^2 \quad (\text{B2.19})$$

B2.1.3.2 Vibrational Energy Levels

In addition to the rotation around the center of mass, a vibration of both atoms along the molecular axis is possible. In the most simple way, this vibration can be described as the motion of a reduced mass μ around an equilibrium position r_0 with $\Delta r = r - r_0$. With

$$\mu = \frac{m_1 m_2}{m_1 + m_2} \quad (\text{B2.20})$$

and the spring constant k the well-known differential equation of the harmonic oscillator is obtained:

$$\mu \frac{d^2(\Delta r)}{dt^2} + k\Delta r = 0 \quad (\text{B2.21})$$

The solution to this equation is an oscillation with the frequency:

$$\nu_{osc} = \frac{1}{2\pi} \sqrt{\frac{k}{\mu}} \quad (\text{B2.22})$$

Similar to the model of the rotating dumb-bell, the application of the Schrödinger equation on the harmonic oscillator yields again quantized vibrational energies. The vibrational energy term becomes:

$$E_{vib}(\nu) = h\nu_{osc} \left(\nu + \frac{1}{2}\right) \quad (\text{B2.23})$$

with $\nu=0, 1, 2, \dots$

Again, a normalization by hc can be done yielding:

$$G(\nu) = \frac{E_{vib}(\nu)}{hc} = \omega \left(\nu + \frac{1}{2}\right) \quad (\text{B2.24})$$

The energy scheme of a linear harmonic oscillator consists of equi-distant steps $h\nu_{osc}$ with a minimum energy value $h\nu_{osc}/2$. ν is the vibrational quantum number and ω represents the vibrational frequency. In contradiction to the rotation, transitions between vibrational energy levels with quantum number differences higher than 1 are also allowed. The wave numbers of pure vibrational lines (which means that both upper and lower level belong to the same electronic state and that no change in rotational energy occurs which is equivalent to $\Delta J = 0$) are given by:

$$\tilde{\nu} = \frac{\Delta E_{vib}}{hc} = \frac{\nu_1 - \nu_2}{c} \nu_{osc} \quad (\text{B2.25})$$

From this equation, the distances between the single lines are supposed to be multiples of the ground frequency divided by c . Again, this expectation is not fulfilled completely in reality which can be explained by the fact that a molecule has to be seen as a so-called *anharmonic oscillator*.

To illustrate this coherence, the potential curves for both harmonic and anharmonic oscillators are plotted in Fig. B2.10. They show the potential of the forces between the nuclei as a function of the nuclear distance. The quantized vibrational energy levels E_{vib} are added to the viewgraph.

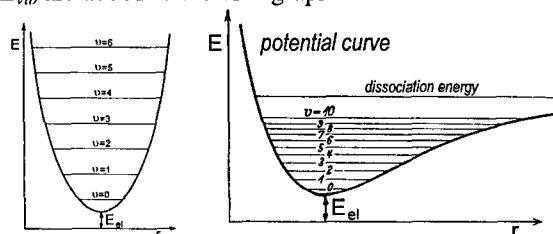


Fig. B2.10: Harmonic (left) and anharmonic (right) oscillator

In the case of a harmonic oscillator, the potential curve appears as a symmetrical parabolic function. If one nucleus is regarded as fixed, the other one would oscillate like a ball which rolls along the curve. The points where the energy levels cross the curve are the reversal points of this oscillation.

This model does not agree with reality in two essential points. First, in the simple model there is no theoretical reason that the distance between the nuclei

could not decrease to zero. In reality, this is physically not possible because the electrostatic forces between the two positively charged nuclei would rise very quickly. On the other hand, the potential is not allowed to rise until infinity with increasing distance between the nuclei. The force between the nuclei which is produced by the electrons is only decreasing with rising distance until the molecule becomes dissociated. As can be seen from the potential curves, reality is better represented by the model of the anharmonic oscillator. In this case, the energy levels are no longer equidistant.

B2.1.4 The Molecular Spectrum

As already mentioned, the molecular emission spectra are based on a superposition of electronic, vibrational and rotational transitions. The wave number of each emission line is given by the total change in energy. From now on, the upper state of a transition is characterized by ν' and the lower state by ν'' . Using this nomenclature, equation (B2.11) can be written as:

$$\tilde{\nu} = \Delta T^{el} + \Delta G + \Delta F \quad (\text{B2.26})$$

or

$$\tilde{\nu} = T'^{el} - T''^{el} + G'(\nu') - G''(\nu'') + F'(\nu', J') - F''(\nu'', J'') \quad (\text{B2.26b})$$

with: T^{el} normalized electronic energy
 $G(\nu)$ normalized vibrational energy
 $F(\nu, J)$ normalized vibrational energy
 and $\Delta T^{el} \gg \Delta G \gg \Delta F$

Within each electronic state, the electronic, rotational and vibrational constants are different and the basic mechanisms described in sections B2.1.3.1 and B2.1.3.2 are coupled. If only the rotational energy changes ($\Delta T^{el} = \Delta G = 0$), the pure rotational spectrum in the far ultrared is obtained with:

$$\tilde{\nu} = +F'(J') - F''(J'') \quad (\text{B2.27})$$

If the vibrational energy changes but the electron energy remains unchanged, the rotational vibrational bands in the short ultrared are obtained.

$$\tilde{\nu} = G'(\nu') - G''(\nu'') + F'(\nu', J') - F''(\nu'', J'') \quad (\text{B2.28})$$

In section B2.1.1.2 the rotational constant B_e was introduced for the model of a rotating dumb-bell. In the case of coupling between vibrational and rotational transitions, the model has to be extended to a rotating oscillator where B is also a function of the vibrational quantum number. Additionally, the bonding length of the molecules differs at different electronic levels. So B_e has to be replaced by $B'_{\nu'}$ and $B''_{\nu''}$ for the upper and lower states of the transition. If the energy terms in equation (B2.26b) which are not a function of the rotational quantum numbers such as the normalized electronic and vibrational energies are combined to a wave number $\tilde{\nu}_0$, the wave numbers of the emission lines for a given electronic and vibrational transition within the

different branches can be written as a function of the rotational quantum number:

P-branch ($\Delta J=1 \Rightarrow J'=J, J''=J+1$):

$$\tilde{\nu}_p = \tilde{\nu}_0 + (B'_{\nu'} - B''_{\nu''})J^2 + (B'_{\nu'} - 3B''_{\nu''})j - 2B''_{\nu''} \quad (\text{B2.29a})$$

Q-branch ($\Delta J=0 \Rightarrow J'=J''=J$):

$$\tilde{\nu}_q = \tilde{\nu}_0 + (B'_{\nu'} - B''_{\nu''})J^2 + (B'_{\nu'} - B''_{\nu''})J \quad (\text{B2.29b})$$

R-branch ($\Delta J=-1 \Rightarrow J'=J+1, J''=J$):

$$\tilde{\nu}_r = \tilde{\nu}_0 + (B'_{\nu'} - B''_{\nu''})J^2 + (3B'_{\nu'} - B''_{\nu''})j + 2B'_{\nu'} \quad (\text{B2.29c})$$

These parabolic functions of the rotational quantum number give the spectral position of all rotational emission lines for one vibrational transition within a given electronic transition. If the rotational quantum numbers are plotted versus the wave number, the resulting graphs are called Fortrat parabolas.

Similar to the wave number, the intensity of an emission line is represented by a superposition of an electronic, a vibrational and a rotational transition. Under the assumption of a Boltzmann distribution (compare section B2.2.1) the intensity of each emission line is given by:

$$I_{\nu'J'-\nu''J''} = K \nu^4 S_J f_{alt} e^{\left[-T'^{el} \frac{hc}{kT_e} \right]} e^{\left[-G'(\nu') \frac{hc}{kT_{vib}} \right]} e^{\left[-F'(\nu'J') \frac{hc}{kT_{rot}} \right]} \quad (\text{B2.30})$$

Here K is a function of the electronic transition moment and the partition functions for the electronic, vibrational and rotational transition and therefore of electronic, vibrational and rotational temperature but not of rotational or vibrational quantum number. For a given plasma state, K is a constant.

S_J is the London-Hönl factor which describes the statistical weights for the transition. In the case of N_2^+ as a homonuclear diatomic molecule the London-Hönl factors for P- and R-branch of the First Negative band system become:

$$\text{P-branch: } S_J^p = \frac{(J'+1)^2 - \frac{1}{4}}{(J'+1)} \quad (\text{B2.31})$$

$$\text{R-branch: } S_J^r = \frac{J^2 - \frac{1}{4}}{J} \quad (\text{B2.32})$$

Due to effects of the atomic spin, an alternation between adjacent lines within the rotational spectrum occurs which is covered by the factor f_{alt} . In the case of N_2^+ the total spin is 2 and f_{alt} becomes:

$$f_{alt} = \left(\frac{3 + (-1)^{J'+1}}{2} \right) \quad (\text{B2.33})$$

To illustrate the appearance of a molecular spectrum, Fig. B2.11 shows the N_2^+ First Negative band system in low resolution with the different band heads and the fine structure of the $\Delta v=0$ band in high resolution including the 0-0 and the 1-1 band head.

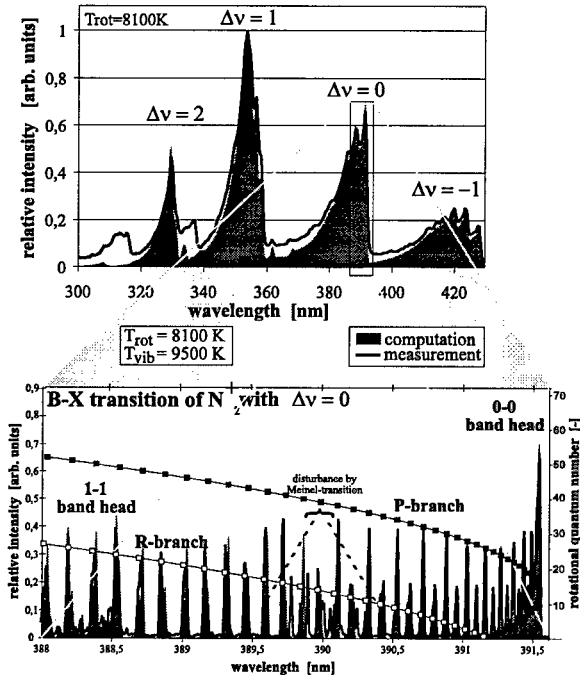


Fig. B2.11: Band structure of the N_2^+ -molecule

The dark line represents a measurement, the gray areas are a numerical simulation of the emission. The Fortrat parabolas for the 0-0 vibrational transition are added to the fine structure diagram. The molecular band is divided into different parts which are formed by single rotational lines. In the case of N_2^+ these bands are degraded to the violet which means that rotational lines with rising rotational quantum number are shifted to lower wavelengths. All rotational lines which result from the transition from the vibrational level 0 to the vibrational level 0 lie close together and form the 0-0 vibrational band. The next band head at lower wavelengths belongs to the 1-1 transition. All higher vibrational transitions with $\Delta v=0$ are adjacent. Together they form the $\Delta v=0$ band system. Systems with other differences in vibrational quantum number such as $\Delta v=-2$, $\Delta v=-1$, $\Delta v=1$ and $\Delta v=2$ are similarly formed.

B2.1.5 Spectral Appearance of an Air Plasma

The basic principles that determine the emission of atoms and molecules have been explained above. The spectrum emitted by a plasma can be regarded as a superposition of the emission of the different radiating species. Figure B2.12 shows a computation of the most important radiating species within an air plasma in the wavelength region between 200 nm and 900 nm in a low resolution of 0.5 nm. The spectral emission as a function of the wavelength corresponds to that of an equilibrium plasma state at a temperature of $T=11700K$ but the emissions of the different species have been scaled by different constant factors to enable a graphical representation in a common diagram. The emissions of the atomic species have been reduced by a factor of 10^{-6} and the emissions of the molecular species NO, N_2 and O_2 have been amplified by factors of 10, 100 and 300, respectively. Generally, the UV-region between 200 nm and 400 nm contains the radiation of most molecular species such as NO, N_2 , O_2 and N_2^+ with the exception of the N_2 First Positive system. The strongest atomic radiation can be observed close to the infrared wavelength region above 700 nm. It can be clearly seen that several wavelength regions are dominated by the emission of different species. The investigation of the molecular species mostly requires a separation of the desired species. For this purpose, best suited wavelength regions can be found for the detection of the different species such as the region below 250 nm which is dominated by the emission of NO, a region between 280 and 305 nm for the investigation of the N_2 Second Positive system and the region between 320 and 450 nm for the N_2^+ First Negative system although a separation of the N_2^+ and the N_2 emission is often not easy. In most cases, the emission of O_2 is too weak to remarkably disturb the measurements of the other species. The investigation of the atomic radiation as well as the measurement of the N_2 Second Positive emission has to be done in a wavelength range from the visible up to the close infrared.

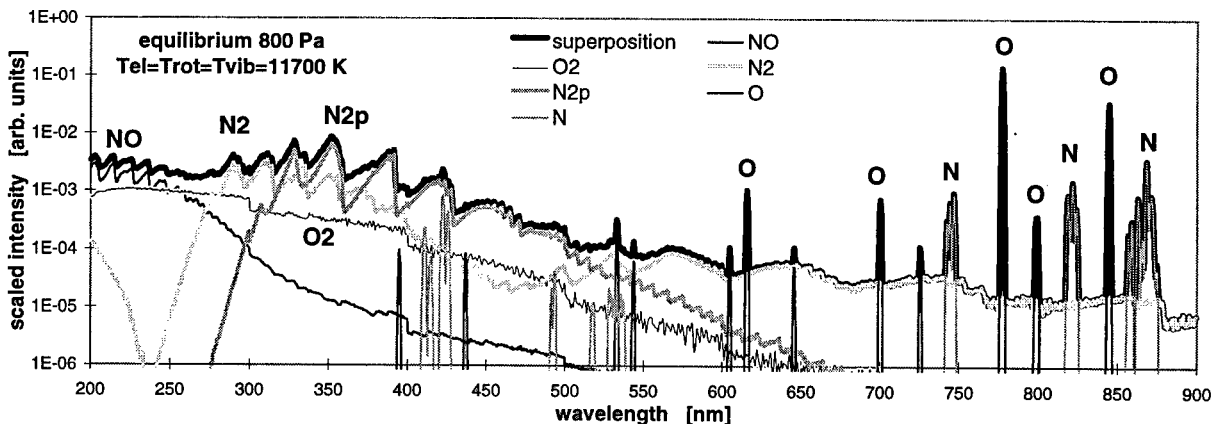


Fig. B2.12: Superposition of the computed emission of the most important radiating species in an air plasma in the wavelength region between 200 nm and 900 nm

The shape of the spectra contains information about the thermodynamic properties of the plasma. Temperatures can be obtained from the ratio of different emission lines; the particle density can be determined from the total intensities. The methods for determining these quantities are described in section B2.2.

B2.2 Plasmadiagnostics

Emission spectroscopy is one of the most important methods of plasma diagnostic measurements with the great advantage of being completely nonintrusive. The emission spectrum contains information about

- the wavelength of the emitted radiation
- its intensity
- the intensity profile of each line
- the intensity distribution of the continuous radiation

To obtain information about thermo-chemical processes, the evaluation of the measured data can become rather difficult. Generally, the applications of emission spectroscopic measurements can be divided into three sections:

- The identification of different atoms and molecules within the plasma
- The determination of thermodynamic quantities such as temperatures and particle densities
- Gaining information about excitation and recombination processes within the plasma

For the applicability of emission spectroscopy as a plasma diagnostic method to determine thermodynamic quantities, the energetic conditions within the plasma are of special interest.

Therefore, this section first gives an overview about the basic assumptions for the different plasma states before the temperature determination from atomic radiation is explained. After that, the determination of T_{rot} and T_{vib} from molecular emission is shown and the determination of particle densities from the emission spectrum is discussed briefly.

B2.2.1 Basic Definitions of the Plasma States

In the state of *complete thermodynamic equilibrium*, each elementary process (e.g. ionization) is in equilibrium with its complementary (in this case recombination) which means the numbers of both processes per unit time are equal. The most important properties of plasma in complete thermodynamic equilibrium are:

- 1) The spectral distribution of the emitted radiation is that of a black body radiator and follows Planck's Law.
- 2) The velocities of all particles follow *Maxwell's distribution function* with a common temperature T

$$f(v) = \frac{1}{N} \frac{dN}{dv} = \frac{4}{\sqrt{\pi}} v^2 \left(\frac{m}{2kT} \right)^{\frac{3}{2}} \exp\left(-\frac{mv^2}{2kT}\right) \quad (\text{B2.34})$$

v is the velocity value, m the particle mass and N the number of particles per volume unit.

- 3) The ratio of the number of particles in an excited state $n_{i,n}$ and the number of all particles of the regarded species n_i is given by a *Boltzmann-distribution*. For this case, the Boltzmann equation

$$\frac{n_{i,n}}{n_i} = \frac{g_{i,n}}{g_{i,0}} \exp\left(-\frac{E_{i,n}}{kT}\right) \quad (\text{B2.35})$$

is valid. The quantities $g_{i,n}$ and $g_{i,0}$ are the statistic weights of the different excitation levels of the regarded ionization stage. They are always integers and can be derived from quantum mechanical laws or taken from spectroscopic tables. $E_{i,n}$ is the energy of the excited state n .

- 4) The chemical equilibrium which is also a part of the complete thermodynamic equilibrium is defined by the *law of mass action*. A reaction $A + B \rightleftharpoons C$ is described by:

$$\frac{n_A n_B}{n_C} = K(T) \quad (\text{B2.36})$$

Here, n_A , n_B and n_C are the concentrations of the reacting components and K is the velocity constant of the particular reaction. K is a function of the temperature and has to be determined experimentally.

- 5) The last important requirement is a relation for the ionization-recombination equilibrium which is given by the *Saha-Eggert equation* which is in fact the law of mass action for the ionization reaction. Limiting the possible ionization stages to 1 yields for the degree of ionization α for an atomic gas:

$$\frac{\alpha^2}{1-\alpha^2} = \frac{(2\pi m)^{\frac{3}{2}}}{ph^3} (kT)^{\frac{5}{2}} e^{-\frac{E_i}{kT}} \quad (\text{B2.37})$$

Here, E_i means the energy of ionization and p is the pressure of the plasma.

In a real plasma there are always differences from complete thermodynamic equilibrium. If those differences are moderate and limited to single processes, the plasma state can often be described as close to equilibrium.

There are several possibilities to gain access to those plasma states but the most important one is probably the LTG-model (*local thermal equilibrium*). In this case, all properties of the complete thermodynamic equilibrium, with the exception of the requirement of a Planck distribution for the radiation, remain valid.

If we regard the energy equations, the influence of this difference on the particle densities can be neglected if the important processes such as excitation and heat transfer processes are dominated

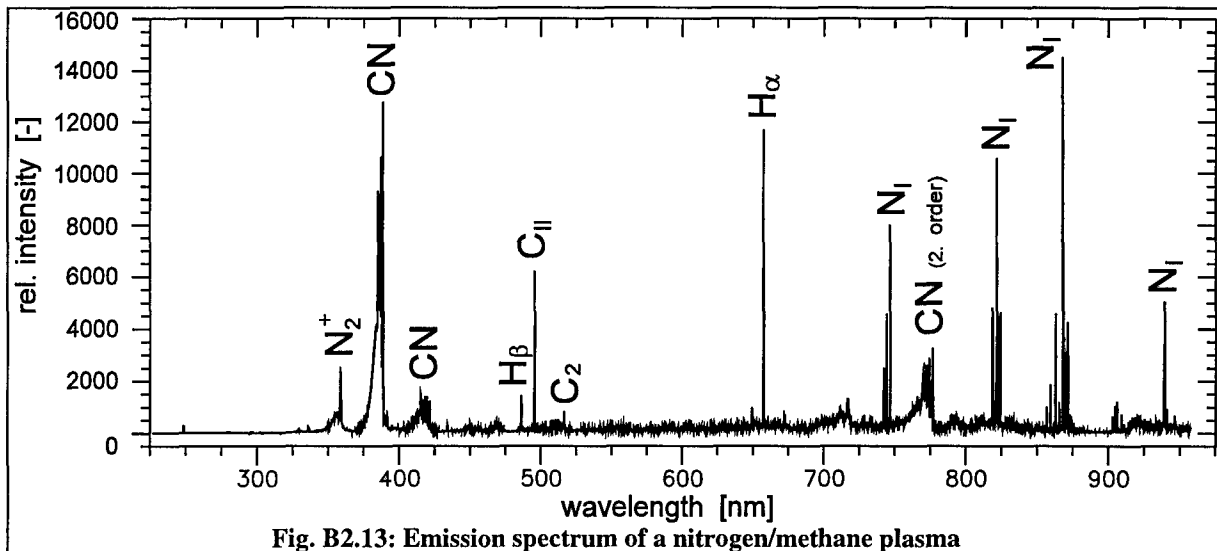


Fig. B2.13: Emission spectrum of a nitrogen/methane plasma

by collisions and not by radiation. For this reason a sufficient particle density of colliding particles is necessary. Due to their higher mobility in comparison to that of the heavy particles, electron number density is the important quantity. The electron number density required for LTG depends on the temperature and the excitation state up to which the LTG should be valid. Additionally, the highest ionization stage that is regarded is important. For example, a typical minimum electron density for LTG for argon up to complete single ionization and at a temperature of $T = 20000\text{K}$ is given by $n_e = 4 \cdot 10^{17}\text{cm}^{-3}$.

Regarding plasma states within plasma wind tunnel experiments, not even LTG can be expected in every region of the jet and the plasma is in thermal and thermodynamic non-equilibrium. Here, thermal non-equilibrium means that the temperatures of the electrons and the heavy particles are different and that the molecules have different values for rotational, vibrational and electronic temperatures. Even in these non-equilibrium cases, the Boltzmann distribution for the rotational and vibrational energy is often still valid with the corresponding temperature T_{rot} or T_{vib} as the determining parameter for the distribution function. In thermodynamic non-equilibrium, the chemical composition of the plasma does not correspond to the equilibrium composition because the changes in temperature are often so fast that the chemical reactions cannot follow.

B2.2.2 Identification of Atoms and Molecules

Without a doubt, the identification of unknown elements using the wavelength of the emitted spectral lines is the oldest application of emission spectroscopic measurements. In plasma wind tunnels, the identification of different particles is of particular interest for:

- Proving the existence of ionized species
- Detecting erosion products of the electrodes which pollute the plasma

- Determining the plasma regions where recombination, dissociation or ionization processes occur (e.g. NO-formation due to catalytic effects).
- Detecting erosion products of the heat shield materials.

As an example, Fig. B2.13 shows the emission spectrum taken from the experimental simulation of the entry conditions into the atmosphere of the Saturn moon Titan which was realized by using a mixture of nitrogen and methane as working gas in the plasma wind tunnel [B2.10].

For the atoms, the index ₁ means that the neutral species is regarded while _{II} means the first ionization stage. For molecules the ionization is characterized by ⁺ (for example N_2^+ is ionized molecular nitrogen).

B2.2.3 Temperature Determination from Atomic Radiation

The information about the plasma temperature is contained within the intensity and the shape of the spectral lines of the radiating species. Replacing the number density of the excited state n_n under the assumption of a Boltzmann distribution as introduced in equation (B2.35), the spectral emission coefficient ϵ_{nm} of a spectral line as introduced in equation (B2.2) can be written as:

$$\epsilon_{nm} = \frac{1}{4\pi} h\nu_{nm} A_{nm} n \frac{g_n}{g_0} \exp\left(-\frac{E_n}{kT}\right) \quad (\text{B2.38})$$

If all quantities that remain constant for one species at the same plasma state are combined in the constant C which also contains common factors that influence the measured radiation such as the solid angle of the focusing system, an equation for the measured line intensity of the transition from state n to m is obtained:

$$I_{nm} = C \nu_{nm} A_{nm} g_n \exp\left(-\frac{E_n}{kT}\right) \quad (\text{B2.39})$$

$$\text{or} \quad \ln\left(\frac{I_{nm}}{v_{nm}A_{nm}g_n}\right) = \ln(C) - \frac{E_n}{kT} \quad (\text{B2.40})$$

Even without knowledge of the particle density, a determination of the temperature by a comparison of two emission lines can be performed. For this method, the fact is applied that the above equation formally appears as a straight line equation $y = b + mx$ with y and x being the logarithmic expression and the excitation energy respectively and where the slope contains the desired temperature. With only two points which means two emission lines the slope and therefore the temperature can be determined. To increase the quality of the measurement, usually more than two lines are used. This method is called Boltzmann plot and can be used both for determining atomic and molecular temperatures as explained in detail in the following section.

B2.2.4 Determination of Molecular Temperatures

In most cases, the distribution of the number densities of the excited rotational and vibrational levels follows a Boltzmann distribution.

If single rotational vibrational lines can be spectrally resolved within the measurements of the molecular bands, the application of a Boltzmann plot is possible to determine the molecular temperatures.

A closer look at equation (B2.30) for the intensity of single emission lines gives the basic principles for temperature determination. Within one electronic transition the ratio of different emission lines is only a function of rotational temperature if the vibrational quantum number does not change.

Therefore, different rotational lines of the same vibrational transition can be used to determine the rotational temperature. Knowing T_{rot} , emission lines of different vibrational transitions can be used to determine the vibrational temperature if absolute intensities are measured. Determining the electronic temperature is only possible if different electronic transitions of the same molecule can be detected. But even in this case, the assumption of a Boltzmann distribution for the electronic states is necessary. Contrary to the rotational and vibrational states, this assumption is seldom fulfilled and has to be verified in any case.

Within real measurements, the spectral distance between corresponding lines of different vibrational transitions is rather large which causes severe problems in performing the necessary measurements. Thus, the usual application of the Boltzmann method is given by the determination of the rotational temperature.

If only emission lines of one vibrational transition are chosen, the terms which contain the electronic and vibrational quantities can be concluded in a constant C . Similar to the procedure in the case of the atomic radiation, equation (B2.30) can then be written as:

$$\ln\left(\frac{I_{v'J'-v''J''}\lambda^4}{S_J}\right) = \ln(C) - \frac{hc}{kT_{\text{rot}}} F'(v', J') \quad (\text{B2.41})$$

Here, $I_{v'J'-v''J''}$ is the intensity of the regarded rotational line at the wavelength λ . The *London-Hönl factor* S_J gives the statistical weights of the different transitions as corresponds to the statistical weights g_n used for the atoms. If the intensities of different rotational lines are measured and plotted over the rotational energy F , in the case of a Boltzmann distribution a straight line is formed where the slope $-1/kT_{\text{rot}}$ contains the desired rotational temperature.

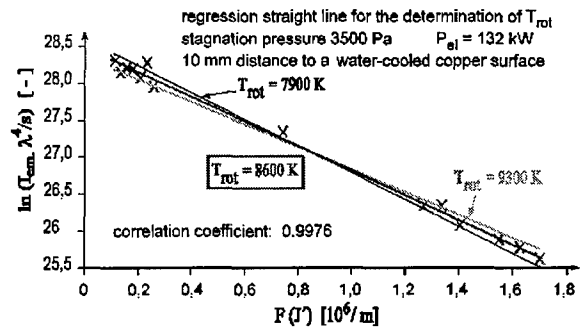


Fig. B2.14: Typical Boltzmann plot used for determining T_{rot}

In Fig. B2.14 the application of this method to the emission of a N_2^+ -molecular band is shown [B2.11]. The theoretical linear relation can be seen clearly which validates the assumption of a Boltzmann distribution.

If different vibrational transitions are regarded, equation (B2.41) transforms into:

$$\ln\left(\frac{I_{v'J'-v''J''}\lambda^4}{S_J}\right) = \ln(C) - \frac{hc}{kT_{\text{vib}}} G'(v') - \frac{hc}{kT_{\text{rot}}} F'(v', J') \quad (\text{B2.42})$$

To obtain a straight line equation equivalent to (B2.41) the upper vibrational and rotational quantum numbers of the chosen emission lines have to be the same for all lines. This means that the lines which have to be evaluated are found in band systems with a different vibrational quantum number difference Δv (compare Fig. B2.11) yielding a large spectral distance. In the case of N_2^+ , the band systems from $\Delta v = -2$ up to $\Delta v = 2$ can typically be observed. Therefore, the maximum number of data points for each Boltzmann plot would be reduced to about five points.

If the measurement of spectrally resolved lines is possible only within a limited wavelength region, equation (B2.42), which no longer has the formal qualities of a straight line equation, has to be used directly for evaluation. It is no longer possible to use a Boltzmann plot to determine the rotational temperature. The vibrational temperature now has to be determined using the ratios of the intensities of different emission lines. In the logarithmic form, these ratios appear as differences. Still, the constant C which now includes only the partition functions and the terms due to the electronic transition is eliminated

from the equation. Solving for T_{vib} yields for two different emission lines:

$$T_{vib} = - \frac{G'(v'_1) - G'(v'_2)}{\frac{F'(v'_1, J'_1) - F'(v'_2, J'_2)}{T_{rot}} + \frac{k}{hc} \ln \left(\frac{I_{v'j'-v'j',1} \lambda_1^4 S_{J,2}}{I_{v'j'-v'j',2} \lambda_2^4 S_{J,1}} \right)} \quad (B2.43)$$

Besides the Boltzmann plot, a low resolution temperature determination can also be done by comparing a simulation of the molecular bands with measured data. For this purpose, a simulation of the quantum mechanical processes has to be done. The spectra for different temperature couples (here T_{rot} and T_{vib}) are computed and the numerically determined data are compared with the measurement. The spectrum which shows the highest resemblance to the measured spectrum gives the desired temperatures [B2.12]. One important presumption is that each simulated spectrum can be accurately related mathematically to a certain couple of the parameters of the model (in this case T_{rot} and T_{vib}). Figure B2.15 shows a parameter variation for the selected molecular bands [B2.13]. The left diagram shows a variation of rotational temperature while electronic and vibrational temperatures were kept constant. The right diagram shows a variation of both T_{rot} and T_{vib} .

The big advantage of this method compared to the Boltzmann plot is the much lower measurement time needed and the possibility for the simultaneous measurement of both T_{rot} and T_{vib} . Only with this method is the determination of the temperature distribution within the boundary layer in front of a material probe as described in section B2.3.3 possible with a reasonable measurement time.

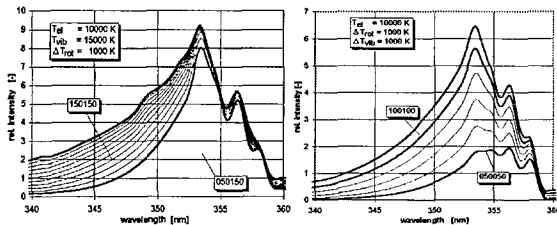


Fig. B2.15: Influence of the different temperatures on the molecular band structure: left - variation of T_{rot} , T_{el} and T_{vib} kept const. right - variation of T_{rot} and T_{vib} , T_{el} kept const.

Recently, the simulation has been extended from pure N_2^+ to a superposition of N_2^+ and N_2 emission [B2.14]. Figure B2.16 illustrates the data processing procedure and the temperature determination method in a flow chart.

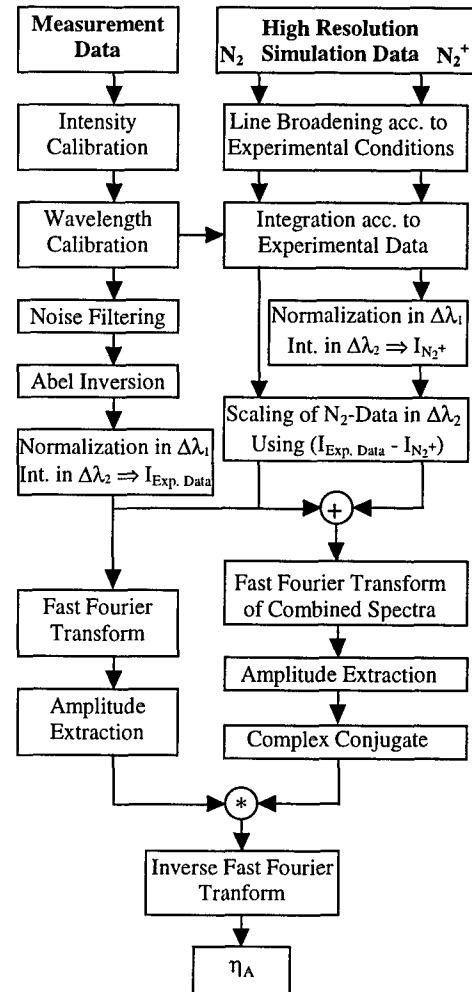


Fig. B2.16: Flow chart of the data processing procedure and the temperature determination method.

B2.2.5 Determination of Particle Densities

Generally, the determination of particle densities from the measured emission spectra is also possible. Again, the most important assumption is the Boltzmann distribution. Additionally, the corresponding temperature must be accurately known and the measured data have to be calibrated to absolute intensities.

To determine atomic particle densities, the emission coefficient ϵ_{nm} in equation (B2.38) (see section B2.2.3) has to be replaced by the intensity calibrated measured emission I_{nm} and the equation has to be solved for the particle density n :

$$n = I_{nm} \frac{4\pi e^{\frac{E_n}{kT}} g_0}{h\nu_{nm} A_{nm} g_n} \quad (B2.44)$$

Theoretically, the determination of molecular particle densities from the emission spectrum is also possible. The desired particle density is contained in the constant K in equation (B2.30) (see section B2.1.4). Although the assumption of Boltzmann distributed

rotational and vibrational energies is often valid, an application to the electronic levels is not necessarily possible.

Therefore, the determination of molecular particle densities with other methods such as laser induced fluorescence (compare section B5.1) is better suited.

B2.3 Plasma Wind Tunnel Application

During re-entry, as well as in the simulation in a plasma wind tunnel, thermal or chemical equilibrium can not be assumed in wide ranges. Sometimes not even a Boltzmann or Maxwell distribution is present. In this case, an interpretation of the measured data becomes rather complicated.

So an important task is the verification of the above-mentioned assumptions. The presence of a Boltzmann distribution can be verified by the linearity of a Boltzmann plot as described in section B2.2.4; the validation of a Maxwell distribution can be done using electrostatic probes (compare section A7.1). The equilibrium condition of the plasma state can be estimated using temperature measurements with electrostatic probes (A7.1) and emission spectroscopic temperature measurements of atomic and molecular temperatures (B2.2).

The next sections describe the experimental set-up for emission spectroscopic measurements, the intensity and wavelength calibration procedures and the Abel inversion as important factors for evaluating the measured data.

B2.3.1 Experimental Set-up

The results of emission spectroscopic measurements are influenced by different factors. Generally, the measured data can not be used for further evaluation without any corrections. Although modern spectrometers and monochromators are normally wavelength calibrated, an additional wavelength calibration should be performed prior to each measurement because testing time is often limited and very expensive. In any case, a spectral intensity calibration (either relative or absolute) is necessary to enable a comparison of emission lines at different wavelengths or to determine thermodynamic quantities from the absolute intensity of the measured emission.

Measurements in different wavelength regions require different capabilities of the experimental set-up. For measurements of molecules in the ultraviolet wavelength region, the spectral transmittance of the optical elements of the experimental set-up and the spectral efficiency of the detector have to be optimized for utilization in the UV because at most plasma states the emission of the molecules is already weak. Fused silica lenses and windows as well as mirrors are the most commonly used optical elements. In any case, a spectral calibration of the set-up has to be done which will be described below.

At higher wavelengths up to the near infrared, the choice of materials for the optical elements is rather easy because most optical materials have sufficient characteristic properties in this wavelength region. On the other hand, most detectors suffer from decreasing efficiency close to the infrared especially if they are sensitive in the UV region. Another important disturbance is second order radiation. Due to self-absorption in air below 185 nm this effect gains importance only at wavelengths above 390 nm. To prevent the measured data from second order radiation, spectral filters are used to block radiation at wavelength below the region of interest.

Figure B2.17 shows a typical set-up for emission spectroscopic measurements. The emitted radiation is focused onto the entrance slit of a spectrometer where the spectral decomposition takes place. At the exit of the spectrometer, the transmitted light is collected by a detector. The focusing elements of the optical set-up have a remarkable influence on the results. In the set-up presented all lenses have been replaced by mirrors to minimize chromatic aberration which causes a shifting of the focus. If extensive wavelength ranges have to be detected, this shifting causes significant errors in the measured data.

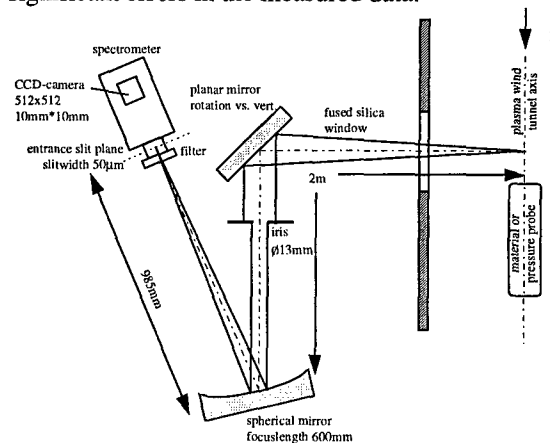


Fig. B2.17: Typical experimental set-up for emission spectroscopic measurements

The mirrors are used for focusing and for adjusting the measurement position inside the vacuum tank. Because of the comparatively large focal length of 650 mm, a precise adjustment of the optics is an important requirement for a successful measurement. For the adjustment procedure, the detector is replaced by a laser. The laser light has to take the reverse optical path and enables both an adjustment of the optical axis and of the measurement position.

If the available space is limited or if the direct optical path is somehow blocked, e.g. for measurements in the arc chamber of the plasma generator, the set-up shown above is not well-suited to perform emission spectroscopic measurements. In this case, the emission can be transferred to the spectrometer using fiber optics. The spectrometer needs no direct optical access to the measurement position. Figure B2.18 shows such a set-up.

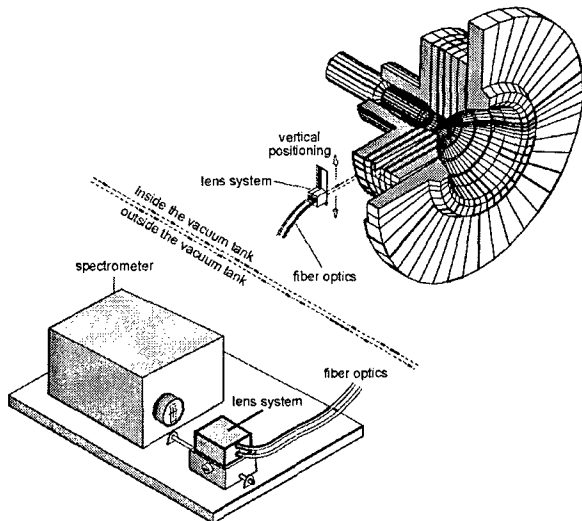


Fig. B2.18: Optical set-up using fiber optics

B2.3.2 Measurement Grid

Emission spectroscopic measurements have been used to characterize the processes within the boundary layer in front of a probe in the plasma jet [B2.5-9]. Some results are given in section B2.4. Due to the non-intrusive character of the measurement method these kinds of measurements are well-suited for such an application.

For this purpose, a measurement grid in front of the probe as shown in Fig. B2.19 had to be developed.

To perform an Abel inversion, radial profiles over the whole radial extension of the plasma jet have to be recorded. The axial distances between the measurement positions are chosen smaller in regions of special interest (normally close to the probe surface) where the gradients are high and larger in regions with low gradients away from the probe surface to reduce the amount of data. The grid is adapted to the dimensions of the boundary layer.

During one test, 3000 to 7000 spectra are recorded. With a measurement time-optimized set-up including an imaging spectrometer and a CCD-camera used as detector which can detect all axial positions in one shot, the measurement of one complete scan requires a measurement time between 20 and 30 minutes.

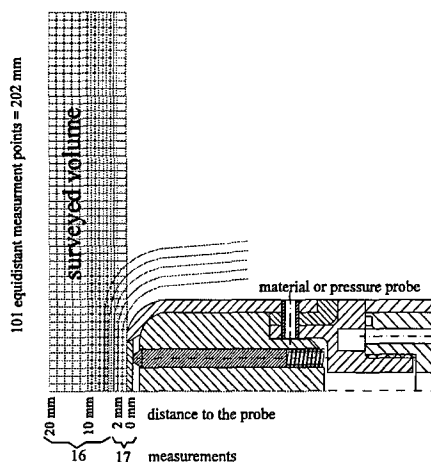


Fig. B2.19: Measurement grid in front of a probe

B2.3.3 Wavelength Calibration

Generally, a wavelength calibration should be done. Most spectrometer software offers a procedure to calibrate the single detector elements although a manual calibration is also possible. For this purpose, the radiation of a calibration lamp with emission lines at known spectral positions is measured. Figure B2.20 shows the measured spectrum of an Hg-lamp which is one of the most commonly used calibration lamps.

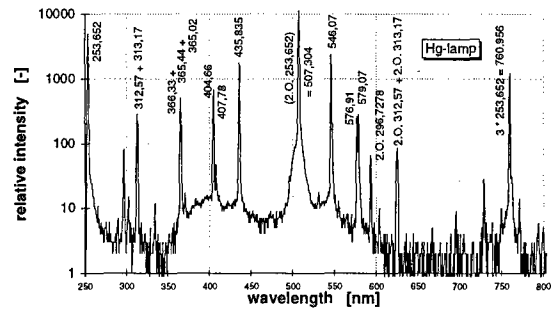


Fig. B2.20: Spectrum of an Hg-calibration lamp

Normally, the spectrometer is adjusted until one of the known emission lines appears in the center of the detector array. Other known lines are used to perform a polynomial fit (second order is most sufficient) for the wavelengths of the other pixels.

B2.3.4 Intensity Calibration

If the absolute intensity of the emission lines has to be detected, it is obvious that the sensitivity of the detector has to be calibrated. But even if only relative intensities have to be compared, at least a relative calibration has to be done. The calibration is done by measuring a calibration lamp with already calibrated continuous emission (e.g. a tungsten band lamp for the visible wavelength region or a deuterium lamp for the UV).

Sometimes, only the spectrometer-detector couple is intensity calibrated which is done by illuminating the whole entrance slit of the spectrometer with the light of a calibration lamp. In this case, the calibration lamp is placed directly in front of the entrance slit. The advantage is that the spectrometer-detector combination has to be calibrated only once for a given wavelength range. The disadvantage of this calibration is that all spectral transmissions of windows, filters and lenses in the optical path have to be known accurately. Additionally, the solid angle and the imaging factor have to be included in the final evaluation.

The better but also more time consuming method is to place the calibration lamp at the measurement position and use the same optical path as in the measurement which has to be calibrated. In this case, all influences on the signal are included in the calibration procedure.

Figures B2.21 and B2.22 show the calibrated emission of two calibration lamps as tabulated by the manufacturer and the measured values. The

correction factors for the single detector elements are included in the diagram. The emission of the tungsten band lamp drops down in the ultraviolet wavelength region where the deuterium emission is rather strong. On the other hand, the emission of the deuterium lamp is no longer continuous in the visible wavelength range. Thus, only a combined calibration using both lamps gives a valid correction factor. Since the deuterium lamp itself is calibrated to spectral irradiance, the correction factors have to be scaled by a constant factor to those of the tungsten band lamp which is calibrated to spectral radiance.

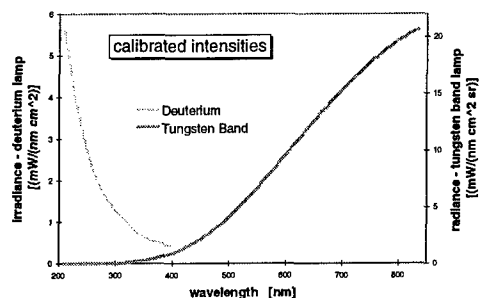


Fig. B2.21: Calibrated intensities of the different calibration lamps

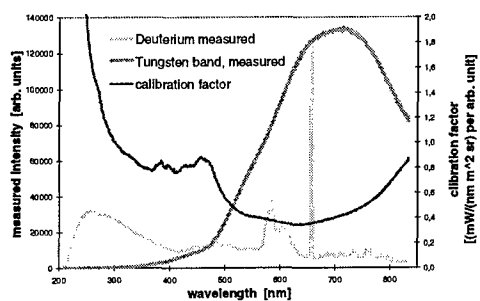


Fig. B2.22: Calibration measurement with different calibration lamps

B2.3.5 Determination of Local Quantities

A main disadvantage of emission spectroscopic measurements is the fact that the measured signal always consists of an integration along the line of sight as illustrated in Fig. B2.23.

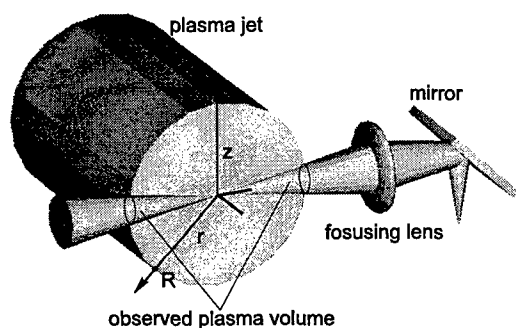


Fig. B2.23: Typical geometrical configuration

The Abel inversion is a mathematical technique which allows a reconstruction of the local values from a vertical profile of measured (that means integrated) intensities $I(z)$ as long as rotational

symmetry of the radiation within the measured volume is given.

The radiation of the plasma volume is described by the emission coefficient $\epsilon(r)$. The measured integrated intensity $I(z)$ is coupled to $\epsilon(r)$ by the *Abel equation*:

$$I(z) = 2 \int_{r=z}^R \frac{r}{\sqrt{r^2 - z^2}} \epsilon(r) dr \quad (\text{B2.1})$$

R is the radius of the measured volume while r is the local radius. Solving for $\epsilon(r)$ gives

$$\epsilon(r) = -\frac{1}{\pi} \int_{z=r}^{\infty} \frac{dI/dz}{\sqrt{z^2 - r^2}} dz \quad (\text{B2.2})$$

In most cases an analytical solution is hard to find because a valid approximation of the integrated intensities is not available. Therefore, a numerical solution is used where the emission coefficient is considered to be constant over finite rings of the regarded volume. A refinement can be implemented if a linear transition between the measurement position is postulated to approximate the continuous course in the real plasma. Figure B2.24 illustrates the principle of the numerical Abel inversion.

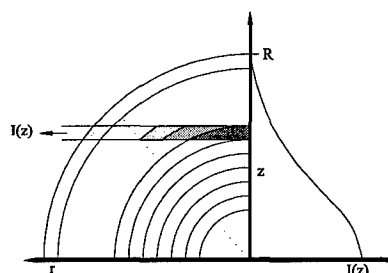


Fig. B2.24: Principle of the Abel inversion

Figure B2.25 shows the measured intensities $I(z)$ and the Abel-inverted intensity $i(r)$. The Abel-inverted intensities drop down to negative values at the borders of the plasma jet. Theoretically, this could be caused by absorption, but more likely these values are caused by numerical errors which can accumulate especially in the border region where intensities are rather low. Generally, the Abel inversion reacts very sensitively to functions which are not constantly differentiable. For this reason, a smoothing of the measured data often has to be performed first.

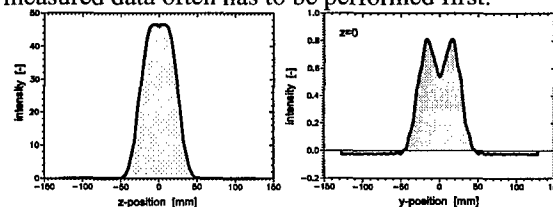


Fig. B2.25: Measured (left) and Abel-inverted (right) intensity distribution

The principle discussed is easily applicable if the local intensity distribution within the plasma is of particular interest as it was postulated for temperature determination methods. The problem becomes more complicated if, in addition to the intensity distribution, the line profile also has to be resolved, for example to determine electron densities from Fabry-Perot measurements (see section B4). Here, the

line broadening changes over the cross section as the electron density changes.

The measured intensity $I(z)$ within the Abel integral equation is not only described by the emission coefficient $\epsilon(r)$ but also by the line profile of the emission lines. The Abel equation becomes:

$$\epsilon(r)\Delta\lambda_B^2(r) = \frac{1}{\pi} \int_{z=r}^{\infty} \frac{d(I(z)\Delta\lambda_B^2(z))/dz}{\sqrt{z^2 - r^2}} dz \quad (\text{B2.3})$$

This expression gives a relation between the integrally measured broadening $\Delta\lambda_B(z)$ of an emission line at the wavelength λ with the local broadening $\Delta\lambda_B(r)$. If $\epsilon(r)$ is known from a conventional Abel inversion, the local broadening can be calculated.

The above-mentioned evaluation procedure is also applicable for Fabry-Perot measurements but one problem arises if plasma velocities are to be determined (see section B4.4). In this case, the optical path is no longer rectangular to the plasma axis. Here, the assumption of rotational symmetry is no longer given and the evaluation of the measured data becomes more difficult [B2.15].

B2.4 Measurement Results

The emission spectroscopic measurements at the IRS concentrate on the investigation of the flow field in front of a probe in the plasma jet although investigations of the free stream are also carried out.

In this section, some overview spectra are presented before the investigation of the boundary layer region by the measurement of atomic and molecular emission, of molecular temperature distributions and of erosion products are discussed. All measurements were taken at the MPD-driven plasma wind tunnel PWK 2.

B2.4.1 Overview Spectra

Figure B2.26 shows the radiating species measured at the plasma condition with a mass flow rate of 8 g/s and a stagnation pressure at the probe position of 800 Pa yielding a SiC surface temperature of 1700°C in front of a glowing probe and a water-cooled copper surface.

Generally, the emission spectra at the subsonic air flows typically investigated are dominated by the emission of the molecules NO, N₂ and N₂⁺ in the ultraviolet and by the molecular emission of N₂ and the atomic emission of nitrogen N and oxygen O in the wavelength region from the visible to the near infrared. In front of a glowing material probe, strong emission of erosion products such as Si, CN and C can be seen in the UV.

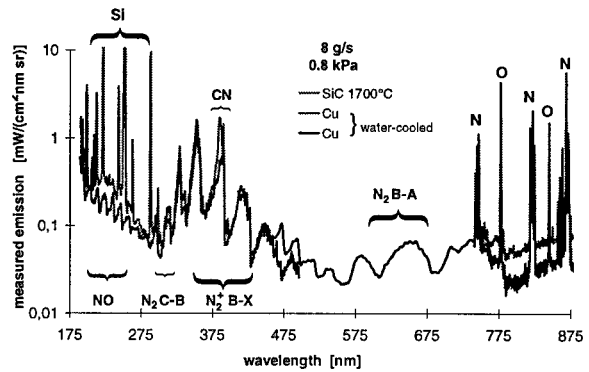


Fig. B2.26: Measured plasma emission in front of a water-cooled copper surface and an SiC material probe at 1700°C

B2.4.2 Integrated Emission as Indicator for the Boundary Layer

There are several different purposes for these kinds of measurements. Besides the characterization of the boundary layer shape, a main purpose was the detection of NO inside the boundary layer with the available emission spectroscopic equipment [B2.16]. In Fig. B2.27 the measured emission distribution of NO in front of a water-cooled copper surface positioned at the plasma jet axis at a plasma state with a mass flow rate of 8 g/s and a stagnation pressure of 800 Pa at a distance to the plasma source of 368 mm is depicted. The rise in NO radiation supports the theory of NO formation in front of high catalytic surfaces such as copper.

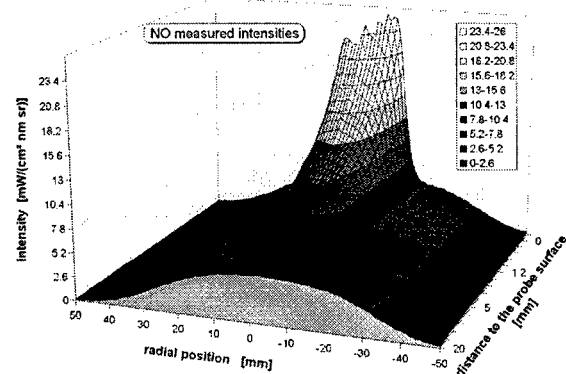
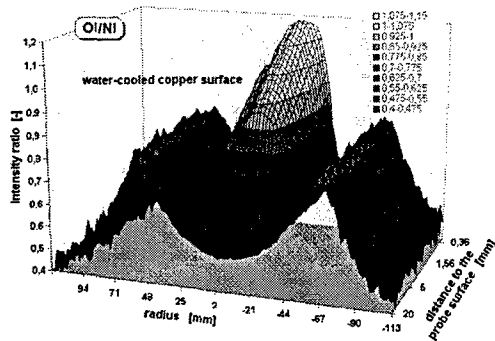


Fig. B2.27: Measured NO intensities in front of a water-cooled probe

The ratio of N₁ to O₁ is also regarded as a good indicator for the boundary layer borders. Figure B2.28 shows the intensity ratios obtained from the measured intensities of O₁ and N₁ [B2.16]. The profile indicates a location of the boundary borders at about 8 mm to the probe surface. The increase of this ratio at the borders of the plasma jet indicates an decrease of N atoms in relation to the O atoms due to their higher recombination energy.



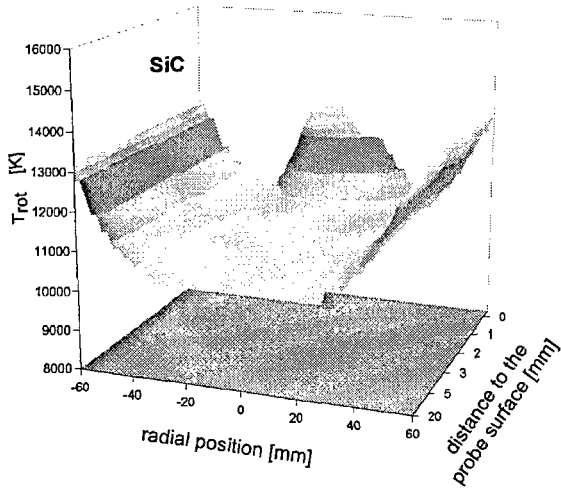


Fig. B2.14: Rotational temperature distribution in front of an SiC sample at 1280°C.

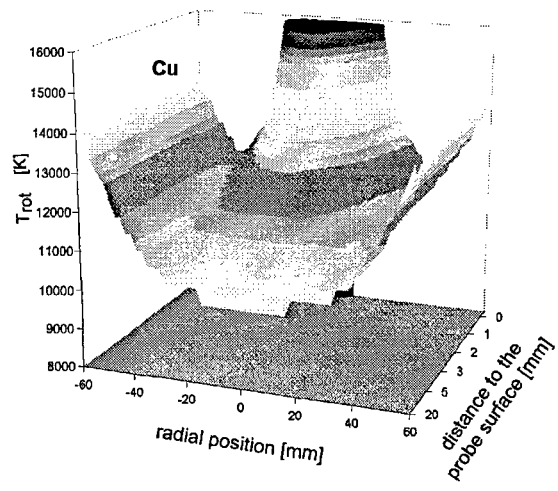


Fig. B2.15: Rotational temperature distribution in front of a water-cooled copper surface.

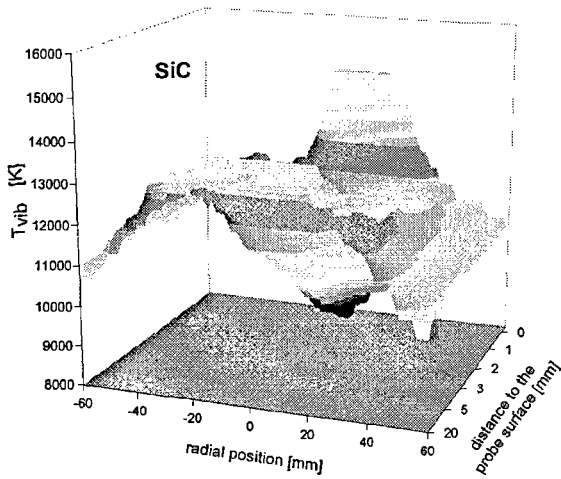


Fig. B2.16: Vibrational temperature distribution in front of an SiC sample at 1280°C.

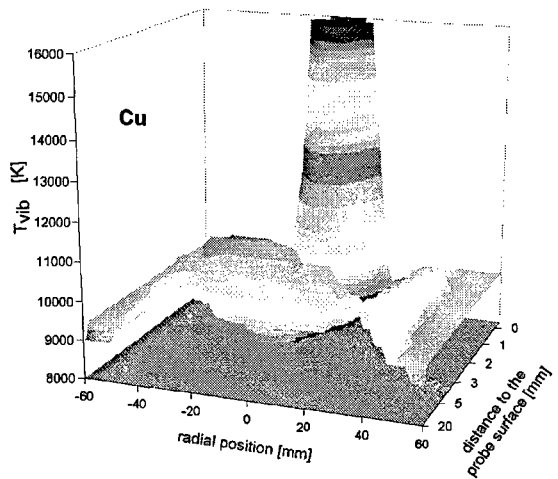


Fig. B2.17: Vibrational temperature distribution in front of a water-cooled copper surface.

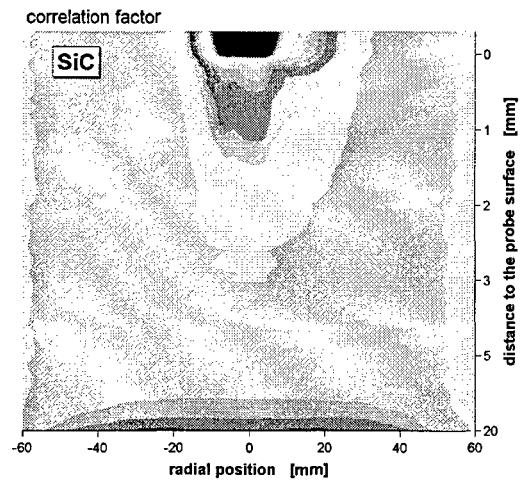


Fig. B2.18: Correlation factors in front of an SiC sample at 1280°C.

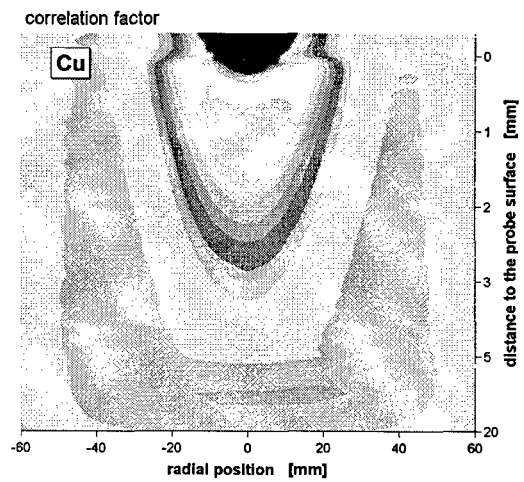


Fig. B2.19: Correlation factors in front of a water-cooled copper surface.

References

- [B2.1] Herzberg, G., "Atomic spectra & atomic structure", Dover Publications, New York, 1944.
- [B2.2] Hellwege, K. H., "Einführung in die Physik der Atome", Springer-Verlag Berlin Heidelberg New York, 1974.
- [B2.3] Striganov, A.R., Sventitskii, N.S., "Tables of Spectral Lines of Neutral and Ionized Atoms", IFI/Plenum, New York - Washington, 1968.
- [B2.4] Wiese, Smith, Miles, "Atomic Transition Probabilities", Volume I+II, U.S. Department of Commerce, Washington D.C., 1969.
- [B2.5] Park, C., "Calculation of Nonequilibrium Radiation in the Flight Regimes of Aeroassisted Orbital Transfer Vehicles" in Thermal Design of Aeroassisted Orbital Transfer Vehicles, Progress in Astronautics and Aeronautics, Volume 96, AIAA, 1985, pp. 395-418.
- [B2.6] Smith, A.J., Gogel, T.H., Vandervelde, P., "Plasma Radiation Database PARADE", Final Report of the ESA/ESTEC TRP, Contract 11148/94/NL/FG, April 1996.
- [B2.7] Hellwege, K. H., "Einführung in die Physik der Molekeln", Springer-Verlag Berlin Heidelberg New York, 1989.
- [B2.8] Herzberg, G., "Molecular Spectra and Molecular Structure: Vol. I, Spectra of Diatomic Molecules, D. Van Nostrand Company, LTD, 1950.
- [B2.9] Laux, C. O., "Optical Diagnostics and Radiative Emission of Air Plasmas", HTGL Report No. T-288, Stanford University, CA, USA, August 1993.
- [B2.10] Röck, W., "Simulation des Eintritts einer Sonde in die Atmosphäre des Saturnmondes Titan in einem Plasmawindkanal", Dissertation, Fakultät Luft- und Raumfahrttechnik, Universität Stuttgart, 1998.
- [B2.11] Winter, M.W., Auweter-Kurtz, M., Kurtz, H.L. and Park, C., "Investigation of an Equilibrium Condition Boundary Layer in Front of a Material Probe in a Subsonic Plasma Flow", 31st AIAA Thermophysics Conference, New Orleans, LA, June, 1996.
- [B2.12] Winter, M.W., Auweter-Kurtz, M. and Kurtz, H.L., "Spectroscopic Investigation of the Boundary Layer in Front of a Blunt Body in a Subsonic Air Plasma Flow", AIAA 97-2526, 32nd AIAA Thermophysics Conference, Atlanta, GA, June 1997.
- [B2.13] Fromm, M.A., "Charakterisierung der Probenumströmung einer Materialprobe im Plasmastrahl mit emissionsspektroskopischen Mitteln", Diplomarbeit IRS-97-S-12, Institut für Raumfahrtssysteme, Universität Stuttgart, Stuttgart, Germany, 1997.
- [B2.14] Winter, M.W., Auweter-Kurtz, M., "Emission Spectroscopic Investigation of the Boundary Layer in Front of a Blunt Body in a Subsonic Air Plasma Flow", 3rd European Symposium on Aerothermodynamics for Space Vehicles, ESTEC, Noordwijk, The Netherlands, November, 1998.
- [B2.15] Habiger, H., "Elektrostatische Sonden und Fabry-Perot Interferometrie zur Untersuchung von lichtbogenbeheizten Plasmen für Triebwerksanwendungen und Wiedereintrittssimulation", Dissertation, Institut für Raumfahrtssysteme, Fakultät Luft- und Raumfahrttechnik, Universität Stuttgart, 1994.
- [B2.16] Winter, M.W. and Auweter-Kurtz, M., "Boundary Layer Investigation in Front of a Blunt Body in a Subsonic Air Plasma Flow by Emission Spectroscopic Means", AIAA 98-2460, AIAA 7th Joint Thermophysics and Heat Transfer Conference, Albuquerque, NM, June, 1998.

B3 Absorption Spectroscopy

With absorption spectroscopy, the absorption of electromagnetic radiation by the particles of the transmitting medium is investigated. The method is based on the same quantum mechanical processes as emission spectroscopy, only that energy is absorbed and not emitted by the plasma.

As already seen, atoms and molecules emit energy in form of electromagnetic waves if they are thermally or electrically excited. Accordingly, light is absorbed at discrete lines if the radiation of a continuous light source is transmitted through a gas. These absorption lines correspond to the discrete energy levels necessary for the excitation of atoms and molecules in the gas [B3.1]. The continuous spectrum of the calibration lamp observed through the absorbing medium (e.g. the gas or plasma) therefore shows weaker intensities at these discrete lines. If the medium is regarded rectangular to the optical axis where the continuous radiation is not visible, an emission line at the same wavelength as the absorption line is visible due to the short life time of the excited state. It can be shown that not only the wavelength but also the amount of radiation is the same in emission and in absorption. This phenomenon is called resonance fluorescence. Figure B3.1 shows the absorption and the emission spectrum of sodium.

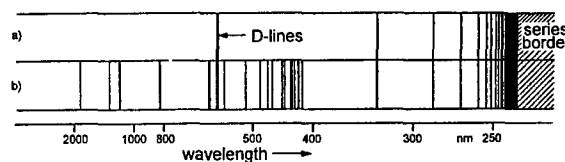


Fig. B3.1: a) Absorption and b) emission lines of sodium

Usually absorption spectroscopy is used at temperatures below 3000K. At these plasma states, the biggest part of the atoms and molecules ($\approx 99.9\%$) is in the ground state. In this case, only absorption from these ground states is possible. The resulting series are called main series, the lines themselves resonant lines. If there are remarkable amounts of excited states, the transitions already known from the emission spectroscopic formulas can be obtained and the absorption spectrum becomes very similar to the emission spectrum.

Due to the high temperatures in plasma wind tunnels, an application of absorption spectroscopy is seldom possible. A more common application is absorption spectroscopy in flames, where temperatures are lower [e.g. B3.2 and B3.8].

B3.1 The Coefficient of Absorption

The total amount of energy absorbed per time and volume unit can be written as:

$$e_{abs} = B_{mn} n_m I_\nu h\nu \quad (\text{B3.1})$$

with:

n_m number of particles in the absorbing state per volume unit

$h\nu$ radiation energy

I_ν spectral energy density

The factor B_{mn} is the Einstein transition probability for absorption for the transition $m \rightarrow n$ and describes the number of absorbing particles per time unit and per spectral energy density in $[\text{m}^3\text{J}^{-1}\text{s}^{-2}]$. The product $B_{mn} I_\nu$ is an expression for the portion of particles in the state m which absorb one photon with the energy $h\nu$ per time unit.

The total amount of energy absorbed per time and volume unit can also be expressed by the product of the number of absorbed photons and their energy:

$$e_{abs} = \kappa_{mn} n_m c I_\nu \quad (\text{B3.2})$$

where κ_{mn} is the coefficient of absorption. Combining both equations yields:

$$\kappa_{mn} = \frac{h\nu}{c} B_{mn} \quad (\text{B3.3})$$

The coefficient of absorption has the unit $[\text{m}^2\text{s}]$ and is a measure for the amount of radiation of the frequency ν that can be absorbed by one particle.

In reality, similar to the emission lines each absorption line has a certain line width which is produced by various effects (see section B2.1.2). Basically, the expression for coefficient of absorption represents an integration over this line width and can be written as:

$$\kappa_{mn} = \int \kappa'_{mn}(\nu) d\nu \quad (\text{B3.4})$$

B3.2 Absorption Measurements of Particle Densities

Atoms are capable of absorbing radiation in only a very narrow frequency interval. For this reason, the radiation source has to meet some special requirements. Although continuous radiators emit a high total amount of radiation, the emitted intensity within the important spectral region is mostly too weak to stimulate remarkable absorption. A lamp which emits the same spectrum as the investigated element or a laser is often a better choice.

With such a set-up, the selected spectral line has to be separated from the other emission lines emitted by the same element using a spectrometer. Figure B3.2 shows an experimental set-up for these kinds of measurements.

A line radiator such as a hollow cathode lamp (or a laser if available) emits the spectrum of the investigated element. Within the plasma, part of the incoming radiation is absorbed at the resonant line. This part is directly proportional to the amount of particles in the corresponding state of excitation. Spectral lines that don't exist in absorption are transmitted without any reductions. The number of excited particles in the low temperature range ($< 3000 \text{ K}$) is usually much smaller than the number of particles in the ground state. Therefore, in most cases the ground state particle density is determined by absorption spectroscopic measurements. After the spectral decomposition in the monochromator, the

absorption line is separated and all other emission lines are eliminated. The detector „sees” only one line. The comparison with the originally emitted line gives the absorption.

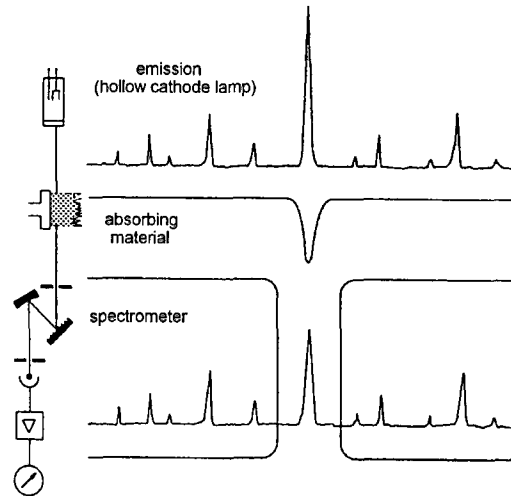


Fig. B3.3: Principle of absorption measurements

To determine n_m , the radiant energy fluxes have to be regarded. According to Lambert's law the relation:

$$\phi_{D\nu} = \phi_{0\nu} e^{-\kappa_{mn} n_m d} \quad (\text{B3.5})$$

is given, where $\phi_{D\nu}$ and $\phi_{0\nu}$ represent the spectral radiative flux prior to and after the transmission through the absorbing region of the thickness d .

If d is known and κ_{mn} can be determined for the specified absorption line, the particle density in the state m (usually the ground state) is obtained from:

$$n_m = \frac{1}{\kappa_{mn} d} \ln \frac{\phi_{0\nu}}{\phi_{D\nu}} = \frac{A}{\kappa_{mn} d} \quad (\text{B3.6})$$

The above equation is valid as long as the half width of the emission line of the radiation source is remarkably lower than that of the absorbing line. If not, a part of the emitted radiation at both (spectral) sides of the absorption line can not be absorbed which influences the results.

Furthermore, n_m has to remain constant over d . Otherwise, an Abel-inversion of the measured data has to be performed to obtain local particle densities (see section B2.3.5).

B3.3 Experimental Set-up

The principle set-up of an absorption spectrometer is rather simple and can be recognized in Fig. B3.2. But such a simple system has some important disadvantages:

As mentioned above, the number of excited particles in the low temperature range ($< 3000 \text{ K}$) is usually much smaller than the number of particles in the ground state. In spite of that, the emission of the absorbing region is known to disturb the absorption measurements of such a simple setup, especially if other elements (for example molecules with numerous emission lines) exist. These effects can become important. If it is not possible to separate the investigated line from other emission lines, so called *spectral interferences* are obtained. In this case, the

ratio $\phi_D/(\phi_0+\phi_E)$ is measured instead of ϕ_D/ϕ_0 , where ϕ_E is the intensity of an additional emission line of the frequency ν' . The observed absorption is smaller than its real value. In some cases, a negative absorption represented by a transmittance > 1.0 will result.

To eliminate disturbing emission lines, most absorption spectrometer work is based on the chopped-light (AC) principle which is illustrated in Fig. B3.3a and no longer on the simple continuous-light (DC) system. The experimental setup is almost the same but the radiation of the reference source is mechanically or electrically modulated with a certain frequency. The amplifier electronics are synchronized with this modulation frequency („selective amplifier”). Only the part of the radiation which is oscillating with the modulation frequency is amplified so that the disturbing emission, which does not oscillate, loses importance. Spectral interferences by disturbing emission are minimized.

Another refinement of this set-up which eliminates additional error sources is given by the two beam AC system, shown in Fig. B3.3b. With this system, the radiation of the primary radiation source is separated by a rotating mirror into a measured beam (ϕ_D) and a reference beam (ϕ_0). After ϕ_D has passed the absorbing volume, both beams are reunited. The electronics of the system builds the ratio of these two beams. Both beams are created by the same radiation source, pass the same monochromator, are detected by the same detector and are amplified by the same amplifier. If the rotation frequency of the mirror is higher than the expected disturbances, changes in the primary radiation source strength or fluctuations in detector sensitivity or amplifier power appear in both measured signals and no longer appear in the ratio of both signals.

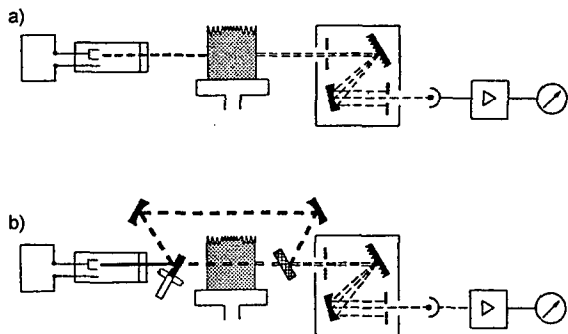


**Fig. B3.5: Working principle of absorption spectrometers: a) chopped-light-system
b) two beam AC-system**

B3.4 Applications

Some of the main applications for absorption spectroscopy are found in astrophysics. Here, numerous investigations of stars and the atmospheres of other planets have been done.

The concentration of atomic or molecular impurities in air can be determined using absorption spectroscopic methods [B3.3]. Molecular absorption spectroscopy in the far infrared wavelength region is used in shock tubes to investigate relaxation

processes [B3.4 to B3.6]. For these applications, lasers are used as light source. Also the investigation of combustion processes by absorption spectroscopic measurements of flames at rather low temperatures offers another broad range of applications.

Further fields of applications are the tracing of metal estimations either in solid food stuffs or organic materials (e.g. estimation of Mercury in water/fish by flameless Atomic Absorption Spectroscopy (A.A.S.), soil analysis). Another growing field is the application of A.A.S. in Clinical Chemistry [B3.8].

For plasma wind tunnel applications some restrictions to absorption spectroscopic methods appear. First, in most cases the temperatures are rather high yielding a highly excited plasma. Thus, the particle densities determined by absorption spectroscopy are no longer necessarily coupled to the ground state density.

Furthermore, the highest thermal loads on a reentering space vehicle occur at high altitudes and low pressures. Here the plasma usually can be regarded as optically thin which complicates absorption spectroscopic measurements.

If a laser is used instead of a continuous light source, a better sensitivity of the setup is provided but still the above mentioned restrictions are valid.

An exception is given if the absorbed energy is measured not by the attenuation of the laser beam but by the radiation of the stimulated emission. This method is called laser induced fluorescence and is described in section B5.1.

B3.4.1 Determination of the Plasma Transmittance

Even if the application as described above is not possible, absorption spectroscopic measurements can be very useful for the correction of all other optical measurement methods. In this case, the spectral range as well as the apparatus used are defined mainly by the measurement method to which the correction will be applied. The knowledge of the plasma absorbance and transmittance over a certain wavelength range for example is of particular interest if the surface temperature of a material probe inside a plasma jet is determined using pyrometers. Absorption of the radiation emitted by the material probe in the surrounding plasma yields errors in the determined surface temperature if the absorbed part of the emitted radiation can not be quantified. Absorption spectroscopy is in use for the selection of suitable filters for linear pyrometers in order to avoid this error source. The required transmittance measurements do not necessarily have to be performed spectrally resolved and a pyrometer can be used instead of a spectrometer (see Fig. B3.4).

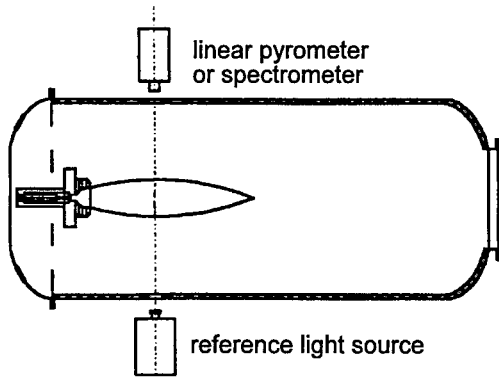


Fig. B3.6: Determination of the plasma transmittance

The reference source, which should radiate at the same magnitude of total radiation as the material to be measured, is placed outside the vacuum chamber and measured by the detector through the plasma. By comparing the measured signal without plasma I_R with the signal transmitted through the plasma I_{R+PI} the transmittance can easily be obtained. If the plasma itself emits within the selected wavelength region, an additional measurement of the plasma without the reference source I_{PI} has to be performed and subtracted from the signal of plasma and radiation source. The transmittance of the plasma is given by:

$$\tau_{PI} = \frac{I_{R+PI} - I_{PI}}{I_R} \quad (\text{B3.7})$$

If the measurement is performed using a spectrometer, the spectral transmittance is obtained.

References

- [B3.1] Welz, B., "Atomabsorptionsspektroskopie", Verlag Chemie, Weinheim, 1983.
- [B3.2] Baer, D. S., Nagali, V., Furlong, E. R., Hanson, R. K., Newfield, M. E., "Scanned- and fixed-wavelength absorption diagnostics for combustion measurements using a multiplexed diode-laser sensor system", *AIAA Journal*, 34, 1996, pp. 489-493.
- [B3.3] Unsöld, A., "Physik der Sternatmosphären: mit bes. Berücks. d. Sonne", Springer Verlag Berlin Heidelberg, 1955.
- [B3.4] Demtröder, W., "Laserspektroskopie, Grundlagen und Techniken", Springer Verlag, Berlin, Heidelberg, 1993.
- [B3.5] Klenk, W., "Spektroskopische Untersuchungen der Relaxationszone hinter Verdichtungsstößen in Luft mit einem Infrarot-Dioden-Laser", *Berichte aus der Luft- und Raumfahrttechnik*, D 93 Dissertation Universität Stuttgart, Shaker Verlag, Aachen, 1997.
- [B3.6] Brandt, O. and Roth, P., "Temperature measurement behind shock waves using a rapid scanning IR-diode laser", *Phys. Fluids*, 30, 1987, pp. 1294-1298.
- [B3.7] Moser, L. K. and Hindelang, F. J., "Shock-tube study of the vibrational relaxation of nitric oxide", in *Proceedings of the 17th International Symposium on Shock Waves and Shock Tubes*, 1989, pp.531-534.

- [B3.8] Thompson, K.C., Reynolds, R.J., "Atomic Absorption, Fluorescence and Flame Emission Spectroscopy", Charles Griffin & Company LTD, London, 1978.

B4 Fabry Perot Interferometry

A Fabry Perot interferometer is a high resolution spectral device based on the principle of multiray interference. It can be used to measure particle speeds and translational temperatures. Contrary to, for example, electrostatic probe measurements, this method provides the speed and temperature of the plasma by optical means. All of the necessary elements and devices for the measurements are located outside of the vacuum tank and therefore do not influence the plasma stream.

Axial and any azimuthal speed components of the accelerated plasma particles that appear are measured by means of the Doppler shift of their emission lines. The Doppler shift can be directly determined by simultaneously displaying the plasma line with a reference line which has not been shifted. With the conditions in the plasma wind tunnel PWK2 heavy particle velocities, for instance of atomic nitrogen, of approximately 1000 to 5000 m/s give Doppler shifts of approximately $\Delta\lambda_D \approx 0.002$ to 0.013 nm. To determine this shift, a high resolution spectrum is necessary. This spectrum can best be achieved by means of a so-called Fabry Perot Interferometer (FPI).

Furthermore, by determining the Doppler broadening the heavy particle translational temperature and if applicable the radial speed components of the plasma particles can be ascertained. As with emission spectroscopy, it is not a local measurement but a kind of average over the beam cross section that can be performed with this method. However, this disadvantage can also for the most part be eliminated with a subsequent mathematical resolution by means of an Abel inversion, as explained in section B4.5. The examined beam cross sections are, however, not axially symmetrical. This complicates the Abel inversion method explained in B2.3.5. A solution is given in [B4.1].

B4.1 Theoretical Principles of Fabry-Perot Interferometry

The Fabry-Perot interferometer was introduced by two French opticians, Charles FABRY and Alfred PEROT, in 1897. It essentially consists of two glass plates with a reflective coating on one side of each plate. The plates are positioned parallel to each other and are a few micrometers to a few meters apart.

The function of an FPI is based on the interference of a smooth wave through multiple reflections on two mirror plates. This phenomenon can also be explained by the multiple reflections in a plane parallel plate. One differentiates between so-called constructive and destructive interference. Construc-

tive interference appears when the phase shift of two overlapping, smooth waves is an integer multiple of 2π (see Fig. 4.1). Otherwise a destructive interference exists.

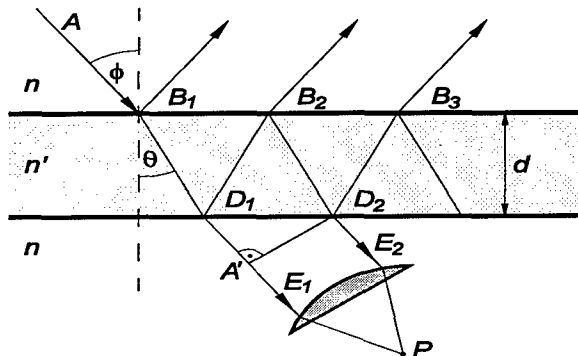


Fig. B4.1: Reflection in a glass plate

In the case of a Fabry-Perot interferometer the multiple reflection takes place on the translucent inner surfaces of two parallel glass plates. As Fig. B4.2 shows, an aperture partition in the focal point of lens 2 has the effect that only almost parallel light ($\theta \approx 0^\circ$) makes it through the FPI. If the medium has the refractive index n between the plates, the following condition for the intensity maximum of order m results:

$$m\lambda_0 = 2nd \tag{B4.1}$$

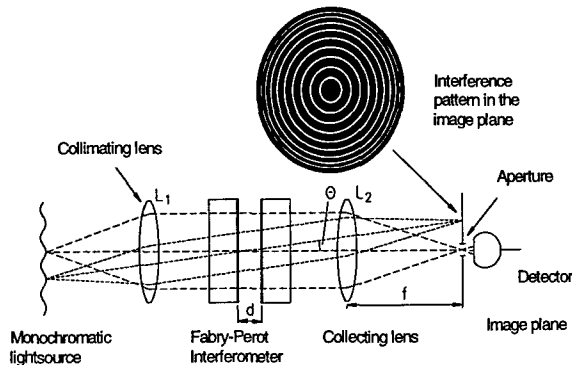


Fig. B4.2: Schematic construction of a Fabry-Perot interferometer

The Fabry-Perot interferometer can be adjusted to a declared wavelength by varying the parameters n or d . Changing the refractive index of the medium between the plates, for example by changing the pressure, is difficult. Modern FPIs are, therefore, adjusted by changing the distance between the plates. With the instrument in use at the IRS, one of the plates is shifted by means of piezoelectric. The piezoelectric elements are steered through a ramp generator and in this way they create a linear, periodic translational movement. This kind of scanning makes it possible to represent several interference arrangements of a certain wavelength or rather makes it possible for a defined, narrow wavelength area to go through.

B4.2 The Airy Function

The intensity I_T of the waves penetrating the FPI is among other things dependent on the transmission T of an FPI. The intensity is defined as the percentage permeability in the exact resonance distance of the mirror plates for a certain wavelength λ_0 , that means as a quotient of the intensities with and without FPI in the path of the detecting optics. The reduction of intensity caused by the FPI is essentially determined by the absorption and the scattering losses on the layers of the mirror-coating substrata, expressed by the mirror depending constant A_S and the reflection degree R on the mirror layers. In order to describe the relationship of the transmitting to incoming intensity I^T/I^i , the so-called Airy function is used which is given by:

$$\frac{I^T}{I^i} = \frac{(1-R)^2}{(1-R)^2 + 4R \sin^2 \frac{\delta}{2}} \tag{B4.2}$$

Here δ is the phase shift of an electromagnetic wave, caused by the reflections on the mirrors' surfaces. If δ is a multiple of 2π , then constructive interference occurs. In this case

$$\delta = \frac{4\pi}{\lambda_0} nd \cos \theta = 2\pi \cdot m \tag{B4.3}$$

is valid, with n as the refractive index inside the FPI, d as the spacing between the mirror plates, θ as the angle of the incoming wave, λ_0 as the wavelength of the transmitted light and m as the number of the interference order. The Airy function is shown in Fig. B4.2 for various degrees of reflection.

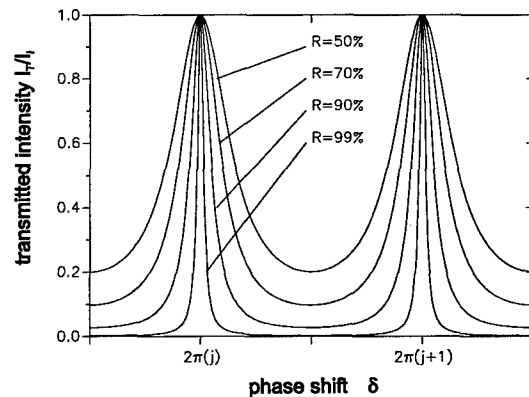


Fig. B4.2: Intensity relationship I_T/I_i for various degrees of reflection as a function of δ .

For a given optical thickness nd the Airy function describes a whole system of concentric interference rings when the order m of the interferences is equivalent to a whole number ($m = 1, 2, \dots$) according to Eq. B4.1. For small degrees of reflection R wide interference rings result and the contours become more and more defined as the degree of reflection increases.

A measure for the definition of the interference rings is given by the so-called half-width χ , which means the width of the profile at half the height of the

intensity maximum. For an interference ring of the order m the intensity is reduced by half. Hence it follows that the half-width of the interference ring results in:

$$\chi = \frac{4}{\sqrt{\frac{4R}{(1-R)^2}}} \quad (\text{B4.3})$$

The mirror plates used in the FPI at the IRS have a dielectric wideband coating with a degree of reflection of $R=94\%$ and a transmission area of 400 nm to 800 nm.

B4.3 Characteristic Quantities of a Fabry-Perot Interferometer

In order to effectively use an FPI as a high resolution spectrometer for a certain measurement task, one must optimize the system in order to maximize the resolution of the system.

B4.3.1 The Resolution

The resolution of the FPI determines the ability to separate two spectral lines which are very close together. The resolution is of great importance for the plasma wind tunnel application. For the practical use of the FPI for the purposes of detecting and identifying spectral lines, the Rayleigh criteria can be used (for Rayleigh see chapter B5). This is shown in Fig. B4.3a. Two spectral lines must be clearly separated by means of a drop in intensity to at least 81%. To use the FPI to determine the Doppler shift and broadening, which is explained in sections B4.4 and B4.5, one is dependent on an exact determination of the central wavelength λ_0 related to the maximum intensity. It is only possible to determine this when the observable profile of two spectral lines can be clearly separated at the height of their half-width.

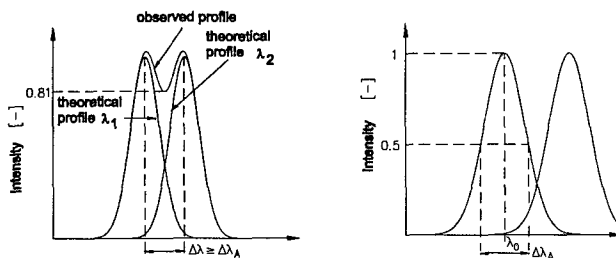


Fig. B4.3: a) unresolvable and b) resolvable spectral lines related to the measurement of Doppler effects

This is not the case in Fig. B4.3a. The central wavelength must be determined from the middle of the half-width as shown in Fig. B4.3b. According to this, the resolution $\Delta\lambda_A$ of the FPI is defined as the half-width of a perfectly monochromatic spectral line of the wavelength λ_0 . The useful resolution $\Delta\lambda_A$ depends on two characteristic quantities of a Fabry-Perot interferometer: the usable finesse F_N and the

free spectral area $\Delta\lambda_F$. Both are explained below. I is calculated from the quotient of both according to:

$$\Delta\lambda_A = \frac{\Delta\lambda_F}{F_N} = \frac{\lambda_0^2}{2ndF_N} \quad (\text{B4.7})$$

B4.3.2 The Finesse

The quality of an FPI is described by the so-called instrumental finesse F of the interferometer. The finesse is used to measure the performance of the FPI and describes the ability to resolve the spectral lines which are very close together. The larger the finesse of an FPI, the higher the resolution. The instrumental finesse F is determined by the individual finesse of the degrees of reflection F_R and the finesse F_F of the smoothness of the mirror plates. If an FPI is operated as a spectral device, in addition to the instrumental finesse the characteristics of the collecting optics which follow the FPI must be taken into consideration. The useful finesse F_N contains in addition the finesse of the aperture partition F_P and the refraction finesse F_D . This can be calculated as follows:

$$\frac{1}{F_N^2} = \frac{1}{F^2} + \frac{1}{F_P^2} + \frac{1}{F_D^2} = \frac{1}{F_R^2} + \frac{1}{F_F^2} + \frac{1}{F_P^2} + \frac{1}{F_D^2} \quad (\text{B4.5})$$

The equation clearly shows that the useful total finesse F_N worsens and the values decrease compared to the apparatus constants F . As a result, the collecting optics following the FPI should be subjected to an optimization to keep the useful finesse F_N as close as possible to the value of the instrumental finesse F .

B4.3.3 The Free Spectral Range

During movement of the FPI mirror plates, that is when the distance d between them is varied, the various orders of interference of the wavelength under observation move across the detection apparatus, for example across the aperture partition in front of the detector in Fig B4.2. The free spectral range $\Delta\lambda_F$ of the FPI describes the wavelength interval in which light is represented under the same order. It is given by

$$\Delta\lambda_F = \frac{\lambda_0^2}{2nd} \quad (\text{B4.6})$$

The free spectral range of the FPI can therefore be influenced by the variation of the distance between the mirror plates d . In order to minimize the free spectral range, the mirror plates have to be far apart. But on the other hand, the useful total finesse F_N decreases with increasing distance [B4.1]. The resolution finally approaches a minimum asymmetrically. It is already close to this value in the case of nitrogen (N_1) at a distance of approximately

3mm [B4.2]. The free spectral range can be determined experimentally by measuring two orders of a strictly monochromatic spectral line, for example of a laser.

B4.4 Doppler Shift and Heavy Particle Speed

The Doppler effect was discovered by Christian Doppler in 1843 while investigating the propagation of sound. He found out that the frequency of a sound changes when a relative movement takes place between the acoustic source and the sound receiver.

This effect can also be applied to optics. If a light emitting medium, for example a plasma, is moving with a speed v and the emitted light is observed by a stationary receiver under an angle α to the propagating medium, the following equation is valid between the wavelength λ measured by the receiver and the actual emitted wavelength λ_0 :

$$\frac{\lambda}{\lambda_0} = \frac{\sqrt{1 - \frac{v^2}{c^2}}}{1 - \frac{v}{c} \cos \alpha} \quad (\text{B4.8})$$

Here c represents the speed of light and α is the angle between the normal to the wave vector of the spreading light and the speed v of the emitting particle. For plasma wind tunnel applications α indicates the angle between the optical axis of the FPI and the flow vector of the plasma stream (see Fig. B4.4). Because v is generally very small compared to c , the root in the equation above can be set at approximately 1. If the denominator in the equation above is developed in a binomic row, while neglecting the term to the second and higher orders the result is finally the following equation for the Doppler shift $\Delta\lambda_D$:

$$\Delta\lambda_D = \lambda - \lambda_0 = \lambda_0 \frac{v}{c} \cos \alpha \quad (\text{B4.9})$$

From this equation the plasma velocity v can be determined from the Doppler shift measurement. The chosen angle, however, must be large enough so that $\Delta\lambda_D$ is larger than the resolution $\Delta\lambda_A$ of the FPI.

B4.5 Doppler Broadening and Heavy Particle Translational Temperature

While observing a plasma volume emitting radiation from any angle, a Doppler broadening of the spectral line being observed occurs due to the random thermal movement (v_{th}) of the plasma particles. This Doppler broadening $\Delta\lambda_T$ results from the overlapping of Doppler shifts $\Delta\lambda$ for which the following is valid:

$$\Delta\lambda = \pm \lambda_0 \frac{v_{th}}{c} \quad (\text{B4.11})$$

Contrary to the speed v in Eq. B4.9, v_{th} is not a directed speed and the change in the wavelength is therefore also not dependent on the angle. Because, however, the thermal speed is a function of the translational temperature T_{tr} of the corresponding particle, the temperature T_{tr} can be determined by determining $\Delta\lambda_T$.

A purely thermal movement of the emitting particle corresponds to the distribution of the thermal speeds of a Maxwell distribution. The particle concentration dn with a thermal speed in the interval between v and $v + dv$ is given by:

$$\frac{dn}{n} = \sqrt{\frac{m}{2\pi k T_{tr}}} \exp\left(-\frac{mv^2}{2kT_{tr}}\right) dv \quad (\text{B4.12})$$

Here k is the Boltzmann constant, n is the concentration of the emitting particles and m their mean mass. If v is replaced by $d\lambda$ using Eq. (B4.11) and its derivative the result is:

$$\frac{dn}{n} = \sqrt{\frac{mc^2}{2\pi k T_{tr} \lambda_0^2}} \exp\left(-\frac{mc^2}{2kT_{tr}} \left(\frac{\Delta\lambda}{\lambda_0}\right)^2\right) d(\Delta\lambda) \quad (\text{B4.13})$$

In a so-called optically thin plasma the radiation absorption plays only a minor role and the intensities of the spectral lines being observed are proportional to the concentration of the emitting particles. In a low pressure plasma wind tunnel, an optically thin plasma can be assumed. Following Eq. (B4.13), the result for the intensity of a Doppler broadened spectral line is a distribution according to:

$$I(\Delta\lambda) = I_0 \sqrt{\frac{mc^2}{2\pi k T_{tr} \lambda_0^2}} \exp\left(-\frac{mc^2}{2kT_{tr}} \left(\frac{\Delta\lambda}{\lambda_0}\right)^2\right) \quad (\text{B4.14})$$

Here I_0 is the entire intensity of the spectral line and herewith $I(\Delta\lambda)$ the intensity at a distance of $\Delta\lambda$ to the unshifted center λ_0 . The width of the spectral line at half maximum counts as Doppler broadening. According to the equation above this is the case when the exponential term assumes the value 1/2. Therefore

$$\Delta\lambda = \sqrt{\frac{2kT_{tr} \ln 2}{mc^2}} \lambda_0 \quad (\text{B4.15})$$

is valid. Because the distribution of the spectral line is symmetric under these assumptions, the entire Doppler broadening results in $\Delta\lambda_T = 2\Delta\lambda$, and herewith for the translational temperature of the emitting particles,

$$T_{tr} = \frac{mc^2 \Delta\lambda_T^2}{8k\lambda_0^2 \cdot \ln 2} \quad (\text{B4.16})$$

is attained.

B4.6 Experimental Set-up

Two experimental set-ups are in use at the IRS for the Fabry-Perot interferometry. The first experimental set-up is completely outside the vacuum tanks and can be applied to every plasma wind tunnel in operation. The second experimental set-up uses fiber optics for sampling and monitoring the plasma emission on the FPI. For the first set-up, shown in Fig. B4.4, emitted light of the plasma jet is sampled with a collimating optic through an optical window. A plano-convex lens with a focal length of 2000 mm or 1500 mm is focused on the centerline of the plasma plume via a steerable mirror. Different angles of incidence are adjustable by turning the mirror and sliding the lens in order to keep the focus length. Keeping the focus in the centerline provides light intensity integration over equal volumes of the plasma plume to the right and left hand side of the centerline. The parallelized light of the plasma enters a cubic beam splitter where it is united with an unshifted and unbroadened but also parallelized light of an external lightsource, which could be a laser or also a broadened but unshifted light of the plasma plume sampled under perpendicular incidence with $\alpha=90^\circ$. Behind the beam splitter the light enters the FPI. The light which passes through the FPI is focused by a $f=84$ mm focal length lens on the pinhole entrance of a monochromator. The monochromator works as a special filter and a fast single channel photomultiplier (PMT) is used as a signal detector. The monochromator is necessary to prevent stray light from entering the PMT which transforms the light intensity into a voltage signal to be detected with a storage oscilloscope.

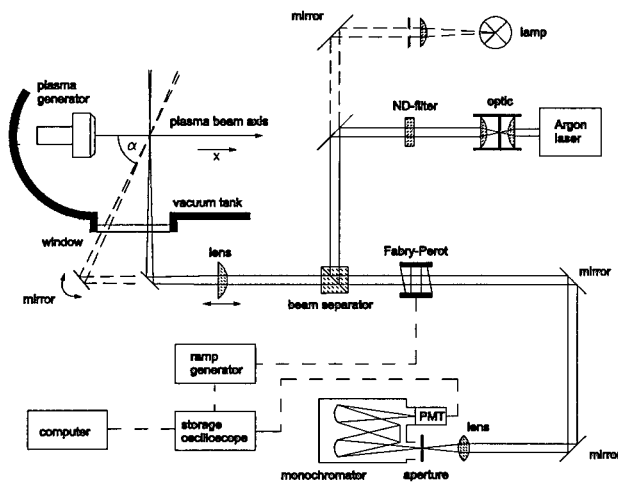


Fig. B4.4: Experimental set-up of the Fabry-Perot interferometer

The modified second experimental set-up is shown in Fig. B4.5. It provides easy access to the light emitted by the plasma plume without intensive calibration of the optical path to the FPI. Moreover, with this set-up there is no longer a limitation in the observation angle due to the window locations. Two fiber optics can be mounted on the positioning system in the plasma wind tunnel. The optical axes of both optics are

orientated under a fixed angle of $\alpha=45^\circ$. The focus of both optics is exactly at the same position in the plasma beam and can be moved to every position. Since one of the optics will always be mounted perpendicular to the plasma beam axis, the observation angle α is always 45° . A third fiber optic provides the possibility to feed laser light into the FPI for calibration purposes. Each of the three fiber optics can be plugged into an optical system which parallelizes and widens the light beam coming out of a fiber optic.

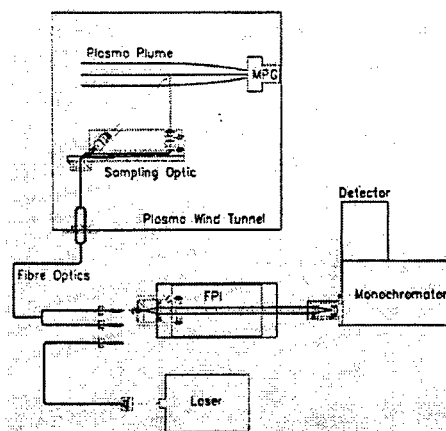


Fig. B4.5: Schematic of the experimental set-up using fiber optics

B4.7 Measurement Results

To examine the Doppler effects, one has to choose an adequate spectral line emitted by the plasma. Taking an emission spectra with the FPI experimental set-up or with emission spectroscopy (see Fig. B2.13), strong lines can be identified. Furthermore, to achieve high resolution (see eq. B4.6), longer wavelengths are preferred. One of the strongest emission lines rises out of the transition of atomic nitrogen at $\lambda_0=746.83$ nm.

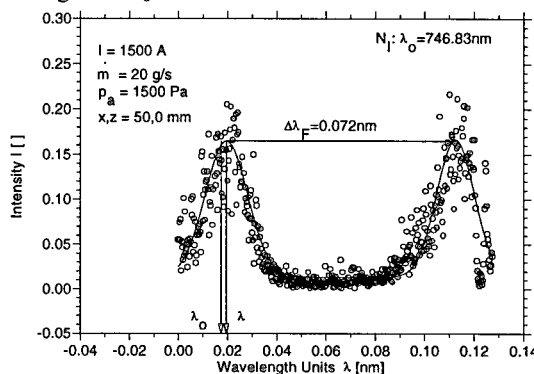


Fig. B4.6: Doppler shifted N_1 emission line of an air plasma flow

In Fig. B4.6, two orders of a typical shifted N_1 emission line are shown. The distance between the two line maximas represents the free spectral range $\Delta\lambda_F = 0.092$ nm. The plotted circles describe the signals of the photomultiplier, while the solid line is the fitted curve in order to determine the center of the full width at half maximum (FWHM). This center

represents the shifted wavelength λ . The FWHM gives the total line broadening $\Delta\lambda_G$ from which $\Delta\lambda_T$ is calculated (for line broadening see B2.1.2).

The axial distribution of the atomic nitrogen velocity in two air plasma flows of different conditions along the plasma plume center line axis can be seen in Fig. B4.7. These values are taken without Abel inversion. Due to the relatively flat velocity profile in the zone of high emission in this case, an Abel inversion does not change the result remarkably. The velocity distribution shows a "shock" behavior with decreasing velocity in the compression zone and acceleration in the expansion area for one of the test conditions.

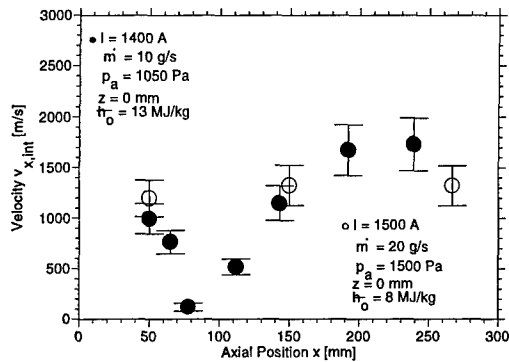


Fig. B4.7: Axial distribution of the heavy particle velocity in air plasma flows of different conditions along the plasma plume center line axis

Figure B4.8 shows the broadened profile of a N_I emission line. The instrumental broadening $\Delta\lambda_R$ is illustrated to show the effect of the thermal broadening.

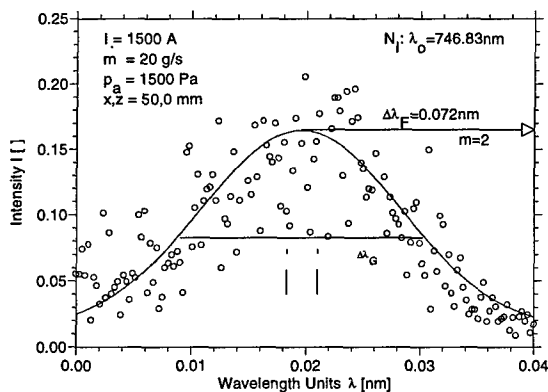


Fig. B4.8: Broadened profile of a N_I emission line of an air plasma flow

The resulting temperatures in a radial scan for different plasma condition is pictured in Fig. B4.9 again taken without an Abel inversion (see section B2.3.5).

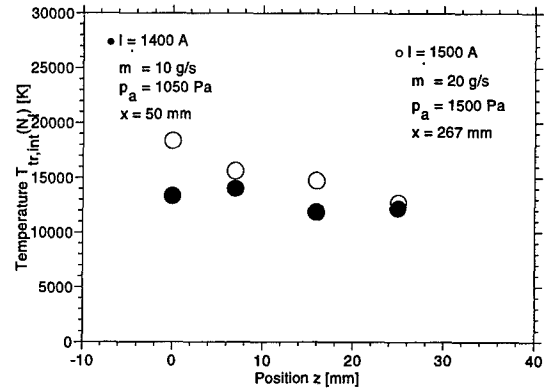


Fig. B4.9: Radial temperature distribution

References

- [B4.1] Habiger, H., "Elektrostatische Sonden und Fabry-Perot Interferometrie zur Untersuchung von lichtbogenbeheizten Plasmen für Triebwerksanwendungen und Wiedereintrittssimulation", Dissertation, Universität Stuttgart, 1994.
- [B4.2] Auweter-Kurtz M., "Manuskript zur Vorlesung Messverfahren für strömende Plasmen", Institut für Raumfahrtssysteme, Universität Stuttgart.
- [B4.3] Habiger H., Auweter-Kurtz M., "Fabry-Perot Interferometrie for the Investigation of a High Enthalpy Plasma Flow", AIAA-5-2040, 30th AIAA Thermophysics Conference, San Diego, 1995.

B5 Laser Diagnostics

Laser technics are in use in plasma wind tunnels for identifying particles, determining particle densities of atoms, molecules and electrons and for plasma velocity measurements. A big part of our knowledge of the structure of atoms or molecules could be gained by laser diagnostic measurement methods. Laser-based techniques offer the capability of performing spatially and temporally resolved measurements for a host of important parameters of the plasma jet and the boundary layer in front of heat shield materials, which can lead to an improved understanding of the material behavior. The interaction between the electromagnetic radiation of the laser and particles leads firstly to absorption and/or scattering and in consequence to emission spectra. The emission provides information about the behavior of species under investigation as explained in section B2.

B5.1 Laser Induced Fluorescence

Laser induced fluorescence is a well-established, sensitive technique for detecting population densities of atoms and molecules in specific quantum states and offers the possibility of investigating species of interest in a selective way just by choosing the appropriate wavelength.

B5.1.1 Basic Theory

With laser induced fluorescence, an upper electronic state is populated by a laser source with an emission frequency tuned to an optically allowed resonance between the electronically and rotationally vibrationally excited state and a discrete lower state, typically the electronic ground level. Fluorescence then denotes the following radiation emitted by molecules or atoms, decaying by spontaneous emission of a photon in an optically allowed transition from a higher to lower energy state. The fluorescence occurs parallel to other processes which act to de-excite the molecule, such as collisional energy transfer to other molecular states.

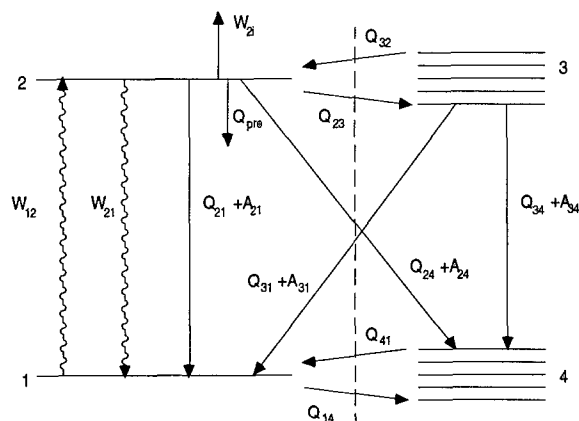


Fig. B5.1: Energy level diagram of important populating and depopulating processes

Figure B5.1 shows the excitation and de-excitation processes involved by exciting a molecule. After excitation (W_{12}), the laser-populated upper state may undergo a number of subsequent processes. Firstly, the molecule can be returned to its original state by stimulated emission (W_{21}). Secondly, absorption of an additional photon can excite still higher molecular states, including ionized levels (W_{2i}). Thirdly, the internal energy of the system can be altered in inelastic collisions with other molecules producing rotational and vibrational and also electronic energy transfer, the latter is often referred to as quenching (Q_{ij}). Fourthly, interactions between the separate atoms of the molecule, known as internal collisions, produce internal energy transfer and dissociation of the molecule. When the dissociation is produced by a change from a stable to a repulsive electronic arrangement in the molecule, it is called predissociation (Q_{pre}). Finally, there is the fluorescence signal (A_{21}) of the originally populated state and nearby states, indirectly populated through collisions [B5.1]. This signal can be captured with a photodetector and can be related to specific properties of the absorbing species through modeling of these state-to-state transfer processes. As the fluorescence is a function of the upper states population density, this requires solving the state dependent population dynamics. While quantum-mechanical density-matrix descriptions of the interactions involved in LIF are available, most treatments of LIF are based on a semi-classical rate

equation analysis [B5.2]. The rate equations are conceptually and mathematically more traceable than the quantum approach, but fail to include possible coherence effects. Generally, the validity of the rate equation analysis holds true for laser pulses which rise slowly compared to the characteristic collision time. The time dependent population $N(t)$ of a specific energy level j among a set of other levels i can be modeled with the set of rate equations, given by:

$$\frac{dN_j(t)}{dt} = \sum_{i \neq j} (N_i(t)Z_{ij}) - N_j(t) \sum_{i \neq j} Z_{ji} \quad (B5.1)$$

The first summation represents events which populate j while the second denotes loss processes. The total rate coefficient for all events transferring molecules from level i to j is Z_{ij} (s^{-1}). A number of distinct rate coefficients are included in this overall coefficient: the collisional transfer coefficient Q_{ij} (s^{-1}), encompassing both intermolecular and internal collisions, the Einstein coefficient A_{ij} (s^{-1}) for spontaneous emission and the coefficient for laser stimulated processes W_{ij} (s^{-1}). For single photon laser stimulated absorption or emission, $W_{ij} = B_{ij}I_\nu$, where B_{ij} ($cm^2 J^{-1} Hz$) is the Einstein B coefficient and I_ν is the laser spectral intensity. Applying equation (B5.1) for the energy levels involved gives a system of differential equations. The equations depend on the excitation and detection scheme used for a specific molecule or atom and have to be solved taking into consideration the special properties of the quantum mechanical behavior of the particle. For a simple two level model, where only the ground (index 1) and the excited state (index 2) are taken into account, the system of differential equations becomes:

$$\frac{dN_1}{dt} = -N_1 W_{12} + N_2 (W_{21} + A_{21} + Q_{21}) \quad (B5.2)$$

$$\frac{dN_2}{dt} = N_1 W_{12} - N_2 (W_{21} + A_{21} + Q_{21} + Q_{pre} + W_{2i}) \quad (B5.3)$$

Assuming that predissociation Q_{pre} and photoionization W_{2i} can be neglected and the population of the excited state prior to the laser excitation is negligible as well, the total population in the system is constant and for moderate temperatures in good approximation equal to the initial population of the ground state N_1^0 prior to laser excitation. This population can be calculated with the Boltzmann expression, according to equation (B2.35). The lower index of N_1^0 accounts for the state and the upper index indicates $t=0$, i.e. prior to the laser pulse, such that:

$$N_1 + N_2 = \text{constant} = N_1^0 \quad (B5.4)$$

The time dependent population for the excited state can then be written as:

$$N_2(t) = \frac{W_{12} N_1^0}{r} (1 - e^{-rt}) \quad (B5.5)$$

where

$$r = W_{12} + W_{21} + A_{21} + Q_{21} \quad (\text{B5.6})$$

For steady state assumption, i.e. the rates of the exciting and decaying processes reach a steady state behavior, the population in the excited state is then given by:

$$N_2 = N_1^0 \frac{B_{12}}{B_{12} + B_{21}} \frac{1}{1 + \frac{I_{sat}^v}{I_v}} \quad (\text{B5.7})$$

where the saturation spectral irradiance I_{sat}^v , i.e. the laser irradiance which saturates a transition, is defined as:

$$I_{sat}^v = \frac{(A_{21} + Q_{21})c}{B_{12} + B_{21}} \quad (\text{B5.8})$$

with c as the speed of light. In the saturation regime the maximum number of molecules or atoms are in the excited state. Increasing the laser irradiance will not increase the fluorescence signal any more. At low laser excitation irradiances, i.e. $I_v \ll I_{sat}^v$, the fluorescence is said to be in the linear regime, namely linearly proportional to the input laser irradiance. For $I_v \gg I_{sat}^v$, the saturated regime is reached, where the fluorescence signal becomes independent of quenching processes and the laser irradiance. In the saturation regime, the rates of laser absorption and stimulated emission become so large that they dominate the state-to-state energy transfer into and out of the directly pumped levels. Saturation also maximizes the fluorescence signal. However, complete saturation is not easy to achieve, especially in the wings of the laser focus and during the entire duration of the laser pulse.

In the linear regime, the fluorescence signal depends on the laser irradiance. To make the measurement independent of the fluctuations of laser energy, one has to normalize the fluorescence signal to the laser irradiance. Additionally the quenching rate can be determined experimentally in the linear regime. In low pressure regimes and low laser irradiances, the quenching rate can be measured by monitoring the exponential decay rate, i.e. the time resolved decay of the excited molecules to the ground level. An excited level has a certain molecular dependent lifetime, which is described with: $\tau = 1/(A+Q)$ [B5.2]. Here, Q stands for all de-excitation processes and A again for the spontaneous emission rate. By monitoring the time decay, one can extract the de-excitation rate, as seen in Fig. B5.2.

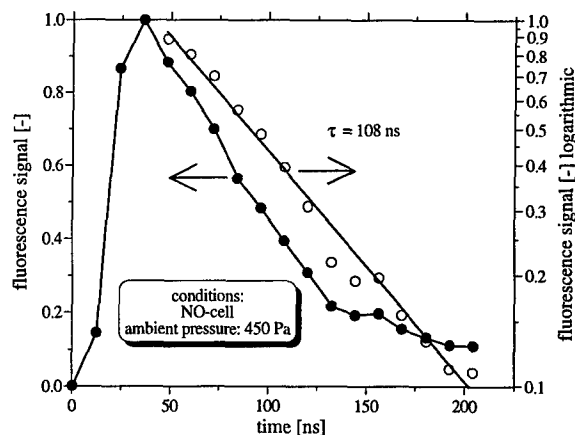


Fig. B5.2: Lifetime measurement of NO in a cold gas cell [B5.3]

B5.1.1.1 Two-Photon Excitation

As will be explained in B5.1.2.1, with modern laser equipment tunable radiation can be generated in a continuous spectral range down to about 200 nm. However, most atoms and several molecules possess absorption lines well below 200 nm. The spectral region below 200 nm is termed the vacuum ultraviolet (VUV), since radiation in this range will not propagate through air due to atmospheric absorption, initially by molecular oxygen. Transitions below 200 nm can be accessed and excited via the simultaneous absorption of two photons (or more). Most of the excitation schemes involve single wavelength multi-photon excitation and are of course favourable since one needs only one laser. An example of the excitation scheme of atomic nitrogen is illustrated in Fig B5.3. The two-photon excitation rate constant per molecule may be written as:

$$W_{12} = \frac{\alpha_{12} I^2}{h\nu} \quad (\text{B5.9})$$

where α_{12} is the two-photon absorption cross section from state 1 (ground state) to state 2 (excited state). The two-photon cross sections are small which means that stimulated two-photon downward transitions can be neglected for moderate laser irradiances. The fluorescence signal will depend quadratically on the laser irradiance and on the quenching rate constant as in the linear fluorescence regime.

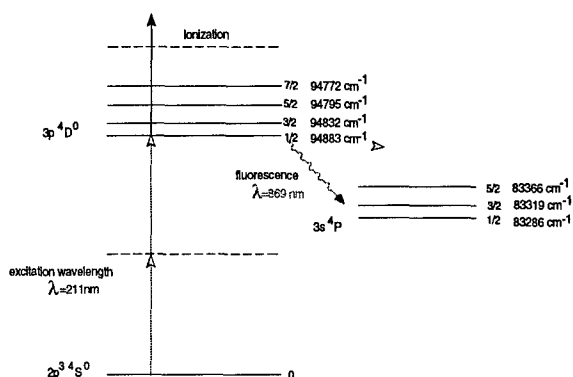


Fig. B5.3: Excitation scheme of atomic nitrogen

By absorption of a third photon, the particle can be ionized. Since this means a loss in fluorescence signal, one has to ensure that the laser energy is kept sufficiently low.

B5.1.1.2 Fluorescence Detection and Temperature Considerations

The intensity of the fluorescence signal is proportional to the number density N_2 in the excited state and can in general be described with:

$$S = C_{KAL} h\nu N_2 A_{21} \quad (B5.10)$$

The calibration constant C_{KAL} has to be determined for the experimental set-up used and includes the transmission of the fluorescence through windows, filters, lenses and influences of the excitation and collection volume and the electronics in the data capturing process. The term $h\nu$ describes the photon energy of the emitted photons. N_2 is determined with the rate equation model. The initial population prior to the laser pulse N_1^0 of the rotational quantum state is related to the total number density and temperature via the Boltzmann expression, see equation (B2.35). Therefore, the temperature has to be determined first. For molecules the temperatures which describe the population distribution in different rotational, vibrational and electronic levels are called the rotational, vibrational and electronic temperature, as explained in B2.1.4 and B2.2.4. Mostly one only has access to the rotational temperature which is coupled with the heavy particle temperature in plasma applications. If the temperature is high enough to populate different vibronic levels, the vibrational temperature can be determined with the so-called two line thermometry. The best access to the rotational temperature is given by doing an excitation scan over the rotational states in the ground state [B5.2]. The laser wavelength is changed continuously over the range of the rotational absorption lines of the electronic transition of the particle. If the fluorescence F_J of each transition is monitored and normalized by the degeneracy $(2J+1)$, fluorescence quantum yield $(A/(A+Q))$ and line strength B_{12} , and plotted in semi-log fashion against the rotational energy $hcB_v J(J+1)$, like

$$\ln\left(\frac{F_J \cdot B_{12} / (A / (A+Q))}{2J+1}\right) = -B_v J(J+1) \frac{hc}{kT} + const. \quad (B5.11)$$

a straight line is obtained with negative slope whose magnitude equals $(kT)^{-1}$ thus yielding the rotational temperature. If the exact temperature cannot be determined but the approximate value \bar{T} is known, one can use a transition whose quantum number J^* is least sensitive to temperature changes. Therefore, setting the derivative of the Boltzmann expression over the temperature to zero leads to:

$$J^{*2} + J^* - \left(\frac{k}{hcB_v}\right) \bar{T} = 0. \quad (B5.12)$$

B5.1.1.3 Calibration

In order to determine the number density from a LIF experiment, values for a number of parameters related to the employed excitation and detecting scheme are required. The exciting wavelength and the spectral width of the laser beam has to be determined as well as the laser pulse length and the laser pulse energy. The light collection efficiency, the collection solid angle and the sample volume have to be evaluated. In the linear fluorescence regime the fluorescence quantum yield has to be measured to account for quenching losses. The influence of the electronic data acquisition system has to be identified.

Calibrations are often performed by employing a gas cell filled with a known density and temperature of the examined gas in the observation volume and leaving any other part of the experimental set-up unchanged. Building the ratio with equation (B5.10) for the calibration measurement and the experiment (N_2 (Eq. B5.7) and the rotational and vibrational temperatures in the Boltzmann distribution equations (B2.35) are different), lead directly to the number density of the species. However, this procedure requires a stable molecule or atom, for instance nitric oxide. Since LIF is a method used mainly for monitoring reactive species (N, O, SiO, OH etc.) other calibration techniques have to be used. There are different methods established to approach the calibration process, like Rayleigh scattering [B5.4], absorption measurements [B5.5] and Raman scattering [B5.6]. Every process has advantages for certain applications. The calibration procedures used at the IRS will be discussed in B5.1.2.

B5.1.2 Research at the IRS

The possibilities offered by LIF are tremendous. LIF can contribute solutions in almost all plasma relevant questions. It can help to identify the species involved in a material erosion process, provide data about the catalytic of a material and monitor plasma parameters. However, high operating expenditure is demanded. It is necessary to control and synchronize the laser with the monochromator, the data capturing electronics, e.g. the gated integrator and boxcar averager, the digital storage oscilloscope, the energy meter and the computer. Special care and further analysis has to be done when relating the fluorescence signal to absolute number densities by calibrating the detection optics. And finally the alignment of the optical paths are crucial for the quality and the precision of an experiment. The research so far has focused on determining number densities as well as on the characterization of erosion mechanisms of thermal protection materials. For the characterization of the plasma flow, the atomic densities of nitrogen (N) and oxygen (O) are of special interest. These quantities are also monitored together with nitric oxide in the boundary layer of a probe material for the investigation of the material

catalycity. The boundary between active and passive oxidation of silicon carbide (SiC) can be determined by exciting silicon oxide (SiO) molecules. Furthermore, the evaluation of the relative density of silicon oxide, carbon oxide and nitric oxide (absolute measurements planned as well) in front of a material probe will help us to better understand the erosion mechanism.

B5.1.2.1 Experimental Considerations and Experimental Set-up

In general, the fluorescence wavelength is different from that of the incident excitation and occurs primarily, but not exclusively, at longer wavelengths. The photons emitted from the excited molecules radiate undirected. Therefore, the fluorescence signal can be detected under any angle, but it is advantageous to detect the fluorescence perpendicular to the propagation of the laser beam and perpendicular to the plasma flow under investigation because this provides the smallest observation volume and a non-Doppler shifted absorption line (see Fig. B5.4).

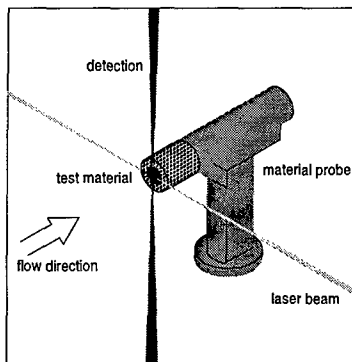


Fig. B5.4: Principle of excitation and detection scheme

There are two ways of setting up the experimental approach. In a single point measurement, the laser is focused into the observation area and the fluorescence is detected with a one-dimensional detector, generally a photomultiplier tube (PMT). The selection of the fluorescence wavelength can be achieved either with a monochromator or with an interference filter. The output signal of the PMT is then captured with a so-called gated integrator and boxcar averager. This device is designed to recover fast analog signals from noisy backgrounds. It consists of a gate generator, a fast gated integrator and exponential averaging circuitry. The gate generator provides an adjustable delay from a few nanoseconds to 100 milliseconds to an input trigger pulse before it generates a continuously adjustable gate of 2 ns to 15 μ s. The fast gated integrator integrates the input signal during the gate. Figure B5.5 shows an example of setting the sampling gate of the boxcar averager (data acquisition device) in respect to the fluorescence signal. The position of the sampling gate is particularly important for density or

temperature measurements as will be discussed in section B5.1.2.2.

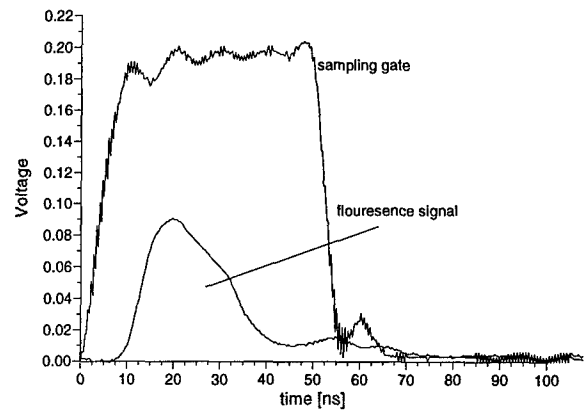


Fig. B5.5: Example of setting a sampling gate

For a planar LIF (PLIF) measurement, the excitation laser beam is optically spread into a thin sheet, and the resulting fluorescence from the illuminated plane is imaged through an appropriate filter onto a two-dimensional detector.

At the IRS, a laser system is available to experimentally examine plasma flows and boundary layers within the plasma wind tunnels. The laser system consists of an excimer laser Lambda Physik COMPex201, a dye laser Lambda Physik SCANmate 2E and a second harmonic generator to double the frequency. The excimer laser is filled with XeCl and emits radiation at around 308 nm. This laser light is passed to the dye laser to pump the circulating dye inside the oscillator / preamplifier and main amplifier cells of the dye laser. The oscillator determines the quality of radiation and is therefore the most important and sensitive part of the dye laser. It basically consists of a grating for wavelength selection and an etalon for ultra-narrow line width operation. If needed, the etalon can be moved in the laser beam path to improve the laser line width from 0.15 cm^{-1} without etalon to 0.03 cm^{-1} with etalon.

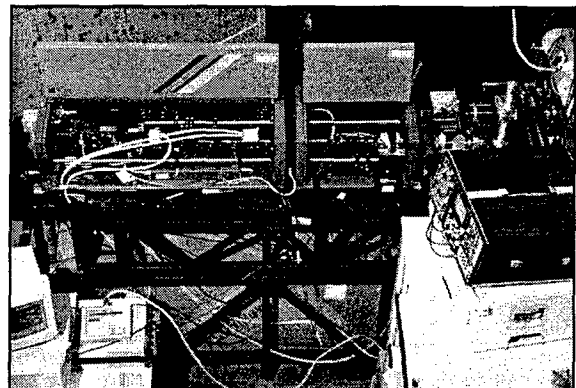


Fig. B5.6: Excimer and dye laser system with the frequency doubling unit at PWK2

This becomes particularly important for determining atomic or molecular velocities with Doppler shift measurements (see also section B4.4). Since many absorption lines of atoms or molecules are in the C-UV (C-ultraviolet, 180-280 nm) or even VUV (vacuum ultraviolet, below 180 nm) region and the different dyes cover a spectral range of 320-1050 nm, a frequency doubling unit was installed. It is a Beta Barium Borat (BBO) crystal followed by a quartz plate to compensate for the beam shift. In order to separate the UV and the fundamental beam with low losses and without beam displacement, four quartz Pellin-Broca prisms, set nearly to Brewster's angle (angle for which the transmission of vertically polarized light is the highest), are placed in the beam path. To provide the specific excitation wavelengths for the species of interest, different dyes, dissolved in Methanol, were used as shown in Table B5.1.

Dye	For excitation of	Peak [nm]	Range [nm]	Efficiency [%]
Stilbene 3	N	425	412-443	9
Coumarin 47	NO O	456	440-484	18
Coumarin 102	SiO	480	460-519	18

Table B5.1: Characteristic values for the dyes used with an XeCl-excimer laser excitation source
With this laser system, it is possible to obtain wavelengths from around 200 nanometers up to 1050 nanometers by choosing the desired dye. Typical maximum laser energy outputs after the frequency doubling unit are about 3-4 mJ. The laser pulse length can be monitored by using the Rayleigh signal and is about 25 ns. Rayleigh scattering is an elastic process in which there is no energy exchange between the incident photons of light and the target molecules. Thus, the scattered light is unshifted from its initial

incident frequency. This is explained in section B5.2. To make the measurement independent of the fluctuations of laser energy, one has to normalize the fluorescence signal to the laser irradiance, where the laser energy can be measured with a pyroelectric energy meter. In Fig. B5.7 the experimental set-up and the assignment of the axes are shown. The x-axis is the plasma beam axis, the y-axis is perpendicular in the horizontal, i.e. along the laser beam path and the z-axis is perpendicular in the vertical, here along the path of the collection optics. Fluorescence is detected perpendicular to the laser and the flow direction. It is monitored with a telescope consisting of two planoconvex fused silica lenses three inches in diameter and detected using photomultiplier tubes with a very short rise and transition time (usually less than 2 ns). The output current of the photomultiplier tube is terminated with a 50 Ohm load and passes through a preamplifier before it is sampled by a boxcar averager and transmitted via the GPIB interface to the computer for data processing.

B5.1.2.2 Examination of Nitric Oxide

The formation of NO is a result of the recombination of N and O atoms on surfaces and contributes to the heat flux to which the material is exposed. This formation strongly depends on the material's catalyticity which has to be minimized for thermal protection application. An attempt has been made to examine NO in the PWK. The γ -band of NO is used to excite molecules from the ground state.

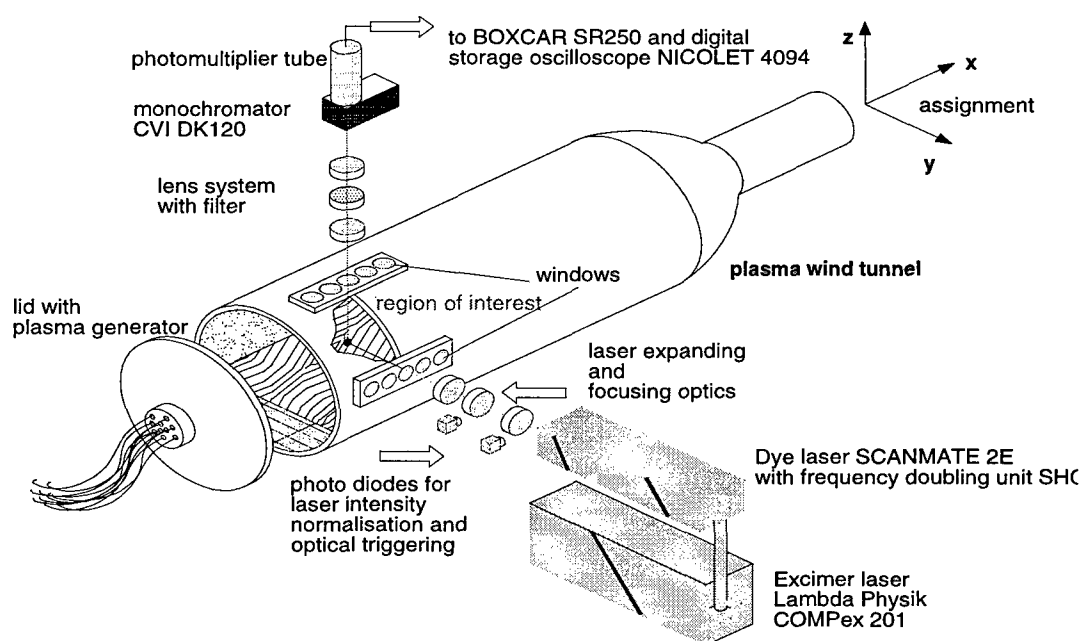


Fig. B5.7: Experimental set-up at PWK2

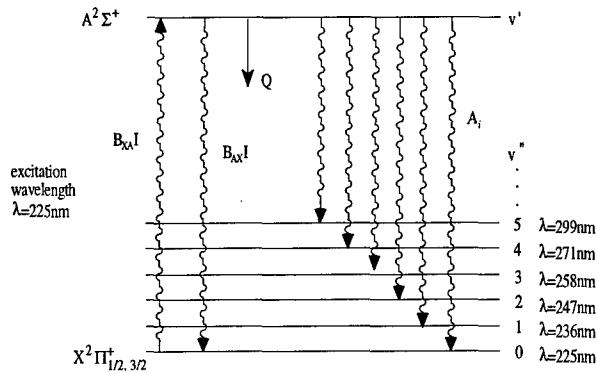


Fig. B5.8: Energy level diagram for nitric oxide

Figure B5.8 shows the radiation and collision processes involved. The monochromator was set at 260 nm with an exit slit of 4 mm, resulting in a detected range of 234 to 286 nm, so that fluorescence from (0,1) to (0,4) vibrational bands could be detected and scattered laser light at 225 nm is rejected. The sampling gate width was set to 200 ns to sample all the fluorescence for an acceptable signal-to-noise (S/N) ratio. Therefore, caution must be taken when calculating rotational temperatures. Rensberger et al. [B5.7] described the requirements for obtaining accurate temperatures. They proposed using small gate widths to account for rotational energy transfer. A gate width, which collects fluorescence over the exponential decay, leads to a measured temperature which is too high because excited states with high rotational quantum numbers can have a longer lifetime than states with low quantum numbers. For these PWK conditions it was necessary to detect any fluorescence signal in order to get a signal high enough to be used for data processing. The occurrence of NO in a plasma jet decreases with increasing enthalpy [B5.8, B5.25]. For operating conditions at high enthalpies of around 30 MJ/kg and pressures of approximately 300 Pa, as is of importance for the qualification of winged vehicles [B5.9], there is no LIF-detectable amount of NO concentration in the plasma beam axis of the free stream. Under these arc heater conditions, the mole fraction of NO is numerically estimated to be about 10^{-5} [B5.10]. But the situation is very different in front of a material probe positioned in the same plasma jet due to the material catalycity. Figure B5.9 shows an excitation scan with an arc current of 1200 A at an axial distance of 467 mm and 1 mm in front of a water-cooled copper probe. The scan is performed at laser irradiances in the linear fluorescence regime and the fluorescence is normalized to laser intensity. Fifty samples have been averaged to achieve a statistical result. The data are normalized from the overlapping $Q_2(35)$ and $R_1(28)$ lines and background subtracted. The line assignment is done by comparing the experimentally obtained spectra with a simulated spectra of LIFBASE [B5.11]. To acquire the fluorescence, the collection volume had to be made comparably large to get enough of a signal.

Additionally, precautions have to be taken for the reabsorption of fluorescence since the occurrence of NO in the outer region of the plasma beam is comparably high.

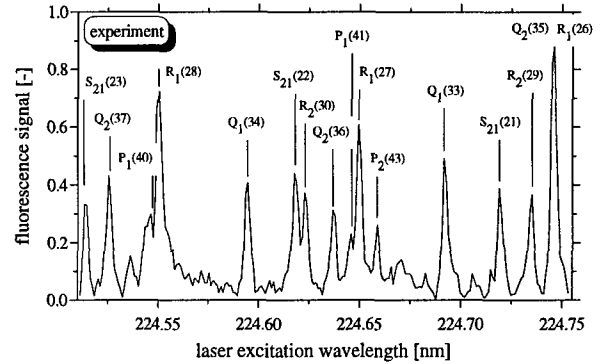


Fig. B5.9: Excitation scans of NO 1 mm in front of a water-cooled copper probe, placed at an axial distance of $x=467$ mm in PWK with an arc current of 1200A and rotational assignment

In Fig. B5.10 one can see that NO is produced as a result of a water-cooled copper probe placed in the plasma beam axis. It is apparent that the background noise at the beam axis is high compared to the fluorescence signal. The data are normalized to the fluorescence signal taken at 1 mm to the probe surface. There is no fluorescence signal in the free stream plasma flow. At a distance of 6 mm from the collected volume to the probe surface there is a detectable amount of NO, which increases as the distance to the probe decreases. Taking into account this fact together with the low rotational temperatures of ca. 1200 K, leads to the assumption that NO is produced by catalytic interactions with the probe surface and not because of adequate conditions in the boundary layer.

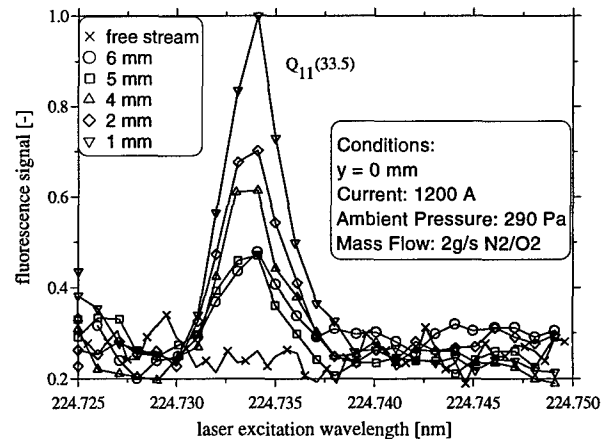


Fig. B5.10: Integrated NO fluorescence at various distances to a water-cooled copper probe at an axial distance of $x=467$ mm

Bismuth is known to have low catalycity. Therefore experiments with a bismuth coated surface were performed but signal levels are too weak for data processing. To get a profile for the y-axis, measurements were carried out in one direction of the y-axis from the center to the outer region, assuming rotational

symmetry. The spatial scan is seen in Fig. B5.11 which was taken with a cooled copper probe placed at $y=0$.

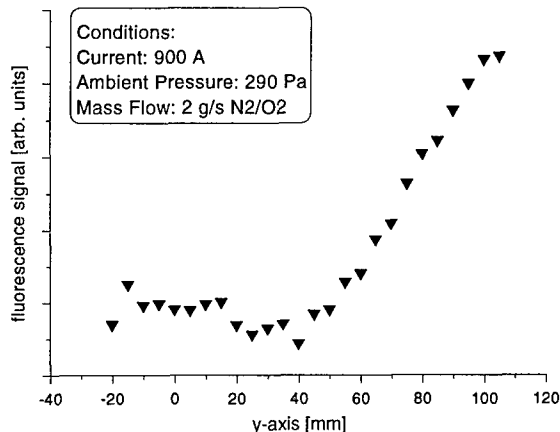


Fig. B5.11: Radial profile of fluorescence signal of NO at an axial distance of $x=467$ mm

The qualitative radial distribution of NO molecules is in agreement with mass spectroscopy measurements. The observation window of the PWK has a diameter of 100 mm. Therefore, the signal with a radial distance of more than $y=20$ mm is not collected correctly perpendicular to the laser beam. But the effect on the collection volume is negligible since the angle varies only by about 1 to 4 degrees. To suppress the influence of the temperature, a ground rotational state which is least sensitive to an estimated rotational temperature is chosen to excite NO molecules. It was calculated from evaluating the derivative of the Boltzmann expression with respect to temperature and equating it to zero according to equation (B5.12). The molecular data were taken from LIFBASE [B5.11]. There is a very small amount of NO in the plasma beam axis compared to the outer region of the plasma beam. The heavy particle temperature in the center of the free stream at $x = 467$ mm is about 6000 K [B5.26] which is too high for NO to occur. In the satellite region (at $y=80$ mm) there is a temperature of about 2500 K and therefore good conditions for NO stability. The increasing NO occurrence in front of a water-cooled copper probe agrees with the numerical prediction using the SINA Code [B5.10]. The probe is placed at $x = 467$ mm (Fig. B5.12). It is evident that the amount of NO increases in front of a probe and the heavy particle temperature which is coupled with the rotational temperature decreases. Absolute measurements could not be performed yet. At the IRS the calibration for NO will be done with a heated dynamic gas cell which is currently under construction. Heating the NO gas of known density is necessary in order to populate higher rotational states and excite a rotational transition with the same quantum number as used in the experiment.

B5.1.2.3 Examination of Silicon Oxide

Ceramics and composites based on silicon carbide (SiC) are prime candidates for reusable thermal protection materials. The erosion behavior of thermal protection materials is still not known in detail. The reactions, which lead to the reduction of the thermal protection material, involve a host of chemical combination products and depend on pressure, temperature, plasma velocity and plasma components. Of great importance is the oxidation behavior of the material. The oxidation regime is divided into a passive and an active oxidation regime. In a situation where the oxidant pressure is so low that a protective layer of SiO_2 cannot be formed, SiO (gaseous) forms and leads to rapid consumption of the SiC and SiO_2 if available. This behavior is termed "active oxidation". The other mechanism which occurs at higher oxidant pressures is the formation of SiO_2 (solid) and immediate reduction to SiO (gaseous) by reducing gases in the environment. At those oxidant pressures where SiO_2 volatility is negligible, typical "passive oxidation" behavior is observed [B5.13, B5.14]. The monitoring of SiO formation while changing plasma parameters can be used to evaluate the conditions for the passive-active transition. The basic spectroscopic data are calculated numerically [B5.15, B5.16].

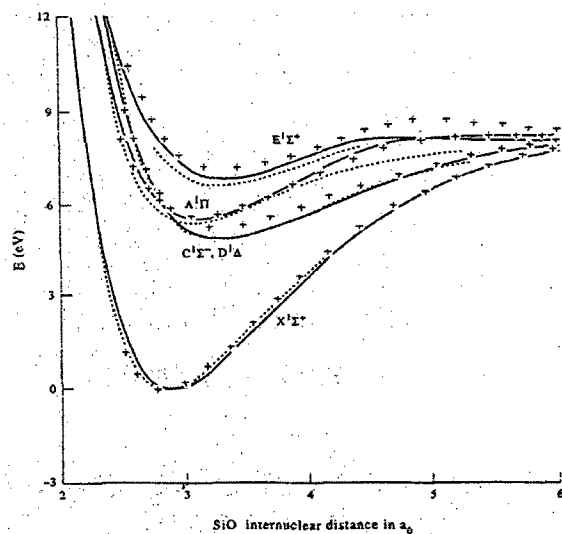


Fig. B5.13: Energy levels of SiO [B5.15]

Experimental data are available from the authors Heynes [B5.17] and Park [B5.18]. The known electronic states are shown in Fig. B5.13. The ground level is given with $X^1\Sigma^+$. The data, like the Franck-Condon-Factors and lifetimes, are only available for the electronically first excited level $A^1\Pi$ and the level $E^1\Sigma^+$. One can easily see that the $E^1\Sigma^+ \leftarrow X^1\Sigma^+$ transition can only be excited with a two-photon-absorption because the symmetry of the molecule does not change. The number of excited atoms or molecules are due to the probability of absorbing two photons almost instantaneously, less than with one photon absorption. Additionally the one-photon-excitation wavelength would be very close to the VUV (around 189 nm). Although this transition

offers a transition probability twice as high as the $A^1\Pi \leftarrow X^1\Sigma^+$ transition, it is advantageous to use the $A^1\Pi \leftarrow X^1\Sigma^+$ transition at around 235 nm because of the excitation wavelength and the one-photon absorption process. In order to identify SiO, an excitation scan (Fig. B5.14) is performed in front of the surface of a Si-probe material in an argon/oxygen plasma at an axial distance of 330 mm. The total pressure in front of the probe was 42 Pa and the front surface of the probe had a temperature of 1315°C. The fluorescence signal of the (0,4) vibrational band and parts of the (0,3) and (0,5) bands were monitored using an interference filter with 260 ± 10 nm. Figure B5.15 shows the reaction zone of SiO in front of a silicon surface. Apparently with these plasma conditions, SiO is produced at the surface or at least close to the surface. It is planned to examine the behavior with the two-dimensional detection of the reaction zone. PLIF will be used to obtain relative concentrations of SiO, as well as from other erosion components (CO, CN, NO, SiN).

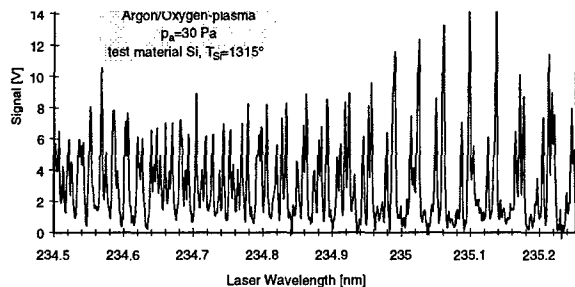


Fig. B5.14: Excitation spectra of SiO

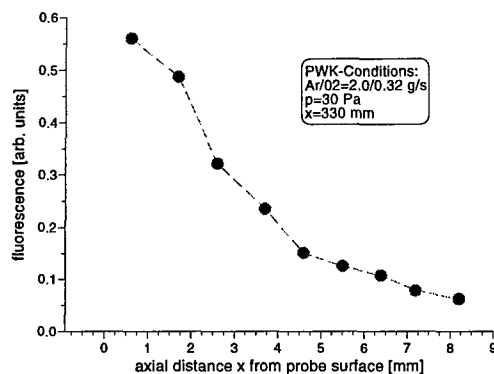


Fig. B5.15: Reaction zone of SiO in front of a silicon wafer

In a second step, the materials Si, SiO₂ and SiC were used and the surface temperatures were varied. The fluorescence signal was observed at a distance of 1 mm to the surface. With SiO₂ material, SiO is produced at a temperature of 1200°C whereas with SiC the onset takes place at 1500°C. An interesting result is seen with an SiC probe. Above 1750°C the process apparently seems to proceed with other dominant reactions. This will be examined in the near future.

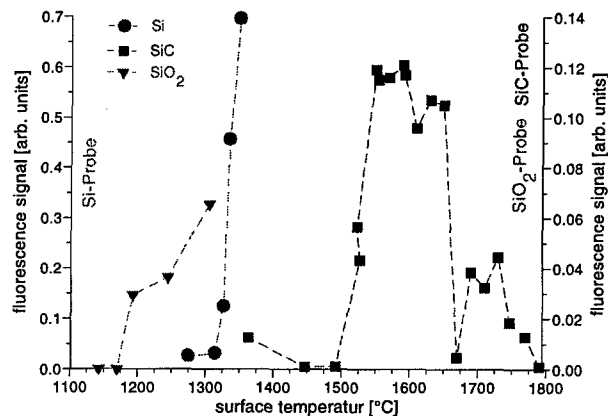


Fig. B5.16: Temperature dependent erosion mechanisms of SiO for different materials at a total pressure of 42 Pa

B5.1.2.4 Examination of Atomic Oxygen and Atomic Nitrogen

There is great interest in determining atomic species concentration. This can contribute to gaining knowledge about plasma conditions created by the different generators and to evaluate phenomena of catalycity and erosion processes. The difficulties of atomic density measurement arise from calibration procedures. Since there are no reliable sources of atomic oxygen or atomic nitrogen production, it is very difficult and very complex to calibrate the measurements, i.e. to relate the fluorescence signal to a certain density. However, LIF can be used to determine N- and O-concentrations. The procedure follows experiments of Bamford et al. [B5.19], who developed an approach by carefully measuring all factors involved. As described in section B5.1.1.3, the spatial (dimension of the focus) and temporal spread (laser pulse length) have to be accounted for and the characteristics of the laser beam, the detection optics and electronics have to be calibrated. Furthermore, the fluorescence quantum yield has to be determined and for atomic nitrogen polarization (polarization explained in section B5.2) effects cannot be neglected. With these assumptions and by computing the system of differential equations, the number density can be calculated with:

$$N_0 = \left[4\pi^2 \left(\frac{S}{E^2} \right) \omega_v \omega_h \frac{(h\nu)^2}{\alpha} \phi_f \cdot D \cdot \int_{-\infty}^{\infty} F^2(t'') dt'' \right] \quad (\text{B5.13})$$

S is the measured voltage of the photomultiplier, E is the energy of a laser pulse, ω_v and ω_h are the focus sizes in vertical and horizontal directions, $h\nu$ is the photon energy of the laser beam, α is the cross section for a two-photon absorption, $\phi_f = A/(A+Q)$ is the fluorescence yield and D is the calibration constant obtained with Raman spectroscopy. The constant includes the effective length of the light collection system, the solid angle of the collection lens, the transmission through

windows and filters, the quantum efficiency of the detector and the electrical conditions.

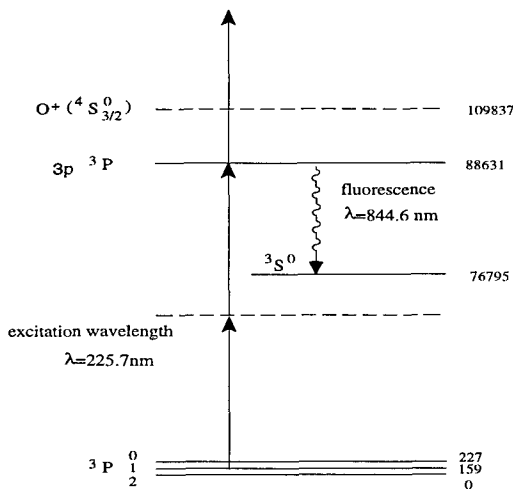


Fig. B5.17: Excitation scheme of atomic oxygen

The function $F(t)$ accounts for the temporal profile of the laser beam. The fluorescence yield can be measured by monitoring the fluorescence decay curve, as explained in section B5.1.1. The excitation processes for atomic nitrogen and atomic oxygen are shown in Figs. B5.3 and B5.17, respectively. A spectra is shown in Fig. B5.18. The atomic oxygen was produced in a microwave discharge at low pressure. The three absorption lines arise out of the fine structure splitting, as can also be seen in the schematic excitation in Fig. B5.17.

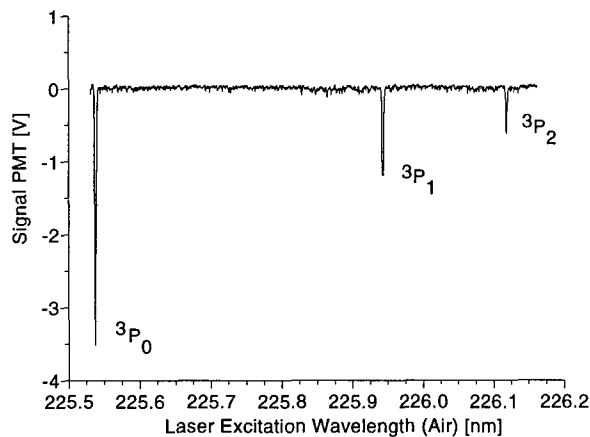


Fig. B5.18: Excitation scan over the fine structure splitting of atomic oxygen

As mentioned before, the requirements for an absolute measurement have to be satisfied. Raman scattering on H_2 is used to absolutely calibrate the photon collection efficiency of the detection optics [B5.6]. This calibration procedure has advantages over the other methods, mentioned in section B5.1.1.3. The collection efficiency can be calibrated for the exact laser focal volume used in the experiment at exactly the fluorescence wavelength. The influence of stray light from the laser beam (e.g. plays a role in calibrating with Rayleigh scattering technics) is greatly suppressed since the transition used is shifted at 4155 cm^{-1} to a higher wavelength than

the incident laser wavelength. This Raman shift in H_2 at 4155 cm^{-1} is the largest of any molecular system and its spectroscopy is well known.

Furthermore, PWK2 can be operated with a mixture of Ar/O_2 and the inductive plasma generator PWK3 can be operated with pure oxygen. In the past an oxygen sensor was developed [B5.20 and see section A6] to monitor the partial pressure of oxygen. The difficulty is that the sensor cannot distinguish between atomic and molecular oxygen. Adjusting the PWK conditions in a manner that it can be assumed that all the oxygen is dissociated but not ionized offers a possibility to compare the results of both measurement methods.

B5.2 Raman Spectroscopy

Raman scattering is the inelastic scattering of light from molecules and is termed rotational, vibrational or electronic, depending on the nature of the energy exchange which occurs between the incident light quanta and the molecules. Because polarization of light plays an important role in Raman spectroscopy, a short introduction to this topic is given. Optical radiation across the spectrum is in the form of transverse electromagnetic waves, that is, the directions of the oscillating electric and magnetic fields of any particular wave are perpendicular to the direction of travel and to each other. Polarization occurs when the electric field vectors for many waves in a beam assume a preferred direction rather than being randomly distributed. The electric field vector is used to describe the various states of polarization. Most incoherent sources emit rays that have electric fields with no preferred orientation and are therefore unpolarized. A beam is said to be linearly or plane polarized when all the electric field vectors are oriented in the same direction or plane of polarization. The plane of polarization is perpendicular to the direction of travel. When the plane of polarization is parallel to the plane of incidence, this is known as p-polarization. If the plane of polarization is perpendicular to the plane of incidence, this is known as s-polarization. The plane of incidence contains the direction of the incident beam and the normal to the surface. In addition to the linear polarization, circular and elliptical polarization can occur.

Raman scattering essentially occurs instantaneously within a time of 10^{-12} s or less. The molecular polarizability, α , relates the induced dipole moment, \vec{p} , to the incident electric field, i.e. $\vec{p} = \alpha \epsilon_0 \vec{E}$ and the dipole moment induced by an incident wave with frequency ν_0 is then:

$$\vec{p} = \alpha_0 \epsilon_0 \vec{E}_0 \cos(2\pi \nu_0 t) + \left(\frac{\partial \alpha}{\partial Q} \right)_0 \epsilon_0 \frac{Q_0 \vec{E}_0}{2} [\cos(2\pi t(\nu_0 - \nu)) + \cos(2\pi t(\nu_0 + \nu))] \quad (\text{B5.14})$$

with Q as the nuclear vibration coordinate. The subscript 0 stands for conditions in the equilibrium position of the atom nuclei. The first term leads to scattered radiation at the incident frequency, the Rayleigh process, while the second term leads to scattered radiation shifted from the incident wave by the characteristic frequencies of the medium, namely the Raman scattering. The radiation downshifted in frequency is termed Stokes, while that upshifted is termed anti-Stokes. The latter involves energy exchange from the molecule to the incident photon and occurs only at elevated temperatures when a sufficient excited state population exists [B5.2]. No specific laser wavelength is required and due to the quantization of the molecular energy states, the Raman spectrum resides at fixed frequency separation from the laser line and is characteristic for the molecule from which the scattering emanates. The Raman scattered signal is therefore species specific and linearly proportional to the species number density.

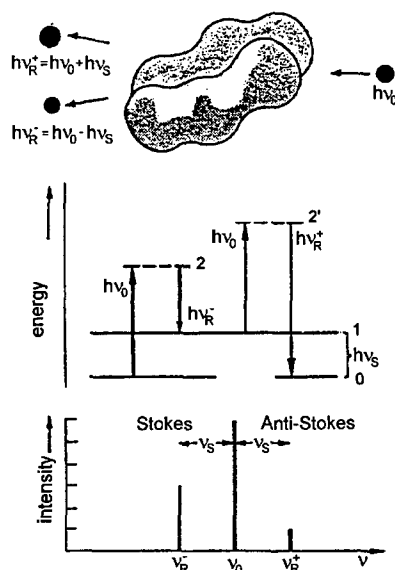


Fig. B5.19: Schematic model of Raman scattering [B5.21]

The energy model in Fig. B5.19 shows the transfer processes involved. State 0 describes the ground level, state 1 an excited vibration level. States 2 and 2' are imaginary states. The frequencies of the Raman scattering are ν_R^- and ν_R^+ . The Raman shift is described with ν_S . The ground vibrational level is more highly populated than the excited levels due to the Boltzmann expression and therefore the intensity of Stokes shifted Raman scattering is mostly higher than the anti-Stokes shifted intensity.

Important factors of Raman scattering are the depolarization ratio and the cross section. The depolarization ratio ρ is defined by the ratio of the polarization of the scattered radiation and is:

$$\rho = \frac{I_{\parallel} - I_{\perp}}{I_{\parallel} + I_{\perp}} \quad (B5.15)$$

where I_{\parallel} and I_{\perp} are the intensities of the scattered radiation with a polarization parallel or perpendicular to the polarization of the laser light. Raman scattering cross sections are necessary to determine the signal strength. In general, Raman cross sections and depolarization ratios depend on the species and are experimentally determined. Unfortunately, Raman scattering is very weak with small cross sections, thus requiring a certain number density of the species probed. In comparison with LIF, Raman requires concentration levels of 1% of the species mole fraction, whereas LIF can measure in the ppm (particle per million) range. For a small scattering solid angle, the radiant intensity I_r may be expressed as:

$$I_r = I_i n \cdot \left(\frac{\partial \sigma}{\partial \Omega} \right) \cdot \Omega l \epsilon \quad (B5.16)$$

where I_i is the incident laser intensity, n is the number density of scattering species, $\partial \sigma / \partial \Omega$ is the differential cross section, Ω the collection angle, l the sampling extend and finally ϵ as the collection efficiency which has been included to account for losses in the optical collection system. Figure B5.20 shows a rotational Raman spectrum of N_2 as an example.

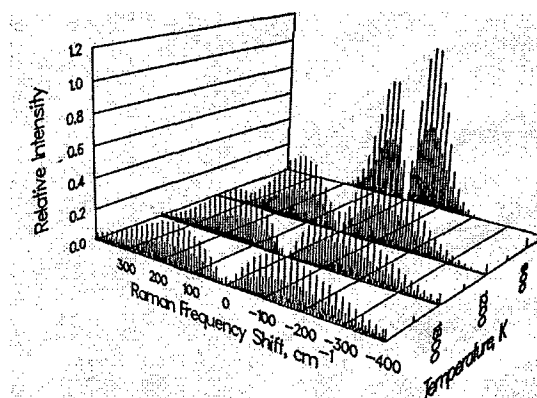


Fig. B5.20: Temperature dependence of the rotational Raman of N_2 [B5.2]

At the IRS, Raman spectroscopy is used for absolute calibration of the detection optics and electronics of the LIF experiments with Raman scattering in H_2 . The molecular densities in the MPD wind tunnels are too small to obtain a sufficient signal.

B5.3 Thomson Scattering

In recent years, the method of incoherent Thomson scattering has been applied to measure electron properties of plasma flows. When a laser beam is injected into a plasma, the laser radiation scatters non-resonantly from the free and bound electrons in the plasma. The total spectrum of the scattered light contains three main components: a Thomson scattering component which arises from scattering of free electrons, a Rayleigh scattering component which arises from incoherent scattering from the

bound electrons in the atoms and ions and a stray light component which arises from laser radiation scattering from the surfaces and windows of the chamber. The Thomson and Rayleigh components, which are both Doppler-broadened due to the motion of the scattering particles, have very different spectral widths because of the much higher thermal velocity of the electrons compared with the atoms and ions.

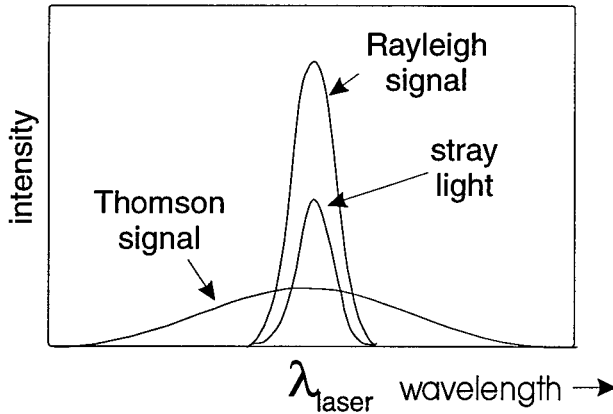


Fig. B5.21: Different components of the total scattered spectrum [B5.22]

If the entire spectrum is measured, the Thomson scattering component can be determined from wavelengths at which there is no contribution from the Rayleigh or stray components. Interpolation of the Thomson component in the central part of the spectrum then allows the Rayleigh and stray light components to be determined. Or the influence of the Rayleigh signal and the stray light are measured separately in a calibration and can then be subtracted from the measured signal in a Thomson scattering experiment. When the electron temperature is low (i.e. below approximately 50000 K), the Doppler-broadened Thomson-scattered spectrum is directly related to the velocity distribution function of the scattering electrons. When the electron velocity distribution function is Maxwellian, the Thomson-scattered spectrum is Gaussian in shape and has a spectral half-width $\Delta\lambda_{Th}$ which is related to the electron temperature by:

$$\Delta\lambda_{Th} = 2\lambda_0 \sin(\theta/2) \sqrt{\frac{2kT_e}{m_e c^2}}, \quad (B5.17)$$

where λ_0 is the laser wavelength, θ is the scattering angle, i.e. the angle under which the scattered radiation is detected in respect to the laser beam, T_e is the electron temperature and k , c and m_e are the Boltzmann constant, the speed of light and the electron mass, respectively.

The total Thomson-scattered light intensity is directly proportional to the electron density n_e . Therefore, n_e can be determined from the measured spectrum if the absolute sensitivity of the detection system is accurately calibrated. In practice, this calibration is easily done by measuring the Rayleigh-scattered intensity when the discharge chamber is filled with gas at a prefixed pressure without a plasma. In this

situation the scattered signal intensities I_p (from a plasma with unknown electron density n_e) and I_g (from a gas with known density n_0) are given by:

$$I_p = n_e \sigma_{Th} \Delta\lambda_p f_{system}, \quad (B5.18)$$

and

$$I_g = n_0 \sigma_R \Delta\lambda_g f_{system}, \quad (B5.19)$$

in which σ_{Th} and σ_R are the differential cross sections for Thomson scattering and Rayleigh scattering, respectively, $\Delta\lambda_p$ and $\Delta\lambda_g$ are the spectral FWHM-widths of the scattered spectra from the plasma and the gas and f_{system} is a function of the laser energy and the efficiency of the detection system. The electron density is then given by [B5.22]:

$$n_e = n_0 \frac{I_p \sigma_R \Delta\lambda_g}{I_g \sigma_{Th} \Delta\lambda_p}. \quad (B5.20)$$

Depending on the efficiency of the collecting optics and detectors, Thomson scattering measurements require electron densities of at least 10^{18} to 10^{21} m^{-3} to achieve an acceptable signal level. Densities of 10^{21} m^{-3} can only be achieved at low distances to the plasma generator and additionally near the plasma beam axis in the MPD wind tunnels at the IRS, as shown in Fig. B5.22. The method is applied with the IRS wind tunnel PWK2 and spatial profiles of the electron temperature and electron density were received from the plasma jet [B5.23].

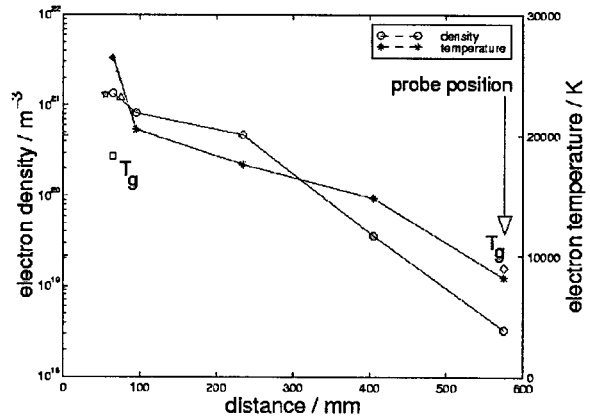


Fig. B5.22: Electron density and temperature profile [B5.24]

An axial scan for the electron density and electron temperature is shown in Fig. B5.22. The gas temperature is indicated with T_g . To achieve a signal in distances more than 200 mm to the plasma generator, one needs to integrate the Thomson scattering emission over thousand shots of the laser and the spatial radial resolution has to be decreased from 2 mm observation length in low distances to the plasma device to 5 mm observation length in higher distances.

References

- [B5.1] Seitzman, J.M.: "Quantitative Applications Of Fluorescence Imaging In Combustion", HTGL Rep. No. T-275, Stanford University, 1991.
- [B5.2] Eckbreth, A.C.: Laser "Diagnostics For Combustion Temperature And Species", 2nd ed., Gordon and Breach Publishers, 1996.
- [B5.3] Feigl M.: "Inbetriebnahme des LIF-Systems und erste Messungen am PWK", IRS 98-IB-08, 1998.
- [B5.4] Salmon, J.T., Laurendeau, N.M.: "Calibration of laser-saturated fluorescence measurements using Rayleigh scattering", Applied Optics, Vol. 24, No. 1, 1985, pp. 65-73.
- [B5.5] Hertz, H. M., Alden, M.: "Calibration of Imaging Laser-Induced Fluorescence Measurements in Highly Absorbing Flames", Applied Physics B 42, 1987, pp. 97-102.
- [B5.6] Bischel, W.K., Bamford, D.J., Jusinski, L.E.: "Absolute calibration of a fluorescence collection system by Raman scattering in H₂", Applied Optics, Vol. 25, No. 7, April 1986, pp. 1215-1221.
- [B5.7] Rensberger, K.J., Jeffries, J.B., Copeland, R.A., Kohse-Höinghaus, K., Wise, M.L. Crosley, D.R.: "Laser-induced fluorescence determination of temperatures in low pressure flames", Applied Optics, Vol.28, No. 17, 1989.
- [B5.8] Arepalli, S.: "Demonstration of the feasibility of laser induced fluorescence for arc jet flow diagnostics", NASA Johnson Space Center CR-185595, 1989.
- [B5.9] Auweter-Kurtz M., Bauer G., Behringer K., Dabala P., Habiger H., Hirsch K., Jentschke H., Kurtz H., Laure S., Stöckle T., Volk G.: "Plasmadiagnostics within the Plasma Wind Tunnel PWK", Z. Flugwiss. Weltraumforsch. 19, pp. 166-179, 1995.
- [B5.10] Grau, T., Messerschmid, E.: "Numerical Investigation of a Partially Ionized Air Flow in a Plasma Wind Tunnel", AIAA 98-2955, 7th AIAA/ASME Joint Thermophysics and Heat Transfer Conference, Albuquerque, NM, June 1998.
- [B5.11] Luque, J., Crosley, D.R.: LIFBASE: "Database and Spectral Simulation Program (Version 1.1)", SRI International Report MP 96-001 (1996).
- [B5.12] Habiger, H.: "Elektrostatische Sonden und Fabry-Perot Interferometrie zur Untersuchung von lichtbogenbeheizten Plasmen für Triebwerksanwendungen und Wiedereintrittssimulation", Dissertation, Universität Stuttgart, 1994.
- [B5.13] Hilfer G.: "Experimentelle und theoretische Beiträge zur Plasma-Wand-Wechselwirkung keramischer Hitzeschutzmaterialien unter Wiedereintrittsbedingungen", Dissertation, Institut für Raumfahrtssysteme, Universität Stuttgart 1998.
- [B5.14] Opila, E.J., Jacobsen, N.S.: "SiO(g) Formation from SiC in Mixed Oxidizing-Reducing Gases", Oxidation of Metals, Vol. 44, Nos. 5/6, 1995, pp 527-544.
- [B5.15] Drira, I., Spielfiedel, A., Edwards, S., Feautrier, N.: "Theoretical study of the A¹Π - X¹Σ⁺ and E¹Σ⁺ - X¹Σ⁺ bands of SiO", J. Quant. Spectrosc. Radiat. Transfer, Vol. 60, No.1, 1998, pp. 1-8.
- [B5.16] Langhoff, S.R., Arnold, J.O.: "Theoretical study of the X¹Σ⁺, A¹Π, C¹Σ⁻ and E¹Σ⁺ states of the SiO molecule", J.Chem. Phys. 70 (02, 1979), pp. 852-863.
- [B5.17] Heynes, A.J.: "Laser-induced fluorescence of silicon monoxide in a glow discharge and an atmospheric pressure flame", Chemical Physics Letters, Vol. 181, No. 2,3 1991, pp.237-244.
- [B5.18] Park, C.S., Crosley, D.R., Eckstrom D.J., Heere K.R.: "Measurement of the A¹Π- X¹Σ⁺ electronic transition moment of SiO using a shock tube", J.Quant.Spectrosc.Radiat.Transfer, Vol.49, No.4, 1993, pp. 349-360.
- [B5.19] Bamford, D.J., O'Keefe, A., Babikian, D.S., Stewart, D.A., Strawa, A.W.: "Characterization of Arcjet Flows Using Laser-Induced Fluorescence", Journal of Thermophysics and Heat Transfer, Vol.9, No.1, January-March 1995.
- [B5.20] Fasoulas S.: "Measurement of Oxygen Partial Pressure in Low Pressure and High-Enthalpy Flows", 19th AIAA Advanced Measurement and Ground Testing Technology Conference, New Orleans, LA, June 1996.
- [B5.22] Muraoka, K., Uchino, K., Bowden, M.D.: "Diagnostics of low density glow discharge plasmas using Thomson scattering", Plasma Phys. Control. Fusion 40, 1998, pp.1221-1239.
- [B5.23] Hirsch, K., Volk, G.: "Thomson scattering with a gated intensified charge-coupled device camera using frequency doubled periodically pulsed Nd:YAG laser", Rev. Sci. Instrum. Vol. 66, No. 11, 1995, pp. 5369-5370.
- [B5.24] Schinkoeth D., Hirsch K., Bauer G., Jentschke H., Schumacher U.: Verhandl. DPG (VI) 3414, 357, P20.15, 1999.
- [B5.25] Feigl M., Auweter-Kurtz M.: "Investigation of nitric oxide in a high enthalpy air plasma flow using laser-induced fluorescence", AIAA 98-2459, 7th Joint Thermophysics and Heat Transfer Conference, Albuquerque, June 1998.
- [B5.26] Fasoulas S.: "Experimentelle und theoretische Charakterisierung einer hochenthalpen Stickstoffströmung zur Wiedereintrittssimulation", Dissertation, Institut für Raumfahrtssysteme, Universität Stuttgart, June 1995.

C Reentry Measurement Techniques

For more than a decade, intensive investigations of reentry conditions for spacecraft have been under way in Europe in view of the development of reusable spacecraft. Ground test facilities have been developed and built for this purpose [C.1-C.7] and a lot of effort has been put into developing numerical simulation processes [C.8-C.11]. Due to the complex physical-chemical relationships - there is in a large area neither chemical nor thermodynamic equilibrium - we are still not in a position today to predict the chemical and physical processes near the surface which can essentially influence the material behavior and therefore also the heat flux and the change from laminar to turbulent flow. However, this is a necessary precondition to qualify thermal protection systems (TPS). On the one hand the TPS can not be allowed to fail and on the other hand its mass must be minimized to gain payload capacity. Especially the US has used its numerous return flights and entries into the atmospheres of other celestial bodies to validate calculation methods. However, only a small portion of these data is available to us in Europe. That is why we are largely dependent on our own experiments. In view of this, a great effort has been

made at the IRS in the last few years to develop and qualify flight measurement equipment and to then use it in actual flights. In the framework of a national mission (MIRKA) [C.12] and participation in return missions (EXPRESS [C.13] and X-38 [C.14]) the IRS was able and continues to be able to gather valuable experience. The following measurement techniques have been or are being developed: a pyrometer system for measuring the temperature distribution on ceramic thermal protection shields, catalytic sensors for determining the heat flux and the degree of dissociation, electrostatic probes for determining the boundary layer density, a boundary layer probe for determining the boundary layer thickness and position and a spectrometer experiment for examining the gas composition. For future interplanetary missions an ablator experiment for determining the recession rate and heat flux and a radiometer probe for determining the radiation heat flux are planned.

References

- [C.1] Auweter-Kurtz, M., Kurtz, H.L., Laure, S., "Plasma Generators for Re-entry Simulation", *Journal of Propulsion and Power*, Vol. 12, No. 6, December 1996, pp. 1053 - 1061.
- [C.2] Auweter-Kurtz, M., Wegmann, Th., "Overview of IRS Plasma Wind Tunnel Facilities", RTO AVT/VKI Special Course on 'Measurement Techniques for High Enthalpy and Plasma Flows', von Karman Institute for Fluid Dynamics, Belgium, October 1999.
- [C.3] Gülhan, A., "Qualification of TPS-Components in the Arc Heated Facility L3K of DLR", *Proceedings of the 3rd European Workshop on Thermal Protection Systems*, ESTEC, Noordwijk, The Netherlands, March 1998, pp. 121-130.
- [C.4] Caristia, S., et. al., "Scirocco Project: Construction Phase Progress Report", CIRA, Italy, *Proceedings of the 3rd European Workshop on Thermal Protection Systems*, ESTEC, Noordwijk, The Netherlands, March 1998, pp. 91-100.
- [C.5] Bottin, B., et. al., "Aerothermodynamic Design of an Inductively-Coupled Plasma Wind Tunnel", *AIAA-97-2498, 32nd Thermophysics Conf.*, Atlanta, GA, June 1997.
- [C.6] Weiland, M.K.H., Beck, W.H., Mee, D.J., Paull, A., "Comparison of Force Measurements in the HEG and T4 Shock Tunnels", *Proceedings of the 3rd European Symposium on Aerothermodynamics for Space Vehicles*, ESTEC, Noordwijk, The Netherlands, November 1998, pp. 631-636.
- [C.7] Willian, J., Sagnier, P., Verant, J.-L., "Effects of Free Electrons in the Onera High Enthalpy Wind Tunnel F4", *Proceedings of the 3rd European Symposium on Aerothermodynamics for Space Vehicles*, ESTEC, Noordwijk, The Netherlands, November 1998, pp. 637-648.
- [C.8] Frühauf, H.-H., Fertig, M., Kanne, S., "Validation of the Enhanced URANUS Nonequilibrium Navier-Stokes Code", *AIAA 99-3683, 33rd Thermophysics Conference*, Norfolk, VA, June/July 1999.
- [C.9] Hejermann, J., Auweter-Kurtz, M., Sleziona, P.C., "Air and Argon RF Plasma Flow Simulation on Structured and Unstructured Meshes", *AIAA-99-3496, 33rd Thermophysics Conference*, Norfolk, VA, June/July 1999.
- [C.10] Kordulla, W., Brück, S. (Eds.), "DLR Contribution to the Fourth European High Velocity Database Workshop", *Forschungsbericht 97-34*, ESTEC, Noordwijk, The Netherlands, November 1994.
- [C.11] Hirschel, E.H., "Thermal Surface Effects in Aerothermodynamics", *Proceedings of the Third European Symposium on Aerothermodynamics for Space Vehicles*, ESTEC, Noordwijk, The Netherlands, November 1998, pp. 17-31.
- [C.12] Schmitt, G., Pfeuffer, H., Kasper, R., Kleppe, F., Burkhardt, J., Schöttle, U.M., "The MIRKA Re-entry Mission", *IAF-98-V.2.07, 49th International Astronautical Congress*, Melbourne, Australia, September/October 1998.
- [C.13] Auweter-Kurtz, M., Hald, H., Koppenwallner, G., Speckmann, H.-D., "German Experiments Developed for Reentry Missions", *Acta Astronautica*, Vol. 38, No. 1, 1996, pp. 47-61.
- [C.14] Herdrich, G., Auweter-Kurtz, M., Hartling, M., Laux, T., "Present Design of the Pyrometric Sensor System PYREX-KAT38 for X-38", *AAAF International Symposium: Atmospheric Re-entry Vehicles and Systems*, Arcachon, France, March 1999.

C1 Pyrometer

The miniaturized linear pyrometer PYREX was designed at the IRS for flight application. PYREX (Pyrometer Re-entry Experiment) was specially designed to determine the temperature on the back of ceramic heat shield materials during reentry without any contact to the surface. Knowing the temperature as a function of time, valuable conclusions about the heat flux and the catalycity (see section C2) of the ceramic material can be made. A one-channel version of PYREX was developed and qualified within the German reentry technology program from DARA [C1.1, C1.2].

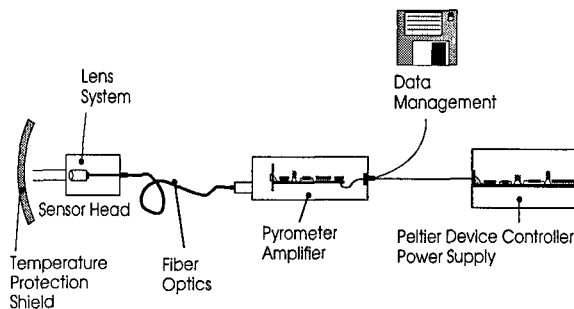


Fig. C1.1: Schematic set-up of PYREX

As shown in Fig. C1.1, the PYREX system consists of five components: the sensor head with the optics, the optical fiber with its connectors, the pyrometer itself with the photodiode and the amplifier, the additional housing for the control electronics and the data processing unit.

The transfer of the radiation into the pyrometer is done by the measurement head which has to image the emitted radiation onto the fiber optics. Essentially, it consists of an SiC-tube which is guided through the structure of the capsule and the ablator/isolator beyond the heat shield tile. The SiC-tube is mounted onto the structure with an inconel flange. The fiber optics with their collecting lenses are

mounted at the measurement head and transfer the signals to the photodiode. The wavelength of the measured signals is limited to a narrow region around 630 nm using a suitable filter combination. The photodiode together with the amplifier electronics are placed in a housing made of aluminum. To guarantee the high accuracy of the measured signal, the temperature of the photodiode has to remain constant (for example at 20°C). This is done by Peltier elements. A thermocouple which is placed directly beside the photodiode delivers a control signal for the Peltier elements. The heat is conducted to the pyrometer housing and the structure. Figure C1.2 shows the integration of the PYREX measurement head into the ceramic shield.

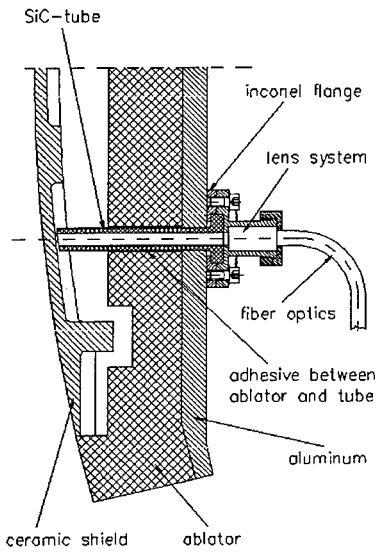


Fig. C1.2: Integration of the measurement head into the structure of the EXPRESS capsule

A two-channel system of PYREX was qualified during the MIRKA mission [C1.3]. With this mission the system successfully measured the temperature profile at two different positions. The instrument disintegrated after the mission and the black body radiator described in section B1.5 was used to compare the signal with the calibration curve prior to the flight.

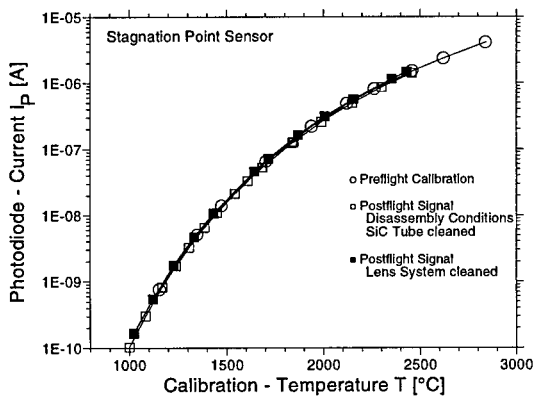


Fig. C1.3: Comparison of preflight calibration and the postflight signal

Figure C1.3 shows the good correlation between the postflight signal and the calibration curve. For the X-38 mission a five-channel system is being developed [C1.4]. Three channels are foreseen for the temperature measurements and two will be used for a catalytic experiment (see section C2).

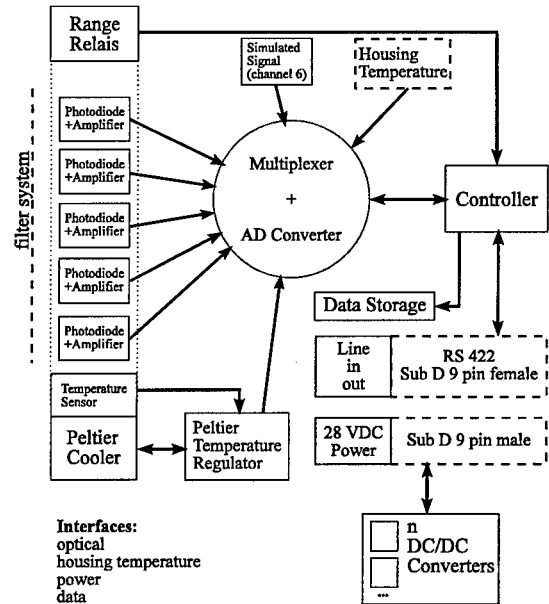


Fig. C1.4: PYREX-KAT38/EM sensor unit

The system PYREX-KAT38 consists of several sub-devices. A schematic view of PYREX-KAT38 is shown in Fig. C1.4. Each of the five sensor heads carries a lens system to focus the incoming radiation on the fiber optics entrance. The fiber optics are attached to the sensor heads and transmit the radiation to the sensor units which contain the electronics. Data transfer, power and control signals are transmitted to the Vehicle Analysis Data Recording (VADR) System, which is being developed by OHB-System GmbH in Bremen, Germany. A portable computer, which can be switched to the sensor unit, enables external data management and preflight tests. Both the X-38 power system and the VADR system are attached to the sensor unit. For PYREX-KATR38 an independent memory bank has been added.

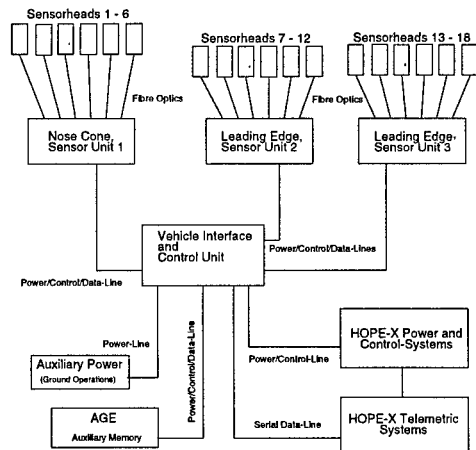


Fig. C1.5: Schematic view of the PYREX-HX system

For the Japanese space plane HOPE-X, three pyrometer systems with six channels each are foreseen (see Fig. C1.5). Six channels will be used for determining the temperature distribution in the nose cap and 12 channels are foreseen for the leading edge (see Fig. C1.6).

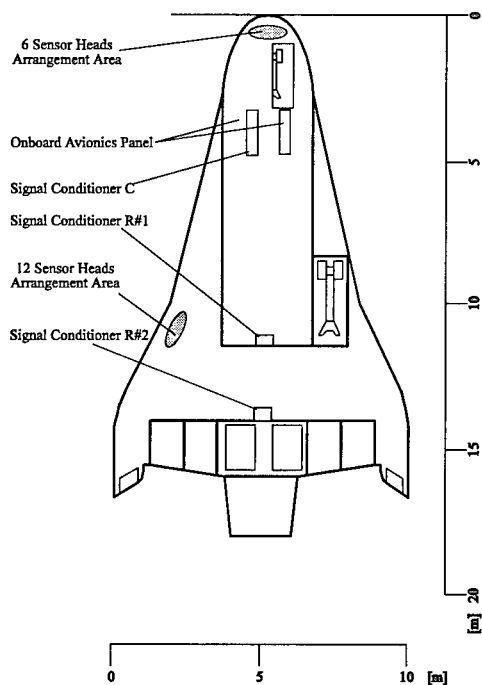


Fig. C1.6: HOPE-X

The graduation has been chosen with respect to the geometries in the nose cone and wing leading edge and the environmental requirements for the sensor units. In addition, it is useful to manufacture three identical sensor units in order to decrease the qualification efforts as only one sensor unit engineering model has to be qualified.

Due to the large distance between the sensor head and the nose cap a special effort is necessary in this mission to calculate the effective emittance for these measurements and to determine the measurement location.

To calibrate the pyrometer sensors the calibration device described in section B1.5 is used. To qualify the pyrometers for reentry application, the numerically predicted heat loads were simulated within the IRS plasma wind tunnels. For EXPRESS, for example, temperatures between 1200°C and 2600°C could be measured. For the EXPRESS mission additional extensive qualification procedures have been performed using various ground test facilities for simulating heat, chemical, thermomechanical, vibration and acceleration loads [C1.1].

In order to improve the accuracy of the measurements in the system, an intrusive postflight program is foreseen. Postflight operations will consist of the readout of the internally stored PYREX-HX data to an auxiliary memory system of the air-ground-equipment (AGE), which is a portable computer, and a preliminary flight data evaluation. A detailed mechanical and optical inspection will be performed after the mission.

During this inspection, the performance of the systems will be checked in comparison to the preflight status. The system will be checked for mechanical and electronic damage. A verification of the previously performed calibration of the system will be carried out using the calibration device described in section B1.5 in order to take possible damage and performance changes into account for an exact flight data processing and temperature evaluation. A functional test in the plasma wind tunnel will be performed to look for reproducibility under acceptance test levels. The system will be generally analyzed to determine improvements for future missions.

The final flight data evaluation will consider all aspects of the postflight inspection. With the known preliminary temperature data of the HOPE-X reentry, the actual emissivity distribution of the C/C structure during the reentry phase and the influence of the thermal behavior of the hardware parts of PYREX-HX must be considered for a final and reliable evaluation of the measured C/C structure temperatures.

References

- [C1.1] Auweter-Kurtz, M., Hald, H., Koppenwallner, G., Speckmann, H.-D., "German Experiments Developed for Reentry Missions", *Acta Astronautica*, Vol. 38, No. 1., 1996, pp. 47-61.
- [C1.2] Auweter-Kurtz, M., "PYREX - Ausbau und Postflight-Untersuchung von PYREX auf EXPRESS", Fördervorhaben 50TT9302, IRS-96-P8, Institut für Raumfahrtssysteme, Universität Stuttgart, December 1996.
- [C1.3] Habiger, H., Auweter-Kurtz, M., Frühholz, H., Herdrich, G., "PYREX - Pyrometric Temperature Measurement on the Ceramic TPS of the Re-Entry Capsule MIRKA", *Proceedings of the 3rd European Workshop on Thermal Protection Systems*, ESTEC, Noordwijk, The Netherlands, March 1998, pp. 353-362.
- [C1.4] Herdrich, G., Auweter-Kurtz, M., Hartling, M., Laux, T., "Present Design of the Pyrometric Sensor System PYREX-KAT38 for X-38", *AAAF International Symposium: Atmospheric Re-entry Vehicles and Systems*, Arcachon, France, March 1999.

C2 Catalytic Sensor

Catalytic sensors are used to gather information on atomic species concentrations in front of the heat shield using materials of different catalycities. The sensors are based on the experience gained from intensive investigations of the catalytic behavior of high temperature materials using plasma wind tunnel facilities.

For years the catalycity of various metallic and ceramic materials has been closely investigated in the IRS plasma wind tunnels (see also section A4.3). Using stationary heat flux probes coated with different materials of known catalycity and calibrated in plasma wind tunnels, information about the atomic concentrations can be qualitatively obtained during reentry. For this purpose sensors based on the Gordon Gage principles (see section A4.1.2) are being

developed at the IRS. The Gardon Gages can be coated using physical vapor deposition (PVD) [C2.1]. Figure C2.1 shows a possible feed-through design for a reentry probe being developed at the IRS. For the calibration of these sensors the atoms species concentrations have to be determined. This will be possible at the IRS in the near future using LIF (see section B5.1).

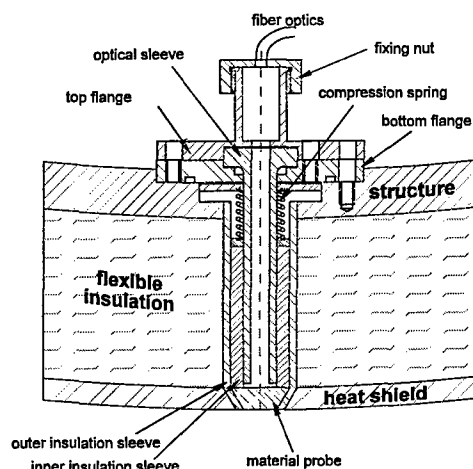


Fig. C2.1: Feed-through from structure to heat shield for a catalytic based sensor

Due to a lack of the time and money necessary for qualification, it was impossible to use such a sensor with the X-38 mission and to insert this kind of probe into the heat shield in the stagnation point region. Because of the expected high temperatures (approx. 2000K), a local increase in the catalycity had to be avoided for safety reasons.

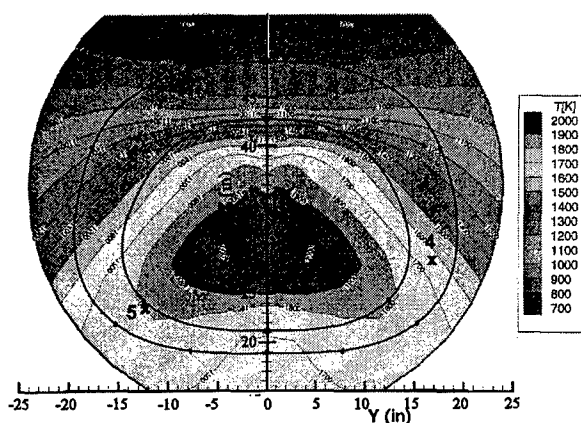


Fig. C2.2: Nose cap (DLR-S) and nose skirt (DASA-B, MAN-T) maximum temperature distribution with PYREX-KAT38 sensor positions

Therefore, it is now planned to apply a layer of low catalycity to the protection shield near the stagnation point 1 (see Fig. C2.2) and to pyrometrically observe the temperature curve on the back of this shield at point 1 and point 2, which are supposed to see the same flow condition due to the symmetrical location. These temperature curves and tests in the plasma wind tunnel will be used to determine the heat flux curve and evaluate the atomic particle densities.

References

- [C2.1] Auweter-Kurtz, M., Dabalà, P., Feigl, M., Habiger, H., Kurtz, H., Stöckle, T., Wegmann, T., Winter, M., "Diagnostik mit Sonden und optischen Verfahren", SFB Arbeits- und Ergebnisbericht 1998, pp. 65-90.

C3 Heat Flux Determination for Ablators

Thermocouples can generally be used for missions with ablative heat shields due to the low heat conductivity of the material and the large wall thickness. If they are inserted at various depths near the surface, the recession rate and the development of the carbonization layer can be determined. Furthermore, as long as the heat conductivity in addition to the degree of emission of the ablator, the heat capacity of the material and its energy consumption for ablation are known, not only can the temperature curve in ablator probes be determined but also the heat flux to the probe surface.

This task, however, is made more difficult with many materials by a non-isotropic heat conduction and heat capacity and conduction both dependent on the depth. In addition, it is in principle possible to determine the ablation energy consumption in plasma wind tunnels, but requires great effort. In addition, the degree of emission of an ablator can change over time due to a change in the chemical composition of the surface and has to be taken into account. In the framework of the reentry mission MIRKA, a corresponding experiment, the so-called HEATIN experiment, was planned, qualified in a plasma wind tunnel at the IRS and successfully tested in flight [C3.1, C3.2].

The main objective of the flight data evaluation of the HEATIN experiment was to determine the transient heat fluxes along the MIRKA surface. The calculation of the areal heat flux density \dot{Q} from measured in-depth temperature histories implies the solution of the inverse heat conduction problem. For this purpose a method has been developed, qualified and successfully applied in order to process flight data [C3.3].

References

- [C3.1] Schmitt, G., Pfeuffer, H., Kasper, R., Kleppe, F., Burkhardt, J., Schöttle, U.M., "The MIRKA Re-entry Mission", IAF-98-V.2.07, 49th International Astronautical Congress, Melbourne, Australia, September/October 1998.
- [C3.2] Reich, G., Jahn, G., "MIRKA Heat Shield Experiment HEATIN - Theoretical and Experimental Approach to the Surface Protected Ablator", 26th International Conference on Environmental Systems, Monterey, CA, July 1996.
- [C3.3] Jahn, G., "Theoretische und experimentelle Untersuchung des Hitzeschutzverhaltens einer Rückkehrkapsel", Dissertation, Universität Stuttgart, 1998.

C4 Boundary Layer Probe

To determine the boundary layer thickness and the pressure, a new probe, shown in Fig. C4.1 is in the process of being developed at the IRS. A retractable probe is used to measure the pressure in the flight body boundary layer perpendicular to the material surface. The pressure curve can be used to determine the position and thickness of the shock front. After a fundamental study [C4.1], the next steps are to choose an appropriate material with temperature stability for the probe head and to build an engineering model for qualification in a plasma wind tunnel. Accompanying flow simulations of the pressure probe in the plasma wind tunnel high enthalpy flow are planned using the numerical methods developed at the IRS [C4.2]. For the qualification of the experiment, emission spectroscopy will be used (see section B2.3).

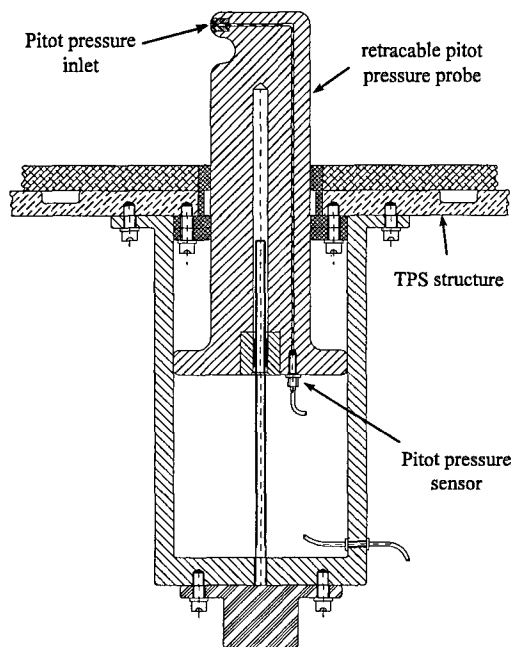


Fig. C4.1: Pressure probe for determining the shock front

References

- [C4.1] Alting, J., "Entwurf eines Flugexperimentes zur Bestimmung der Stoßfrontposition beim Wiedereintritt", IRS-97-S23, Institut für Raumfahrtssysteme, Universität Stuttgart, 1997.
- [C4.2] Sleziona, P.C., Auweter-Kurtz, M., Boie, C., Heiermann, J., Lenzner, S., "Numerical Code for Magneto-Plasma Flows" in: Hyperbolic Problems: Theory, Numerics, Applications, 7th International Conference in Zürich, February 1998, Vol. II, Eds. M. Fey, R. Jeltsch, International Series of Numerical Mathematics, Vol. 130, 1999, Birkhäuser Verlag, Basel, pp. 905-914.

C5 Spectrometer Probe

The thermal and mechanical loads onto a space vehicle surface during re-entry are mainly defined by the plasma state and its chemical composition close to the wall. Although various numerical codes have

been developed to simulate these conditions, the experimental data which can be used to verify the numerical simulation are still poor. The existing experimental data concentrate on single species such as NO-radiation. Experiments that give information about multiple important species within the post-shock layer at the same time have not been performed yet.

One way to gain access to the required data is given by emission spectroscopic measurements during the re-entry flight. Figure C5.1 shows the measurement principle of the proposed experiment.

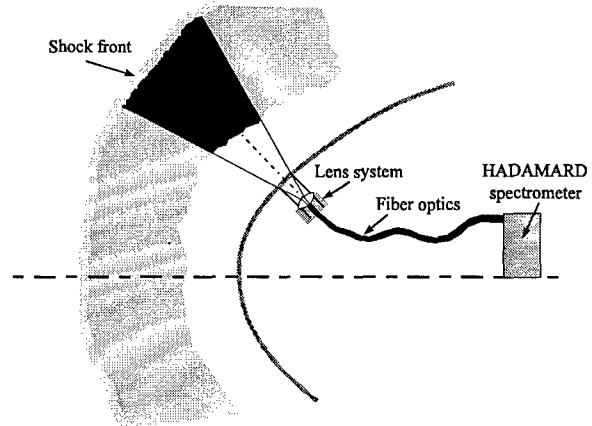


Fig. C5.1: Measurement principle of the proposed experiment

A newly developed spectrometer which operates according to the HADAMARD principle is planned to gain spectral data in the flow field around a space vehicle re-entering the earth's atmosphere [C5.1]. Data collection is foreseen during the entire flight trajectory.

Due to the integrating character of the measurement, a direct extraction of temperatures or densities from the measured data does not seem possible; however, the desired information can be obtained by a comparison with numerically simulated data.

A spectrometer for use in space has to fulfill special requirements. Besides the optical qualities, it has to be small and light and withstand the mechanical, thermal and chemical loads. The proposed spectrometer shown in Fig. C5.2 uses the HADAMARD principle to minimize the size and weight of the apparatus.

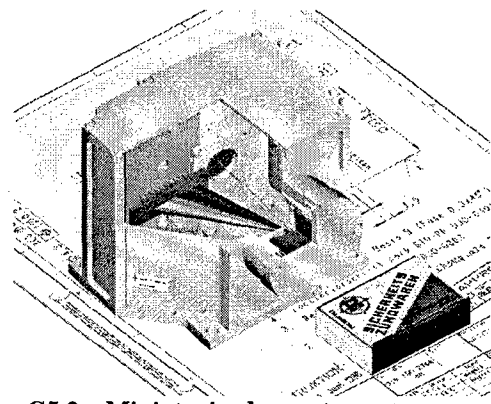


Fig. C5.2: Miniaturized spectrometer operated according to the HADAMARD principle

The HADAMARD principle is based on the use of different entrance slits into the spectrometer. These slits are used in various combinations to perform the measurements. A transformation of the obtained data results in a higher effective resolution than with conventional spectrometers [C5.2]. This allows for a smaller configuration of the spectrometer itself. The obtained data will cover a wavelength range from 200 nm up to 800 nm with a resolution of approximately 0.5 nm. Thus, it will contain the emission of all relevant radiating air species such as N_2 , NO, N, O and N_2^+ .

The functional qualification procedure will be performed in the plasma wind tunnels of the IRS [C5.3, C5.4]. Magnetoplasmadynamic as well as thermal plasma generators creating sub- and supersonic flows, respectively, will be used to simulate the condition along the flight path at lower and higher stagnation pressures.

Emission spectroscopic experiments have already been carried out to investigate the boundary layer in front of a blunt body in a subsonic high enthalpy plasma flow at total pressures between 0.1 kPa and 3.5 kPa representing the first part of re-entry (see section B2.3.3). The ratios of the emission of different species were found to be a valuable indicator for chemical processes, especially within the boundary layer. Although within a flight mission Abel inversion or temperature determination techniques as used in the plasma wind tunnel experiments are not possible, a comparison with numerically simulated spectral data will provide valuable information about the chemical and thermodynamic processes in the plasma flow.

The numerical data for the comparison with the measurement will be provided by the numerical flow solver URANUS (Upwind Relaxation Algorithm for Nonequilibrium Flows of the University of Stuttgart) [C5.5], the radiation transport code HERTA (High Enthalpy Radiation Transport Algorithm) [C5.6] and the radiation database PARADE (Plasma Radiation Database) [C5.7]. In recent years, URANUS has been validated for different flow cases, such as Shuttle, FIRE II, MIRKA, RAMCII, BSUV I & II and Stardust. Compared to these cases, however, the proposed experiment will perform more detailed spectroscopic measurements by offering the emission of multiple radiating species measured at the same time. This will enable a more specific investigation of the physical processes in the plasma.

Using the radiation codes, the chemical model of the flow field solver can be verified by a comparison of measured and calculated radiation. Different models can be tested and the influence of chemical reactions on radiation signals can be shown. For example, the modeling of the NO production can be checked by this method.

The requirements for the spectrometer are mainly defined by a wavelength range which allows the detection of the main radiating species in the flow as presented in Fig. C5.3 and Fig. B2.26 in section B2.4.1. The experimental data were measured within experimental investigations of the boundary layer in

front of a blunt body in the subsonic air plasma flow in the IRS plasma wind tunnel PWK2. The numerical data result from a simulation with PARADE for a shuttle reentry at a distance of 77 km to the ground.

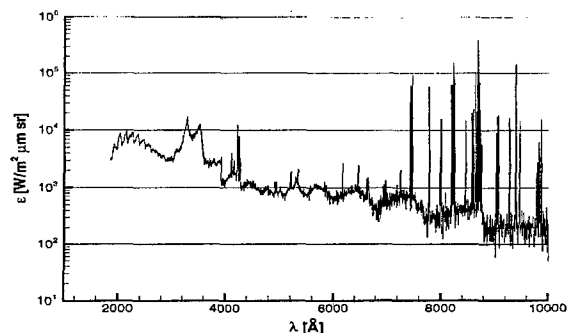


Fig. C5.3: Numerically simulated spectrometer signal during a shuttle reentry at a distance of 77km to the ground

The lower border of the wavelength range is defined by the emission of NO in the UV from 200 nm up to 250 nm. The upper border is defined by the emission of atomic oxygen with strong emission lines at 776 nm. For this reason, a wavelength region from 200 nm to almost 800 nm has to be covered. According to the plasma wind tunnel measurements, a resolution of about 1 nm is sufficient to separate the emission of the different species.

The dynamic range of the detector has to be chosen as high as possible to take both varying intensities within one spectrum and the variation along the flight trajectory into account. At the same time, a sufficient readout frequency has to be guaranteed to minimize the integration along the flight path. A measurement time of 100 ms is considered to give both sufficient time resolution and measured intensity. For these reasons, a dynamic range of 16 bit is proposed.

Because the spectrometer has been proposed for a flight mission, the dimensions and weight have to be minimized.

The demonstrator of the spectrometer has already been built and tested at Jena Optic. It is the first demonstration of the HADAMARD principle with a double-array-arrangement in the world. Functionality and performance of the spectrometer were demonstrated with a device having dimensions of 150 mm × 150 mm × 50 mm. The next step in the project is the development of a prototype. The design and materials for the optical head have already been prepared for use in space. Minimization of the volume to 80 mm × 80 mm × 50 mm is foreseen. An enlargement of the wavelength range from 200 nm up to 800 nm by a resolution goal of about 0.5 nm is planned.

Although most specifications for the coupling to the space vehicle itself will have to be specified by the requirements of the flight mission, some basic requirements have to be fulfilled in any case.

It will surely not be possible to mount the spectrometer directly behind the thermal protection material. The transmission of the radiation to the spectrometer inlet has to be done using optical fibers. For the coupling of the fibers to the surface material a feed-

through has to be used to couple the fiber optics to the heat shield.

This phase is of particular importance for the success of the whole project. The design and construction of the feed-through will be done in cooperation with the DLR-Stuttgart. Furthermore, the focusing system has to be protected from both plasma influences and erosion products of the heat shield.

At the IRS, several flight missions have been performed with experiments like PYREX, measuring the material temperature with a minimized pyrometer (see section C1). The experience gained from these flight experiments will be used for the construction of the required coupling device.

References

- [C5.1] Winter, M., Kanne, S., Lonschinski, J., Auweter-Kurtz, M., Frühauf, H.-H., "Proposal for a Reentry Experiment Using a Newly Developed Spectrometer", Proceedings of the 3rd European Symposium on Aerothermodynamics for Space Vehicles, ESTEC, Noordwijk, The Netherlands, November 1998, pp. 711-716.
- [C5.2] Riesenberger, R., Voigt, W., Schöneich, J., "Kompakt-Spektrofotometer mit Mikro-systemtechnik", SENSOR 97, Nürnberg, 1997.
- [C5.3] Auweter-Kurtz, M., Kurtz, H.L., Laure, S., "Plasma Generators for Re-entry Simulation", Journal of Propulsion and Power, Vol. 12, No. 6, December 1996, pp. 1053 - 1061.
- [C5.4] Auweter-Kurtz, M., Wegmann, Th., "Overview of IRS Plasma Wind Tunnel Facilities", RTO AVT/VKI Special Course on 'Measurement Techniques for High Enthalpy and Plasma Flows', von Karman Institute for Fluid Dynamics, 1999.
- [C5.5] Kanne, S., Knab, O., Frühauf, H.-H., Messerschmid, E., "The Influence of Rotational Excitation on Vibration-Chemistry-Vibration-Coupling", AIAA-96-1802, 31st AIAA Thermophysics Conference, New Orleans, LA, June 1996.
- [C5.6] Gogel, T., "Numerische Modellierung von Hochenthalpieströmungen mit Stahlungsverlusten", Dissertation, Universität Stuttgart, 1994.
- [C5.7] S. Kanne, T. Gogel, M. Dupius, E. Messerschmid, "Simulation of Radiation Experiments on Reentry Vehicles Using the New Radiation Database PARADE", AIAA-97-2562, 32nd AIAA Thermophysics Conference, Atlanta, GA, June 1997.

C6 Electrostatic Triple Probe

An electrostatic triple probe is being developed to determine the electron density and electron temperature during reentry. With reentry missions from low earth orbit the densities of charged particles close to the surface is very low. This is no longer the case for sample return missions which now also being planned in Europe. For these missions the knowledge of the electron density close to the surface is of great importance due to the high reactivity of these particles and a possible impact on radio communication.

Triple probes offer the possibility of monitoring this quantity on-line with a high time resolution (as described in section A7.3). A drawing of this experiment is shown in Fig. C6.1.

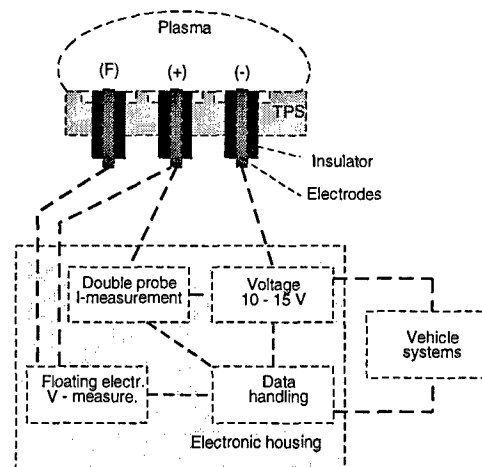


Fig. C6.1: Flight experiment with an electrostatic triple probe

C7 Radiometer Probe

During high enthalpy reentries and many interplanetary missions, the radiative portion of the heat flux to a vehicle can no longer be neglected. The high gas enthalpy and high radiative intensities of some carbonaceous molecules cause high radiation intensities. This is, for example, the case for the Huygens mission. At the IRS the heat shield material for Huygens was tested and the final qualification for this mission was carried out. Within this context a radiometer probe (see section A9) for wind tunnel application was developed at the IRS [C7.1]. Based on this knowledge, it is planned to develop a flight version for future European interplanetary missions which can be qualified in the plasma wind tunnels of the IRS [C7.2].

References

- [C7.1] Röck, W., "Simulation des Eintritts einer Sonde in die Atmosphäre des Saturnmondes Titan in einem Plasmawindkanal", Dissertation, Universität Stuttgart, 1998.
- [C7.2] Auweter-Kurtz, M., Wegmann, Th., "Overview of IRS Plasma Wind Tunnel Facilities", RTO AVT/VKI Special Course on 'Measurement Techniques for High Enthalpy and Plasma Flows', von Karman Institute for Fluid Dynamics, 1999.

C8 Acknowledgements

The authors would like to thank all colleagues who were involved in the development and qualification of the diagnostic techniques at the IRS during the last decade. Special thanks also to Mrs. Jennifer Baer-Engel for her help in writing this script.